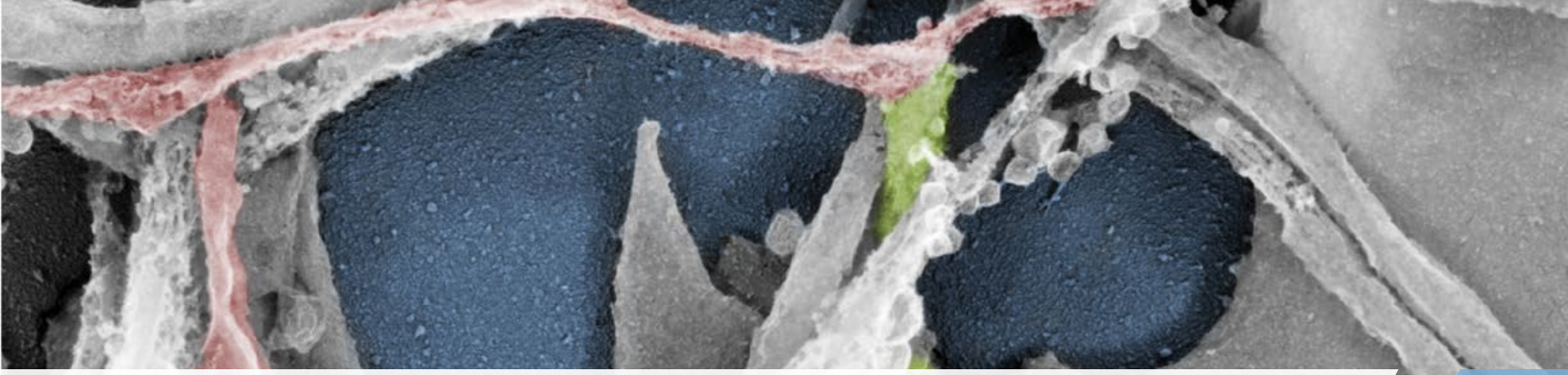

# SHORT COURSE 2:

## Functional, Structural, and Molecular Imaging, and Big Data Analysis

Organized by Ed Boyden, PhD,
and Kwanghun Chung, PhD

SOCIETY *for* NEUROSCIENCE

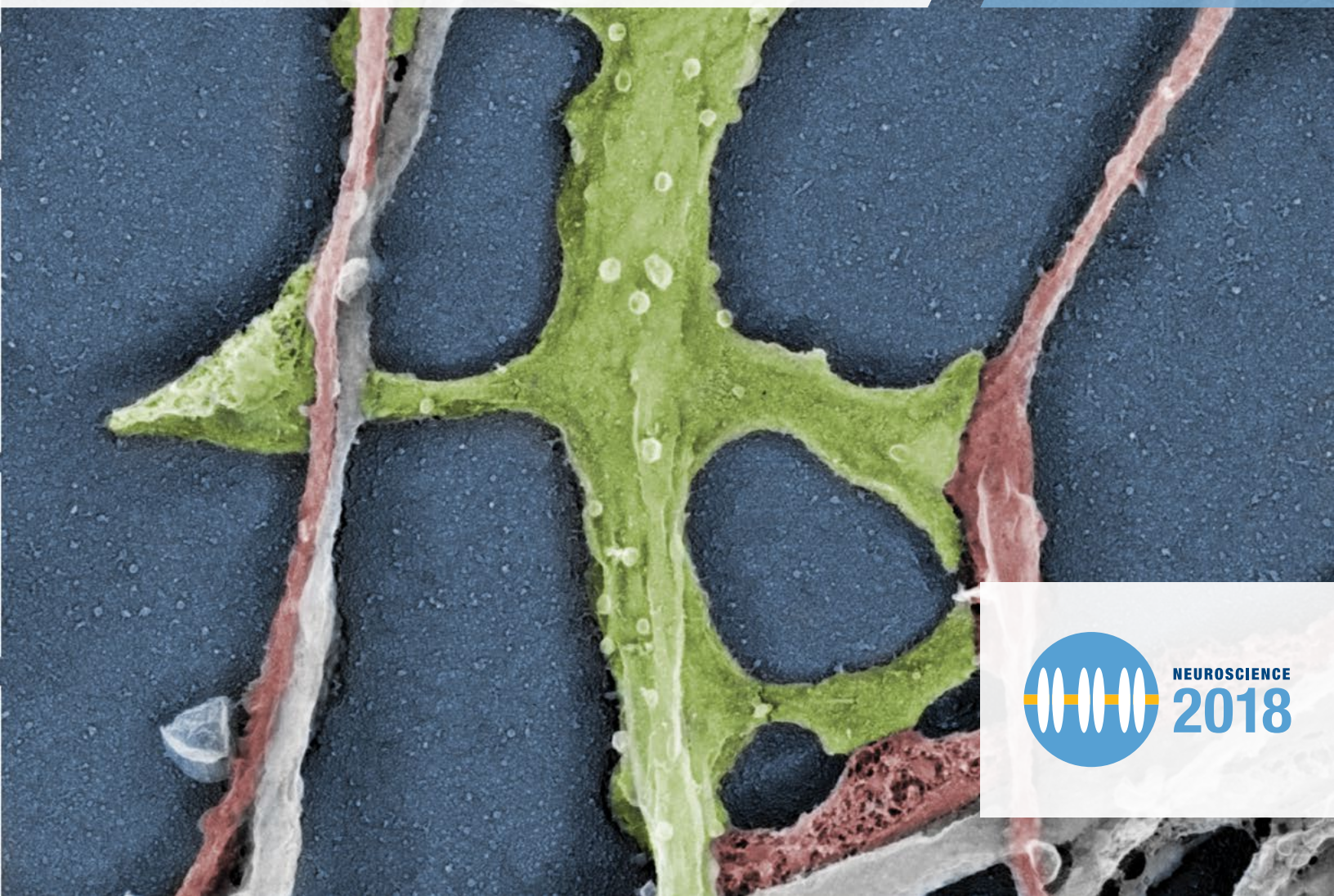

NEUROSCIENCE 2018

# Short Course 2

## Functional, Structural, and Molecular Imaging, and Big Data Analysis

Organized by Ed Boyden, PhD, and Kwanghun Chung, PhD

Society for Neuroscience

Please cite articles using the model:
[AUTHOR'S LAST NAME, AUTHOR'S FIRST & MIDDLE INITIALS] (2018)
[CHAPTER TITLE] Functional, Structural, and Molecular Imaging, and Big Data Analysis.
(Boyden E, Chung K, eds) pp. [xx-xx].
Washington, DC : Society for Neuroscience.

NEUROSCIENCE 2018

# SHORT COURSE 2

## Functional, Structural, and Molecular Imaging, and Big Data Analysis

Organized by Ed Boyden, PhD, and Kwanghun Chung, PhD

Friday, November 2, 2018

8 a.m.–6 p.m.

Location: San Diego Convention Center • Room: 6CF

| TIME | TOPIC | SPEAKER |
|---|---|---|
| 7:30–8 a.m. | CHECK-IN | |
| 8–8:10 a.m. | Opening Remarks | Ed Boyden, PhD • Massachusetts Institute of Technology<br>Kwanghun Chung, PhD • Massachusetts Institute of Technology |
| 8:10–8:50 a.m. | Advanced Optical Methods for Multi-Scale Optical Probing and Manipulation of Neural Circuits | Valentina Emiliani, PhD • Paris Descartes University |
| 8:50–9:30 a.m. | Optical Imaging of Neural Ensemble Dynamics in Behaving Animals | Mark Schnitzer, PhD • Stanford University |
| 9:30–10:10 a.m. | High-Resolution and High-Speed In Vivo Imaging of the Brain | Na Ji, PhD • University of California, Berkeley |
| 10:10–10:30 a.m. | BREAK | |
| 10:30–11:10 a.m. | High-Speed Volumetric Microscopy and Wide-Field Optical Mapping of Whole-Brain Activity | Elizabeth Hillman, PhD • Columbia University |
| 11:10–11:50 a.m. | Denoising, Compression, Demixing, and Deconvolution of Functional Imaging Data | Liam Paninski, PhD • Columbia University |
| 11:50 a.m.–12:30 p.m. | Connectome Coding | Joshua Vogelstein, PhD • Johns Hopkins University |
| 12:30–1:30 p.m. | LUNCH — ROOM 25 | |
| 1:30–2:10 p.m. | Holistic Molecular Imaging and Rapid Phenotyping of the Brain | Kwanghun Chung, PhD • Massachusetts Institute of Technology |
| 2:10–2:50 p.m. | Toward Integrative Optical Interrogation of the Brain | Ed Boyden, PhD • Massachusetts Institute of Technology |
| 2:50–3 p.m. | Summary and Introduction of Breakout Sessions | Ed Boyden, PhD, and Kwanghun Chung, PhD |
| 3–3:15 p.m. | BREAK | |

**AFTERNOON BREAKOUT SESSIONS • PARTICIPANTS SELECT FIRST DISCUSSION GROUPS AT 3:15 P.M.**

| TIME | BREAKOUT SESSIONS | SPEAKERS | ROOM |
|---|---|---|---|
| 3:15–4:30 p.m. | Group 1:<br>Collection and Analysis of Structural and Molecular Data | Kwanghun Chung, PhD, Joshua Vogelstein, PhD, and Ed Boyden, PhD | 24B |
| | Group 2:<br>Collection and Analysis of Neural and Signaling Dynamics | Elizabeth Hillman, PhD, Liam Paninski, PhD, Ed Boyden, PhD | 24A |
| | Group 3:<br>Microscopy Technology | Valentina Emiliani, PhD, Mark Schnitzer, PhD, and Na Ji, PhD | 23A |
| 4:30–4:45 p.m. | BREAK | | |

**AFTERNOON BREAKOUT SESSIONS • PARTICIPANTS SELECT SECOND DISCUSSION GROUPS AT 4:45 P.M.**

| | | | |
|---|---|---|---|
| 4:45–6 p.m. | Group 1:<br>Collection and Analysis of Structural and Molecular Data | Kwanghun Chung, PhD, and Joshua Vogelstein, PhD | 24B |
| | Group 2:<br>Collection and Analysis of Neural and Signaling Dynamics | Elizabeth Hillman, PhD, Liam Paninski, PhD, Ed Boyden, PhD | 24A |
| | Group 3:<br>Microscopy Technology | Valentina Emiliani, PhD, Mark Schnitzer, PhD, and Na Ji, PhD | 23A |

# Table of Contents

Agenda . . . . . 3

Introduction . . . . . 5

Expansion Microscopy: Development and Neuroscience Applications
*Emmanouil D. Karagiannis, PhD, and Edward S. Boyden, PhD* . . . . . 7

Holistic Molecular Imaging and Rapid Phenotyping of the Brain
*Kwanghun Chung, PhD* . . . . . 17

Holographic Illumination for Two-Photon Optogenetics
*Dimitrii Tanese, PhD, and Valentina Emiliani, PhD* . . . . . 23

High-Speed Recording of Neural Spikes in Awake Mice and Flies with a Fluorescent Voltage Sensor
*Yiyang Gong, PhD, Cheng Huang, PhD, Jin Zhong Li, DVM, Benjamin F. Grewe, PhD, Yanping Zhang, MD, Stephan Eismann, MS, and Mark J. Schnitzer, PhD* . . . . . 41

High-Resolution and High-Speed *In Vivo* Imaging of the Brain
*Cristina Rodriguez, PhD, and Na Ji, PhD* . . . . . 52

What Is Connectome Coding?
*Eric W. Bridgeford, BS, Daniel Sussman, PhD, Vince Lyzinski, PhD, Yichen Qin, PhD, Youngser Park, PhD, Brian Caffo, PhD, Carey E. Priebe, PhD, and Joshua T. Vogelstein, PhD* . . . . . 62

Analysis of Functional Imaging Data at Single-Cellular Resolution
*Eftychios A. Pnevmatikakis, PhD, and Liam Paninski, PhD* . . . . . 75

High-Speed Volumetric Microscopy and Wide-Field Optical Mapping of Whole-Brain Activity
*Elizabeth M. C. Hillman, PhD* . . . . . 86

# Introduction

We find ourselves in an era of great innovation in neuroscience that is yielding a constant stream of new molecular reporters of neural activity, novel microscope architectures, and new strategies for acquiring and analyzing large physiological, molecular, and anatomical datasets. How can these technologies be deployed in the service of making the highest-impact discoveries in both basic and applied neuroscience? With the help of a number of excellent faculty at the cutting edge of the invention and application of novel tools, we have designed this course to explore the basic principles underlying how such technologies work as well as practical considerations for adopting and integrating these methods into neuroscience. Our experts will cover a broad range of topics in their lectures, including the imaging of neural ensemble dynamics, multiscale optogenetic manipulation of circuits, high-resolution *in vivo* imaging, and multiscale structural and molecular phenotyping techniques. We will also review methods for extracting information from the large-scale functional, structural, and molecular imaging datasets that result. During the breakout sessions, our experts and teaching assistants (TAs) will discuss each technology in depth and go over detailed protocols, with the goal of enabling attendees to intelligently select the best technological path and rapidly adopt the technologies. We will also discuss examples that show how these technologies can be integrated into a streamlined experiment to study a given scientific question in the fundamental or translational realm.

Our experts (listed in alphabetical order) include pioneers of optical methods for studying the brain, who will discuss the following topics: Ed Boyden will discuss how integrating optical tools for reading neural activity, writing neural activity, and mapping the connectivity of the brain might be unified to enable new kinds of structure–function linkage in neuroscience experimentation. Kwanghun Chung will discuss a series of technologies including CLARITY, SWITCH, MAP, stochastic electrotransport, SHIELD, and eFLASH (unpublished) that enable integrated multiscale imaging and molecular phenotyping of both animal tissues and human clinical samples. Valentina Emiliani will discuss the powerful intersection of three-dimensional (3D) parallel holographic illumination for the single-cell-targeted optogenetic control of neurons, and the development of novel opsins with high-performance characteristics for mediating such control. She will explore the optical principles underlying such microscopy systems, as well as practical considerations governing the most suitable manipulation approaches for given problems. Elizabeth Hillman will discuss swept confocally aligned planar excitation (SCAPE) microscopy (a form of light-sheet microscopy that uses a single stationary objective lens to perform high-speed 3D microscopy of a diversity of neuroscientifically relevant systems) and wide-field optical mapping (WFOM) for imaging neural activity and brain hemodynamics across the whole dorsal cortex in awake, behaving mice. Na Ji will present wavefront shaping techniques that enable the imaging of neural circuits with higher resolution, greater depth, and faster speed than before, including examples that enable synapse-level spatial resolution imaging throughout the entire depth of the cortex, and a volumetric microscopy strategy with a novel video rate (~30 Hz). Liam Paninski will discuss methods for extracting information from single-cell resolution calcium and voltage imaging data, including denoising, demixing, and deconvolving approaches to extract estimates of voltage and spiking activity from video data. Mark Schnitzer will present recent advances from his lab that are allowing the measurement of neural codes across large scales and optical readout of neural voltage oscillations. These advances include miniature microscopes, new forms of two-photon microscopy, and novel fiber optic methods for transmembrane electrical measurements performed optically (TEMPO). In the context of neural coding, Josh Vogelstein will discuss "connectome coding"—the characterization of the relationship between past environments and stimuli (even past experiences of ancestors encoded in the genome) and current neural connectivity.

NOTES

In summary, our speakers will cover the dynamical readout, dynamical control, and the anatomical and molecular mapping of the brain, as well as the computational analysis of the datasets thus acquired. We anticipate that students will emerge from the course with not just new technical insights, but also the ability to think across technologies and scales to devise new approaches to confronting neuroscience questions.

# Expansion Microscopy: Development and Neuroscience Applications

Emmanouil D. Karagiannis, PhD,[1] and
Edward S. Boyden, PhD[1,2,3,4]

[1]MIT Media Lab
Massachusetts Institute of Technology
Cambridge, Massachusetts

[2]Department of Biological Engineering
Massachusetts Institute of Technology
Cambridge, Massachusetts

[3]McGovern Institute for Brain Research
Massachusetts Institute of Technology
Cambridge, Massachusetts

[4]Department of Brain and Cognitive Sciences
Massachusetts Institute of Technology
Cambridge, Massachusetts

NOTES

## Introduction

At the core of many neuroscience questions—ranging from understanding how memories are encoded, to how neurons transform sensory inputs into motor outputs, to how emotions and decisions are implemented—is a need to understand how neural circuits are organized to yield complex emergent functions. Understanding the nature of brain disorders, and pointing the way to new therapeutics, is also increasingly demanding a knowledge of how brain cells, molecular cascades, and connections change in disease states. Ideally one would be able to map biomolecules such as neurotransmitters, receptors, and ion channels across the spatial extents of neurons and neural circuits. Traditional microscopes are limited by diffraction, and thus, specialized technologies have been required to perform imaging with nanoscale precision. Electron microscopy is capable of nanoscale resolution and has yielded many insights into the wiring diagrams of neural circuits (Kasthuri et al., 2015; Eichler et al., 2017). However, it typically yields little molecular information about the neurons in those circuits. Super-resolution light microscopy methods have powerfully revealed many molecular features of neurons at the nanoscale level (D'Este et al., 2015; He et al., 2016), but such methods are difficult to apply to extended three-dimensional (3D) specimens, such as neural circuits, owing to their speed and complexity. To address the need for a method of imaging extended 3D objects such as neural circuits, with molecular information and at nanoscale resolution, we recently developed a novel modality of imaging. In contrast to earlier methods of nanoscale imaging that magnify information emitted from a specimen, we discovered that it was possible to physically magnify the specimen itself (Chen et al., 2015).

In this new methodology, which we call expansion microscopy (ExM) (Figs. 1*a–e*), we synthesize a dense, interconnected web of a swellable polymer, such as sodium polyacrylate, throughout a preserved specimen, such as brain. The polymer is very dense, such that the distance between adjacent polymer threads is on the order of the dimension of a biomolecule. We anchor biomolecules such as proteins or RNA (or labels bound to those biomolecules, e.g., antibodies) to the polymer network via covalently binding anchoring molecules. We treat the specimen with heat, detergent, and/or enzymes to mechanically homogenize the specimen so that it can expand evenly, and then finally we add water. The swellable polymer absorbs the water and expands, bringing along the anchored biomolecules or labels (Fig. 1*f*). The net result is that biomolecules or labels that are initially localized within the diffraction limit of a traditional microscope are now separated in space so that they can be resolved. As a byproduct of this process, the specimen also becomes completely transparent, having become mostly water (Fig. 1*g*).

ExM builds from two sets of ideas that go back to the late 1970s and early 1980s. Around that time, the physicist Toyoichi Tanaka at MIT was creating and studying the physics of swellable gels (Tanaka et al., 1980). He found that they could swell many orders of magnitude in volume in ways that could be described via phase transition mathematics. Around the same time, Peter Hausen and Christine Dreyer at the Max Planck Institute developed polymer hydrogel embedding of fixed tissues for the enhancement of imaging, synthesizing polyacrylamide networks throughout preserved specimens (Hausen and Dreyer, 1981). ExM fuses these two old concepts to enable physical magnification of specimens with nanoscale precision.

In this review, we first discuss the principles of how ExM works, covering some of the rapidly exploding family of protocols that have been invented in the past few years that are making ExM easier to use and more powerful. We then discuss some current applications in the field of neuroscience.

## Principles of Expansion Microscopy

Since our discovery of ExM, accompanied by a proof-of-concept protocol and validation data originally published in 2015 showing its high performance in cultured mammalian cells and mouse brain tissue (Chen et al., 2015), we have developed several variants specialized for simple visualization of proteins (Tillberg et al., 2016) and RNA (Chen et al., 2016) using off-the-shelf chemicals. These variants can expand cells and tissues to much greater extents than the original protocol (Chang et al., 2017) and can easily be applied to human pathology specimens (Zhao et al., 2017). Several groups, including ours, have also shown the technology to work in a wide diversity of nonbrain tissues, both normal and diseased (e.g., cancer-containing) (Ku et al., 2016; Tillberg et al., 2016; Zhao et al., 2017), and even with pathogens like bacteria (Zhang et al., 2016). Many other groups have joined in independently creating ExM protocol variants as well, creating related protocols for the visualization of proteins and RNA (Truckenbrodt and Rizzoli, 2014; Chozinski et al., 2016; Ku et al., 2016; Tsanov

NOTES

et al., 2016; Kumar et al., 2017). Demonstrations of utility as well as scientific applications to a diversity of neuroscience questions have begun in a variety of species, ranging from planaria (Wang et al., 2016) to *Drosophila* (Mosca et al., 2017) to mouse (Crittenden et al., 2016; Sümbül et al., 2016) to nonhuman primate (Tillberg et al., 2016) to human (Deshpande et al., 2017). Rather than go through individual protocols one by one, as we have in previous reviews (Gao et al., 2017) and protocols papers (Asano et al., 2018), here we discuss the general principle of how ExM works, seeking a unified workflow picture (Figs. 1*a*–e). We will not go into detailed protocols in this paper; they are available on the Internet at ExpansionMicroscopy.org.

## Anchoring biomolecules

First, biomolecules such as proteins (Tillberg et al., 2016) or RNA (Chen et al., 2016), or labels that bind to these biomolecules, such as fluorescent antibodies (for proteins) (Chen et al., 2015; Tillberg et al., 2016) or fluorescent *in situ* hybridization (FISH) probes (for RNA) (Tsanov et al., 2016), are functionalized with chemical handles that allow them to be covalently

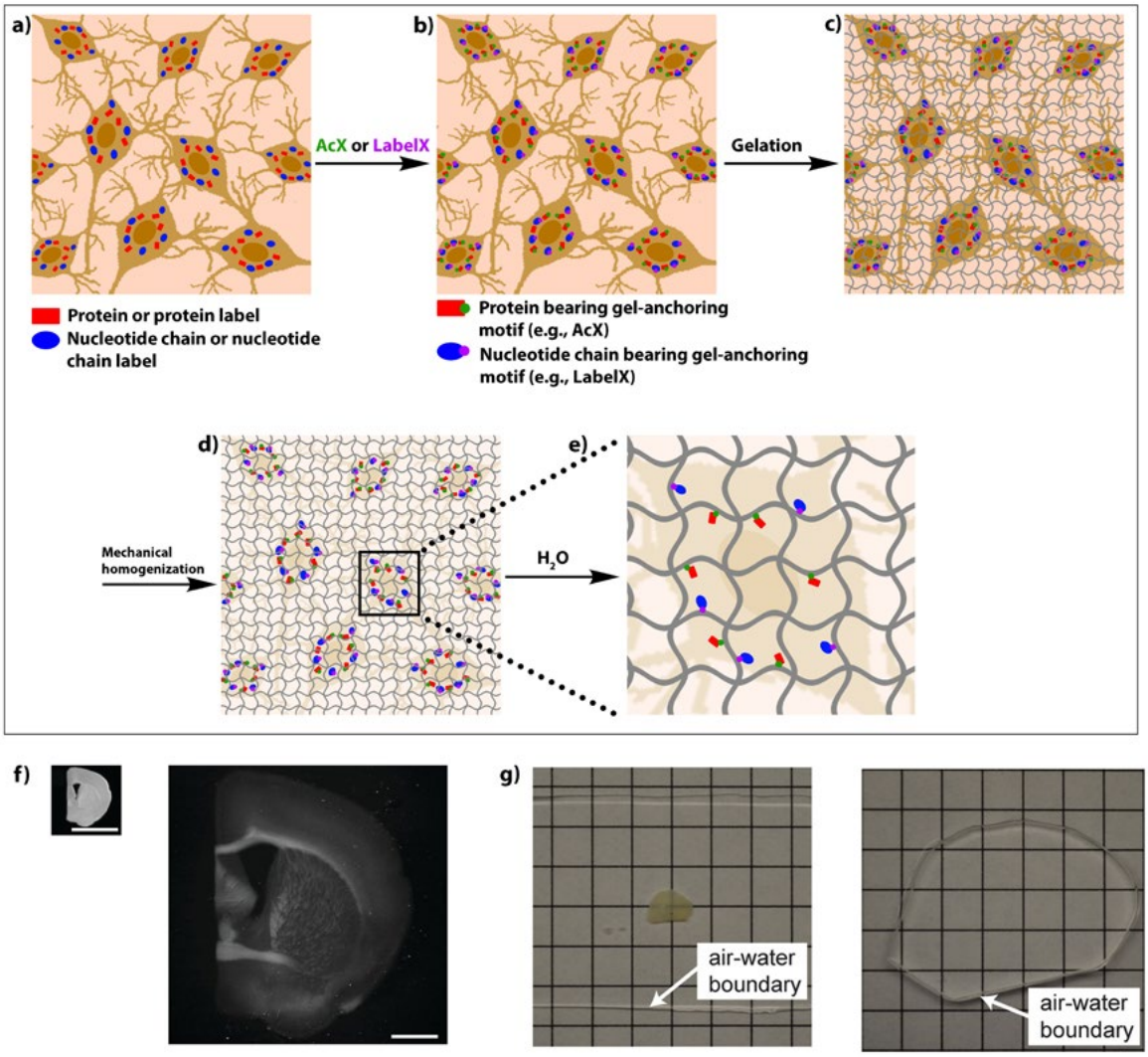


**Figure 1.** ExM workflow. ***a***, Biomolecules, or labels highlighting biomolecules of interest, in fixed cells or tissues, are functionalized with chemical handles (green, AcX binds proteins; purple, LabelX binds nucleic acids such as mRNA) that enable them to be (***b***) covalently anchored to a swellable polymer mesh (composed of cross-linked sodium polyacrylate) that is (***c***) evenly and densely synthesized throughout the specimen. ***d***, The sample is mechanically homogenized by treatment with heat, detergent, and/or proteases. ***e***, Adding water initiates polymer swelling, which results in biomolecules or labels being pulled apart in an even, isotropic manner, enabling nanoscale-resolution imaging (***f***) by conventional microscopes. ***g***, Expansion significantly reduces scattering of the sample since the sample is mostly water. A 200-μm-thick fixed mouse brain slice is opaque before ExM, but after expansion is completely transparent. Scale bars: ***f***, 5 mm. Panels ***f*** and ***g*** modified with permission from Chen et al. (2015), Figs. 1*B, C*; Suppl. Fig. 2. Copyright 2015, American Association for the Advancement of Science.

NOTES

anchored to the polymer (Figs. 1*a*,*b*). For example, applying a commercially available small molecule, the succinimidyl ester of 6-((acryloyl)amino)hexanoic acid (acryloyl-X, SE; abbreviated here as AcX), will equip amines on proteins (either endogenous proteins, genetically encoded fluorophores, or applied fluorescent antibodies) with an acrylamide functional group, which can be linked to a growing polyacrylate polymer chain made in a downstream step (Tillberg et al., 2016). Other groups have developed related anchoring strategies (Chozinski et al., 2016 and Ku et al., 2016). Applying a small molecule that contains an alkylating group that reacts to guanine, as well as an acrylamide group, easily made by mixing two off-the-shelf chemicals (which we call LabelX), enables endogenous RNA (and DNA) to be equipped with a handle that can be linked to a growing polymer chain (Chen et al., 2016). Alternatively, applying FISH probes chemically pre-equipped with a similar linker will allow for these probes to be linked to the polymer (Tsanov et al., 2016).

## Polymer embedding

Next, we synthesize a densely cross-linked sodium polyacrylate mesh throughout the specimen so that it permeates the cells, with polymer chains going between and around the biomolecules and/or labels (Figs. 1*b*,*c*). We do this by immersing the specimen in a solution containing sodium acrylate monomer (which can form long chains once triggered to polymerize) and cross-linking agents so that the final gel topology is a densely linked mesh. The small molecular weight of these building blocks enables their diffusion throughout cells and tissue in a short time, usually <0.5 h for a piece of brain tissue 100 µm thick. This incubation is performed at 4°C, allowing the building blocks to permeate the sample. Polymerization is initiated when the sample is transferred to a 37°C incubator. Within a few hours, a densely cross-linked polymer web is formed in the sample.

This polymerization process is a standard free-radical polymerization process, not unlike the kind used to make polyacrylamide gels for electrophoresis, and is similar to the protocol of Hausen and Dreyer (1981). We use a vinyl addition free-radical polymerization of sodium acrylate monomers (along with the co-monomer acrylamide) and an N-N'-methylenebisacrylamide cross-linker, initiated by the generation of free radicals by a polymerization initiator (e.g., ammonium persulfate). We add the polymerization accelerator tetramethylethylenediamine as well as a polymerization inhibitor, 4-hydroxy-TEMPO, to tune the rate of polymerization so that monomers have time to diffuse throughout the sample before the reaction takes off. The resultant mesh is extremely dense; small-angle x-ray scattering data from similar polymers suggest that the mesh size (spacing between polymer chains) may be in the 1–2 nm range (Cohen et al., 1992). Such polymer spacing—smaller than many biomolecules themselves—suggests the possibility of immobilizing biomolecules to the polymer on an individual basis as well as the potential for isotropic expansion (and thus resolution) down to the 1–2 nm range (although the latter has not yet been experimentally realized).

## Mechanically homogenizing the specimen

Next, the specimen—now permeated with swellable polymer, and with key biomolecules or labels bound to the polymer—is homogenized in its mechanical properties (Figs. 1*c*,*d*) so that the tissue components do not resist expansion. This can be performed by treatment with high temperatures and detergents (Ku et al., 2016; Tillberg et al., 2016) or with proteases that cleave proteins either broadly (Chen et al., 2016; Chozinski et al., 2016; Tillberg et al., 2016) or specifically (Tillberg et al., 2016). In protocols using heat and detergents, the goal is to denature proteins so that they can be easily separated in the expansion step. In protocols using enzymes, the goal is either to destroy proteins that are no longer relevant to the later visualization steps or to cut them into smaller pieces that can be easily separated. For example, we and others have found that fluorescent antibodies and genetically encoded fluorescent proteins are resistant to proteinase K digestion at doses where most other proteins are broken down by proteinase K treatment (Chozinski et al., 2016; Tillberg et al., 2016). Thus, for specimens bearing such antibodies or fluorescent proteins, anchoring them to the permeating swellable hydrogel, followed by proteolytic destruction of the other proteins, enables mechanical homogenization while preserving the information to be observed (i.e., the antibody locations or the fluorescent protein locations).

## Expanding the specimen

Finally, adding water (Figs. 1*d*,*e*) triggers the swelling of the sodium polyacrylate polymer so that the biomolecules or labels that are chemically linked to the polymer are pulled apart. Osmotic force draws water into the specimen–polymer composite, and the highly charged carboxyl groups along the polyacrylate backbone then further repel each other (a key advantage of using a polyelectrolyte gel). At that time, labels (e.g., fluorescent antibodies) (Ku et al., 2016; Tillberg et al., 2016) or FISH probes (Chen

et al., 2016) can be applied to label biomolecules that were anchored and expanded away from each other but that are not yet visualizable. Also at that time, signals can be amplified by any of a number of traditional methods. These include hybridization chain reaction amplification of FISH signals (Chen et al., 2016); adding DNA strands equipped with fluorophores (Chang et al., 2017); or using fluorescent streptavidin to add fluorophores to a previously anchored biotinylated probe (Chozinski et al., 2016). The original ExM protocol (Chen et al., 2015), as well as many of the follow-on protocols (Ku et al., 2016; Tillberg et al., 2016; Zhao et al., 2017), reported 4–4.5× linear expansion factors (~100× volumetric expansion) in pure water (Fig. 1*f*); expanding specimens in a low-osmolarity saline solution (helpful for maintaining hybridization of postexpansion probes applied to implement FISH) resulted in a ~3.3× linear expansion (Chen et al., 2016).

### Results of the expansion process: ExM, proExM, and iExM

We and others extensively compared ExM-expanded samples with pre-expansion samples imaged using traditional super-resolution means (e.g., SIM [structured illumination microscopy]) (Chen et al., 2015; Tillberg et al., 2016; Zhao et al., 2017), STORM (stochastic optical reconstruction microscopy) (Chozinski et al., 2016; Chang et al., 2017), as well as analysis of expanded biomolecular complexes that were previously characterized at a ground-truth nanostructural level (e.g., with electron microscopy) (Chen et al., 2015; Chang et al., 2017). As a result, we were able to show that the expansion process was isotropic, with distortion errors of only a few percent over length scales of tens to hundreds of micrometers (Chen et al., 2015; Tillberg et al., 2016; Zhao et al., 2017). The excellent isotropy results from the design of the dense and highly cross-linked swellable polymer, as well as the mechanical homogenization. By analyzing biomolecular complexes of known structure (e.g., microtubules), we further estimated that current expansion processes might be introducing as little as 5–10 nm of error in terms of fundamental resolution (Chang et al., 2017) (although pinpointing this number will require further study). As a result, a 4.5× expansion will evenly expand specimens so that when imaged on, e.g., a confocal microscope with 300 nm lateral resolution, the effective resolution will be 300 nm/4.5 ~ 70 nm.

A specimen can be expanded multiple times for even better effective resolution—a process we call iterative ExM (iExM) (Chang et al., 2017). A specimen is first expanded as in Figure 1, except using a chemically cleavable cross-linker rather than N-N'-methylenebisacrylamide to form the initial polyelectrolyte gel network. Such cross-linkers include N,N'-(1,2-dihydroxyethylene)bis-acrylamide (DHEBA) and N,N'-Bis(acryloyl)cystamine (BAC). After the first expansion is complete, a second swellable polymer (with an uncleavable cross-linker) is synthesized in the space opened up by the first expansion. The biomolecules or labels are transferred from the first gel to the second, the first gel is cleaved, and then the second gel is expanded. This double-expansion process results in a linear expansion factor of ~4.5 × 4.5 ~ 20×, which would theoretically result in an effective resolution of 300 nm/20 ~ 15 nm, but in practice is slightly larger because of the size of the labels (i.e., antibodies, linkers) used to stain the specimen in the first place.

In summary, there are different ExM protocols that are optimal for different kinds of specimen and biological questions. The process of functionalizing the proteins or antibodies with AcX and expanding them away from each other we call protein retention ExM (proExM) (Tillberg et al., 2016). proExM can be performed by staining the biological samples with primary and secondary antibodies before expansion, or by expanding proteins away from each other before expansion and then adding antibodies afterwards. Other groups developed related strategies for proExM in parallel to us (Chozinski et al., 2016; Ku et al., 2016). The process of functionalizing RNA with LabelX and decrowding RNA molecules in a swellable hydrogel for later FISH visualization we call ExFISH (Chen et al., 2016).

## Applications of ExM to Neuroscience

From our earliest paper on the subject, we showed that ExM could be used to visualize synaptic contacts between neurons in brain circuits, e.g., in the mouse hippocampus (Figs. 2*a–d*) (Chen et al., 2015). In particular, with ExM (Chen et al., 2015), proExM (Tillberg et al., 2016), or iExM (Chang et al., 2017), one can visualize synapses and synaptic proteins (e.g., excitatory and inhibitory neurotransmitter receptors, presynaptic scaffolding proteins, postsynaptic scaffolding proteins, neurotransmitter synthesis enzymes) in the context of many neurons in a connected circuit. This ability enables cellular and synaptic analyses to be made across scales in a neural network.

One interesting application of ExM is in the visualization of Brainbow (combinatorially

NOTES

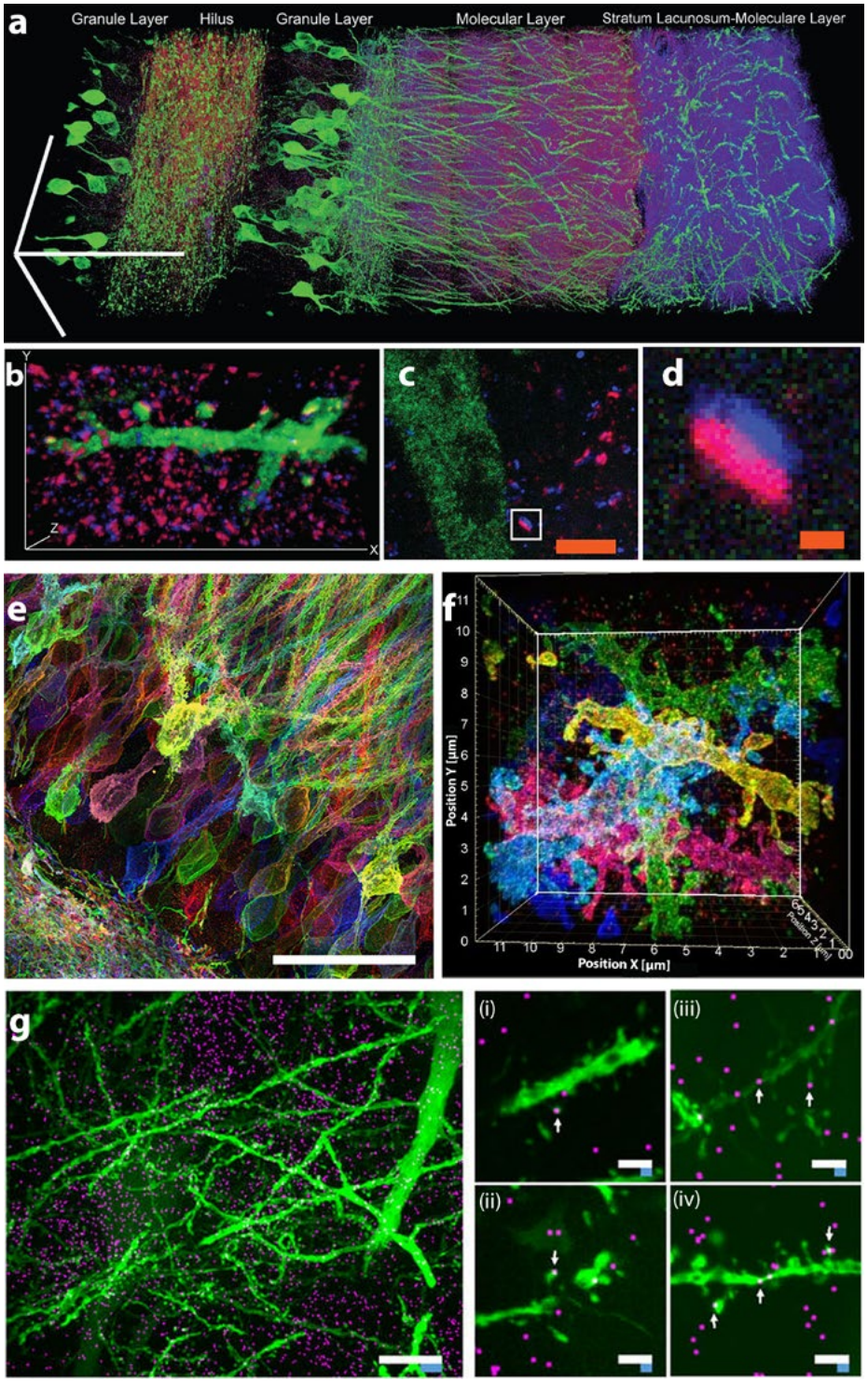


**Figure 2.** ExM of brain circuitry. ***a***, Expanded mouse hippocampus, with yellow fluorescent protein (YFP)–expressing neurons (green) antibody stained for the postsynaptic protein Homer1 (magenta) and the presynaptic protein bassoon (blue). ***b***, A hippocampal neuron from a piece of mouse brain tissue expanded and labeled as in (***a***), highlighting a single branch bearing multiple synapses. ***c***, ***d***, mouse cortex, expanded and labeled as in ***a***, with a single synapse (box in ***c***) highlighted in ***d***. ***e***, proExM and ***f***, iExM of mouse hippocampus expressing Brainbow (combinatorially expressed fluorophores for randomly labeling neurons with different colors). ***g***, ExFISH imaging of single RNA molecules (magenta) in mouse hippocampus with simultaneous visualization of protein (green, YFP). Left, Dlg4 mRNA (magenta) visualized simultaneously with YFP (green). Middle (*i, ii*), dendrites with spine-localized Dlg4 mRNA highlighted with arrows. Right (*iii, iv*), dendrites with Camk2a mRNA highlighted with arrows. Scale bars: ***a***, 100 µm; ***b***, 13.5 µm *x*, 7.3 µm *y*, 2.8 µm *z*; ***c***, 2.5 µm; ***d***, 250 nm; ***e***, 5 µm; ***g***, white, 10 µm; blue, divided by the expansion factor of 3; *i–iv*, white, 2 µm; blue, divided by the expansion factor of 3. Panels ***a–d*** adapted with permission from Chen et al., 2015, Figs. 3*g,h,* 4*a,c*. Copyright 2015, American Association for the Advancement of Science. Panel ***e*** adapted with permission from Tillberg et al. (2016), Fig. 3*f*. Copyright 2016, Springer Nature. Panel ***f*** modified with permission from Chang et al. (2017), Suppl. Fig. 12. Copyright 2017, Nature Publishing Group. Panel ***g*** adapted with permission from Chen et al. (2016), Figs. 3*i–k*. Copyright 2016, Nature Publishing Group.

NOTES

expressed, genetically encoded fluorophore-labeled neural circuitry) (Cai et al., 2013) (via ~70 nm effective resolution proExM in Fig. 2*e* and Tillberg et al., 2016; and via ~25 nm effective resolution iExM in Fig. 2*f* and Chang et al., 2017). Such volumes can be imaged on ordinary confocal microscopes, making neural circuit mapping into a democratized activity requiring hardware of the kind accessible to most groups. A recent algorithmic and experimental study suggests that automated tracing of neural morphologies in expanded brain circuits containing neurons labeled with Brainbow may be possible (Sümbül et al., 2016).

proExM has successfully revealed synaptic architectures in mouse striatal circuitry (Crittenden et al., 2016) as well as in the *Drosophila* brain (Mosca et al., 2017) and zebrafish brain (Freifeld et al., 2017). proExM has also proven useful for characterizing astrocytic gap junctions near blood vessels in human epilepsy patient brain specimens (Deshpande et al., 2017). Furthermore, proExM has helped perform a study in the planarian *Schmidtea mediterranea* that revealed a new nonneural cell type the authors proposed to be a planarian glial cell (Wang et al., 2016).

Mapping messenger RNAs (mRNAs) and other nucleic acids with subsynaptic precision in intact neural circuits is important for confronting many questions related to how gene expression is regulated in a spatial manner, throughout neural circuits, in development, plasticity, and disease. ExFISH has been used to visualize the location and identity of single mRNA molecules, with nanoscale precision, in brain circuits with covisualization of proteins (Fig. 2*g*) (Chen et al., 2016).

Specimen expansion, in addition to providing nanoscale resolution across extended 3D specimens, enables two other key features. One is that, after expansion, the final tissue–gel composite is ~99% water, making the resulting specimens transparent and essentially optical-aberration free (Fig. 1*g*) (Chen et al., 2015). This makes light-sheet imaging into a very fast nanoscale-resolution modality, as we have shown by applying light-sheet imaging to expanded samples (Chen et al., 2016), thereby enabling multiple-order-of-magnitude acceleration over earlier nanoscale-resolution imaging technologies.

A second benefit of ExM is the decrowding of the biomolecules or labels as they are pulled apart during the swelling, which creates room around biomolecules for amplification and analysis of chemical reactions. For example, the hybridization chain reaction (Choi et al., 2014) results in many fluorophores being targeted to a single biomolecule via a self-assembling DNA complex. Molecular decrowding makes more room for these large complexes, which otherwise might overlap or compete against each other (Chen et al., 2016). Molecular decrowding could also enable epitopes, which may be concealed in protein complexes, to be revealed by separating proteins from one another (Tillberg et al., 2016). Finally, by creating room around biomolecules for well-controlled performance of useful reactions, decrowding may help in the future to support better performance of analytical reactions, such as *in situ* sequencing (Lee et al., 2014), multiplexed antibody staining (Jungmann et al., 2014), and multiplexed hybridization (Moffitt et al., 2016). For example, the Zhuang lab has recently shown ExM to decrowd mRNAs sufficiently to improve the yield of their multiplexed error-robust fluorescence *in situ* hybridization (MERFISH) protocol. This yields an exponential amount of information in a linear number of hybridization steps, with RNA density more than 10-fold higher than previously reported (Wang et al, 2018).

## Common Problems and Strategies to Overcome Them

As with any new technology, early adopters will need to confront potential problems in order to deploy ExM in their scientific field. Early adoption also presents opportunities for refinement and innovation, as various groups have published papers applying or validating ExM in new contexts like *Drosophila* (Cahoon et al., 2017; Mosca et al., 2017), zebrafish (Freifeld et al., 2017), and human brain (Deshpande et al., 2017). One common problem that people encounter early in their experiences with ExM samples is the fragility of the expanded samples. We recommend storing, transporting, and handling samples in the unexpanded state as much as possible and expanding them in water at the latest feasible moment. Paintbrushes and spatulas can be used to handle gels when unexpanded, but expanded gels require care to transport, for example, being carried on coverslips that evenly support the gel (Gao et al., 2017). Storing samples in the compact state may also help preserve fluorescence for longer periods than in the expanded state. In an unbuffered solution like pure water (as used in the expanded state), fluorophores can deteriorate faster than if samples are stored in PBS or another buffered salt solution in the compact state (Gao et al., 2017).

Another common problem is that expanded samples, being volumetrically diluted by a hundredfold or

NOTES

more, can sometimes appear dim when imaged with a microscope, and/or be hard to find because they are so transparent. Thus, amplifying the brightness of labels (as described earlier) can be very helpful. It is important to validate antibodies in unexpanded samples to ensure that they work, since the dilution effect of expansion will compound any antibody errors with additional difficulty of visualization. If antibodies are to be applied after expansion, it is important not to use proteases that destroy epitopes but instead to use denaturing conditions to mechanically homogenize cells and tissues (Ku et al., 2016; Tillberg et al., 2016). If antibodies are to be applied pre-expansion, it is important not to use cyanine dyes on secondary antibodies, since they will be destroyed during the polymerization process. (For a list of alternative dyes that work well in ExM, see Tillberg et al., 2016.)

To facilitate imaging, it can be helpful to trim the gel to the smallest size feasible and to shape the boundary of the gel (e.g., by cutting the edge in a pattern) so that its shape will tell you its orientation (Synthetic Neurobiology Group, 2017). When imaging a subregion, it is also very helpful to image samples both before and after expansion with a low-magnification microscope to understand where you are in the sample. It can be helpful to immobilize expanded samples in agarose or to mount them on a sticky surface (e.g., a polylysine-coated coverslip or slide) to prevent them from drifting during imaging (Gao et al., 2017). For details on how to mount samples for stable imaging in a diversity of microscope settings and other helpful tips, see Gao et al. (2017) and up-to-date protocols at our website: ExpansionMicroscopy.org.

## Acknowledgments

This chapter was modified with permission from a previously published article: Karagiannis and Boyden (2018) Expansion microscopy: development and neuroscience applications. Curr Opin Neurobiol 50:56–63. Copyright 2018, Elsevier. For funding, E.S.B. acknowledges the Howard Hughes Medical Institute–Simons Foundation Fellowship; John Doerr; the Open Philanthropy Project; Intelligence Advanced Research Projects Activity D16PC00008; National Institutes of Health grants 1R01MH103910, 1RM1HG008525, 1R01MH110932, 1R01EB024261, and 1R01NS102727; the Cancer Research UK Grand Challenge; and the U.S. Army Research Laboratory and the U. S. Army Research Office under Contract/Grant W911NF1510548. We thank all members of the Synthetic Neurobiology Group for helpful discussions.

## References

Asano SM, Gao R, Wassie AT, Tillberg PW, Chen F, Boyden ES (2018) Expansion microscopy: protocols for imaging proteins and RNA in cells and tissues. Curr Protoc Cell Biol 80:e56.

Cahoon CK, Yu Z, Wang Y, Guo F, Unruh JR, Slaughter BD, Hawley RS (2017) Superresolution expansion microscopy reveals the three-dimensional organization of the *Drosophila* synaptonemal complex. Proc Natl Acad Sci USA 114:E6857–E6866.

Cai D, Cohen KB, Luo T, Lichtman JW, Sanes JR (2013) Improved tools for the Brainbow toolbox. Nat Methods 10:540–547.

Chang J-B, Chen F, Yoon Y-G, Jung EE, Babcock H, Kang JS, Asano S, Suk H-J, Pak N, Tillberg PW, Wassie AT, Cai D, Boyden ES (2017) Iterative expansion microscopy. Nat Methods 14:593–599.

Chen F, Tillberg PW, Boyden ES (2015) Expansion microscopy. Science 347:543–548.

Chen F, Wassie AT, Cote AJ, Sinha A, Alon S, Asano S, Daugharthy ER, Chang J-B, Marblestone A, Church GM, Raj A, Boyden ES (2016) Nanoscale imaging of RNA with expansion microscopy. Nat Methods 13:679–684.

Choi HM, Beck VA, Pierce NA (2014) Next-generation *in situ* hybridization chain reaction: higher gain, lower cost, greater durability. ACS Nano 8:4284–4294.

Chozinski TJ, Halpern AR, Okawa H, Kim H-J, Tremel GJ, Wong RO, Vaughan JC (2016) Expansion microscopy with conventional antibodies and fluorescent proteins. Nat Methods 13:485–488.

Cohen Y, Ramon O, Kopelman IJ, Mizrahi S (1992) Characterization of inhomogeneous polyacrylamide hydrogels. J Polym Sci Part B Polym Phys 30:1055–1067.

Crittenden JR, Tillberg PW, Riad MH, Shima Y, Gerfen CR, Curry J, Housman DE, Nelson SB, Boyden ES, Graybiel AM (2016) Striosome-dendron bouquets highlight a unique striatonigral circuit targeting dopamine-containing neurons. Proc Natl Acad Sci USA 113:11318–11323.

Deshpande T, Li T, Herde MK, Becker A, Vatter H, Schwarz MK, Henneberger C, Steinhäuser C, Bedner P (2017) Subcellular reorganization and altered phosphorylation of the astrocytic gap junction protein connexin43 in human and experimental temporal lobe epilepsy. Glia 65:1809–1820.

NOTES

D'Este E, Kamin D, Göttfert F, El-Hady A, Hell SW (2015) STED nanoscopy reveals the ubiquity of subcortical cytoskeleton periodicity in living neurons. Cell Rep 10:1246–1251.

Eichler K, Li F, Litwin-Kumar A, Park Y, Andrade I, Schneider-Mizell CM, Saumweber T, Huser A, Eschbach C, Gerber B, Fetter RD, Truman JW, Priebe CE, Abbott LF, Thum AS, Zlatic M, Cardona A (2017) The complete connectome of a learning and memory centre in an insect brain. Nature 548:175–182.

ExpansionMicroscopy.org. Physical specimen expansion enabling 3-D large volume, nanoscale imaging. Available at http://expansionmicroscopy.org.

Freifeld L, Odstrcil I, Förster D, Ramirez A, Gagnon JA, Randlett O, Costa EK, Asano S, Celiker OT, Gao R, Martin-Alarcon DA, Reginato P, Dick C, Chen L, Schoppik D, Engert F, Baier H, Boyden ES (2017) Expansion microscopy of zebrafish for neuroscience and developmental biology studies. Proc Natl Acad Sci USA 114:E10799–E10808.

Gao R, Asano SM, Boyden ES (2017) Q&A: Expansion microscopy. BMC Biol 15:50.

Hausen P, Dreyer C (1981) The use of polyacrylamide as an embedding medium for immunohistochemical studies of embryonic tissues. Stain Technol 56:287–293.

He J, Zhou R, Wu Z, Carrasco MA, Kurshan PT, Farley JE, Simon DJ, Wang G, Han B, Hao J, Heller E, Freeman MR, Shen K, Maniatis T, Tessier-Lavigne M, Zhuang X (2016) Prevalent presence of periodic actin-spectrin-based membrane skeleton in a broad range of neuronal cell types and animal species. Proc Natl Acad Sci USA 113:6029–6034.

Jungmann R, Avendaño MS, Woehrstein JB, Dai M, Shih WM, Yin P (2014) Multiplexed 3D cellular super-resolution imaging with DNA-PAINT and Exchange-PAINT. Nat Methods 11:313–318.

Karagiannis ED, Boyden ES (2018) Expansion microscopy: development and neuroscience applications. Curr Opin Neurobiol 50:56–63.

Kasthuri N, Hayworth KJ, Berger DR, Schalek RL, Conchello JA, Knowles-Barley S, Lee D, Vázquez-Reina A, Kaynig V, Jones TR, Roberts M, Morgan JL, Tapia JC, Seung HS, Roncal WG, Vogelstein JT, Burns R, Sussman DL, Priebe CE, Pfister H, et al. (2015) Saturated reconstruction of a volume of neocortex. Cell 162:648–661.

Ku T, Swaney J, Park J-Y, Albanese A, Murray E, Cho JH, Park Y-G, Mangena V, Chen J, Chung K (2016) Multiplexed and scalable super-resolution imaging of three-dimensional protein localization in size-adjustable tissues. Nat Biotechnol 34:973–981.

Kumar A, Kim JH, Ranjan P, Metcalfe MG, Cao W, Mishina M, Gangappa S, Guo Z, Boyden ES, Zaki S, York I, García-Sastre A, Shaw M, Sambhara S (2017) Influenza virus exploits tunneling nanotubes for cell-to-cell spread. Sci Rep 7:40360.

Lee JH, Daugharthy ER, Scheiman J, Kalhor R, Yang JL, Ferrante TC, Terry R, Jeanty SSF, Li C, Amamoto R, Peters DT, Turczyk BM, Marblestone AH, Inverso SA, Bernard A, Mali P, Rios X, Aach J, Church GM (2014) Highly multiplexed subcellular RNA sequencing *in situ*. Science 343:1360–1363.

Moffitt JR, Hao J, Bambah-Mukku D, Lu T, Dulac C, Zhuang X (2016) High-performance multiplexed fluorescence *in situ* hybridization in culture and tissue with matrix imprinting and clearing. Proc Natl Acad Sci USA 113:14456–14461.

Mosca TJ, Luginbuhl DJ, Wang IE, Luo L (2017) Presynaptic LRP4 promotes synapse number and function of excitatory CNS neurons. eLife 6:e27347.

Sümbül U, Roossien D, Chen F, Barry N, Boyden E, Cai D, Cunningham JP, Paninski L (2016) Automated scalable segmentation of neurons from multispectral images. In: 2016 Advances in Neural Information Processing Systems, Vol 29 (Lee DD, Sugiyama M, Luxburg UV, Guyon I, Garnett R, eds). Cambridge, MA: MIT Press.

Synthetic Neurobiology Group (2017) proExM gel demonstration. Available at https://www.youtube.com/watch?v=OksNCAJwxVI.

Tanaka T, Fillmore D, Sun ST, Nishio I, Swislow G, Shah A (1980) Phase transition in ionic gels. Phys Rev Lett 45:1636–1639.

Tillberg PW, Chen F, Piatkevich KD, Zhao Y, Yu C-C, English BP, Gao L, Martorell A, Suk H-J, Yoshida F, DeGennaro EM, Roossien DH, Gong G, Seneviratne U, Tannenbaum SR, Desimone R, Cai D, Boyden ES (2016) Protein-retention expansion microscopy of cells and tissues labeled using standard fluorescent proteins and antibodies. Nat Biotechnol 34:987–992.

Truckenbrodt S, Rizzoli SO (2014) Spontaneous vesicle recycling in the synaptic bouton. Front Cell Neurosci 8:409.

Tsanov N, Samacoits A, Chouaib R, Traboulsi A-M, Gostan T, Weber C, Zimmer C, Zibara K, Walter T, Peter M, Bertrand E, Mueller F (2016) smiFISH and FISH-quant – a flexible single RNA detection approach with super-resolution capability. Nucleic Acids Res 44:e165.

Wang G, Moffitt JR, Zhuang X (2018) Multiplexed imaging of high-density libraries of RNAs with MERFISH and expansion microscopy. Sci Rep 8:4847

Wang IE, Lapan SW, Scimone ML, Clandinin TR, Reddien PW (2016) Hedgehog signaling regulates gene expression in planarian glia. eLife 5:e16996.

Zhang YS, Chang J-B, Alvarez MM, Trujillo-de Santiago G, Aleman J, Batzaya B, Krishnadoss V, Ramanujam AA, Kazemzadeh-Narbat M, Chen F, Tillberg PW, Dokmeci MR, Boyden ES, Khademhosseini A (2016) Hybrid microscopy: enabling inexpensive high-performance imaging through combined physical and optical magnifications. Sci Rep 6:22691.

Zhao Y, Bucur O, Irshad H, Chen F, Weins A, Stancu AL, Oh E-Y, DiStasio M, Torous V, Glass B, Stillman IE, Schnitt SJ, Beck AH, Boyden ES (2017) Nanoscale imaging of clinical specimens using pathology-optimized expansion microscopy. Nat Biotechnol 35:757–764.

NOTES

# Holistic Molecular Imaging and Rapid Phenotyping of the Brain

Kwanghun Chung, PhD

Department of Chemical Engineering
Institute for Medical Engineering and Science (IMES)
Picower Institute for Learning and Memory
Massachusetts Institute of Technology
Cambridge, Massachusetts

NOTES

## Introduction

Human organs such as the brain comprise vast numbers of molecules, cell types, and intricate tissue organizations. Understanding the complex interactions of these components is essential for many fields of biology and often requires high-dimensional information across many scales. Although it is desirable to obtain such information from the same tissue owing to large individual variations, combined measurement of many molecular and anatomical traits remains an unmet goal in biology despite the remarkable success of current pioneering methods.

Rapidly evolving tissue transformation and three-dimensional (3D) imaging approaches may enable holistic phenotyping of intact brains (Chung et al., 2013; Chung and Deisseroth, 2013; Renier et al., 2014; Susaki et al., 2014; Chen et al., 2015; Kim et al., 2015; Murray et al., 2015; Richardson and Lichtman, 2015; Ku et al., 2016; Pan et al., 2016; Tillberg et al., 2016; Murakami et al., 2018; Park et al., 2018). The objective of this chapter is to introduce a series of technologies (e.g., SWITCH, MAP, stochastic electrotransport, and SHIELD) that allow integrated multiscale imaging and molecular phenotyping of both animal tissues and human clinical samples. We discuss how these methods engineer (1) the physicochemical properties of brain tissues, (2) molecular interactions, and (3) molecular transport all together to achieve integrated brainwide molecular phenotyping at unprecedented speed and resolution. To enable immediate and broad adaptation of the technologies, we have made all associated reagents and protocols available to the scientific community. Detailed protocols and resources are freely available online at http://www.chunglabresources.org.

## Engineering Physicochemical Properties of Tissue

### SHIELD

SHIELD (Stabilization to Harsh conditions via Intramolecular Epoxide Linkages to prevent Degradation) is a versatile tissue-processing method that simultaneously preserves key molecular information—nucleic acids, protein fluorescence, and protein immunoreactivity—in cleared intact tissues by using a polyfunctional flexible epoxide crosslinker (Park, 2018). This chemical modifier performs several tasks: it renders individual biomolecules highly resistant to denaturation, protects their physicochemical properties (such as protein fluorescence) while minimally altering interactions with molecular probes (including antibodies), and secures biomolecules to their physiological location (Fig. 1). By screening a library of polyepoxides, we identified a structurally unique polyfunctional epoxide that shields the activity of fluorescent proteins against harsh environmental stressors. Based on physicochemical characterization and molecular dynamics calculations, we attributed the crosslinker's protective mechanism to the formation of multiple flexible intramolecular bonds that enhance the stability of proteins' tertiary structure. When applied to tissue, SHIELD enables uniform, organwide preservation of proteins and transcripts, their probe-binding properties, and fluorescent protein activity without loss of tissue architecture.

### SHIELD and MAP

Combining SHIELD with MAP (Magnified Analysis of the Proteome) (Ku et al., 2016) enables integrated circuit mapping at single-cell resolution (Fig. 2). To test this possibility, we genetically targeted parvalbumin (PV)–positive ($PV^+$) neurons in the globus pallidus externa (GPe) ($GPe\text{-}PV^+$) by injecting AAV-hSyn-DIO-mRuby2-Synaptophysin-EGFP virus into a *PV-Cre* transgenic mouse brain, which labeled neurites with mRuby2 and presynaptic boutons with EGFP (enhanced green fluorescent protein). We SHIELD-processed and cleared the intact mouse brain hemisphere with stochastic electrotransport (SE, discussed below) and imaged it using a light-sheet microscope to map the global projection pattern of $GPe\text{-}PV^+$ neurons. GFP-labeled synaptic terminals of the $mRuby2^+$ cells were found in the GPe, subthalamic nucleus (STN), substantia nigra reticulata (SNr), globus pallidus interna (GPi), nucleus reticularis thalami (nRT), caudate putamen (CPu), and parafascicular nucleus (PF).

To further investigate the PV-GPe circuit, we dissected a 1-mm-thick tissue block that included the GPe, STN, nRT, GPi, and SNr. We then performed fluorescent *in situ* hybridization (FISH) followed by immunostaining to map GAD1 (glutamate decarboxylase 1) messenger RNA (mRNA) and calretinin protein. Finally, the tissue was expanded using SHIELD-MAP for super-resolution volumetric imaging. To characterize the long-range output of a $GPe\text{-}PV^+$ neuron at single-cell resolution, we reconstructed the axonal arborization of an $mRuby2^+$ neuron. The exceptional preservation of fluorescent protein (FP) signal and enhanced resolution obtained with SHIELD-MAP enabled reliable reconstruction of individual axons and their presynaptic boutons. The resulting multidimensional axogram revealed that the reconstructed neuron is possibly connected to four neurons in the GPe, two neurons in the nRT, and 13 neurons in the SNr through axosomatic synapses. SHIELD is a highly

NOTES

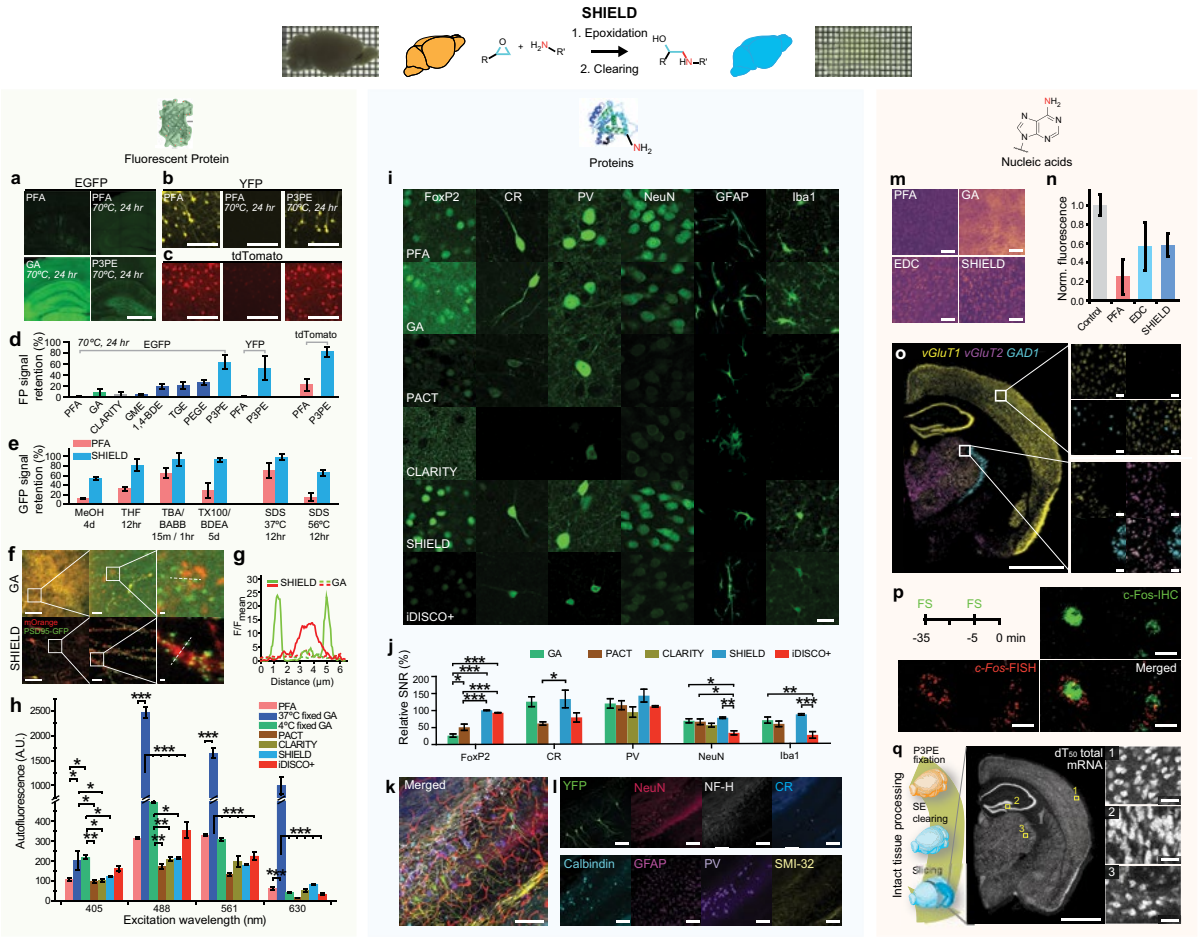


**Figure 1.** SHIELD preserves FP signals, proteins, transcripts, and their probe-binding affinities. ***a–c***, Representative FP signals of brain slices subjected to thermal treatment after being processed with fixatives (PFA, GA, or P3PE). Brain slices expressing EGFP (Thy1::EGFP M-line), yellow fluorescent protein (YFP) (Thy1::YFP H-line), or tdTomato (PV-Cre / loxP-tdTomato) were used. Scale bars: ***a***, 1 mm; ***b, c***: 100 μm. ***d***, FP signal retention after the same heat treatment in brain sections preserved with difference fixatives and CLARITY (a tissue-clearing technique that transforms tissue into a tissue–hydrogel hybrid). ***e***, GFP signal retention from M-line slices after exposure to organic solvents and detergents. MeOH, methanol; THF, tetrahydrofuran; TBA, *tert*-butyl alcohol; BABB, one part benzyl alcohol and two parts benzyl benzoate; TX100, Triton-X100; BDEA, butyldiethanolamine. $N = 3$. ***f***, Fluorescence images of neurons virally labeled with RV-hSyn-mOrange-p2A-PSD95-GFP in GA and SHIELD tissue. Scale bars: 100, 10, and 1 μm (left to right). ***g***, Fluorescence intensity profiles of PSD95-GFP and mOrange signals along the dotted lines in ***f***. ***h***, Tissue autofluorescence from various excitation wavelengths (405, 488, 561, and 630 nm excitation; emission detection window: +5 nm to +65 nm of the excitation wavelength). $N = 3$. ***i***, Representative images comparing the immunofluorescence of key cell-type antibodies in various tissue-processing methods. Scale bar, 20 μm. FoxP2, forkhead box protein P2; CR, calretinin; PV, parvalbumin; NeuN, neuronal nuclei; GFAP, glial fibrillary acidic protein; Iba1, ionized calcium-binding adapter molecule 1; PFA, paraformaldehyde; GA, glutaraldehyde; PACT, passive CLARITY technique; iDISCO, immunolabeling-enabled three-dimensional imaging of solvent-cleared organs. The same imaging and display settings were used for each antibody. ***j***, Signal-to-noise ratios (SNRs) of immunofluorescence in ***i*** normalized to the SNR of PFA control. $N = 3$. ***k, l,*** SHIELD preserves endogenous YFP fluorescence during multiple rounds of immunostaining and destaining. ***k***, Overlay of multiround immunostained images. Scale bar, 100 μm. ***l***, Images from individual rounds. Scale bar, 100 μm. ***m***, Representative heat maps showing FISH of total mRNAs by $(dT)_{50}$-Cy3 in cleared PFA, EDC-CLARITY, GA, and SHIELD tissues. Scale bar, 100 μm. ***n***, Fluorescence intensities of $dT_{50}$-Cy3 FISH normalized to the signal of uncleared PFA tissues (Control). $N = 3$. ***o***, Three-color FISH hybridization chain reaction (HCR) against vGluT1, vGluT2, and GAD1 mRNAs in SHIELD tissue. Scale bars, 1 mm (left); 50 μm (right). ***p***, Dual labeling of *c*-Fos protein and mRNA in SHIELD tissue from a mouse foot-shocked (FS) twice at 35 min and 5 min before sacrifice. Scale bars, 10 μm. ***q***, Uniform preservation of transcripts in a SHIELD-processed, SE-cleared brain hemisphere. A 1-mm-thick coronal block from the middle of the hemisphere was cut and stained with $dT_{50}$-Cy3 FISH. Scale bar, 2 mm (left); 100 μm (right). Error bars indicated SEM. One-way ANOVA; Tukey's multiple comparison test; $*p < 0.05$, $**p < 0.01$, $***p < 0.001$. Reprinted with permission from Park et al. (2018), Fig. 2. Copyright 2018, Springer Nature.

NOTES

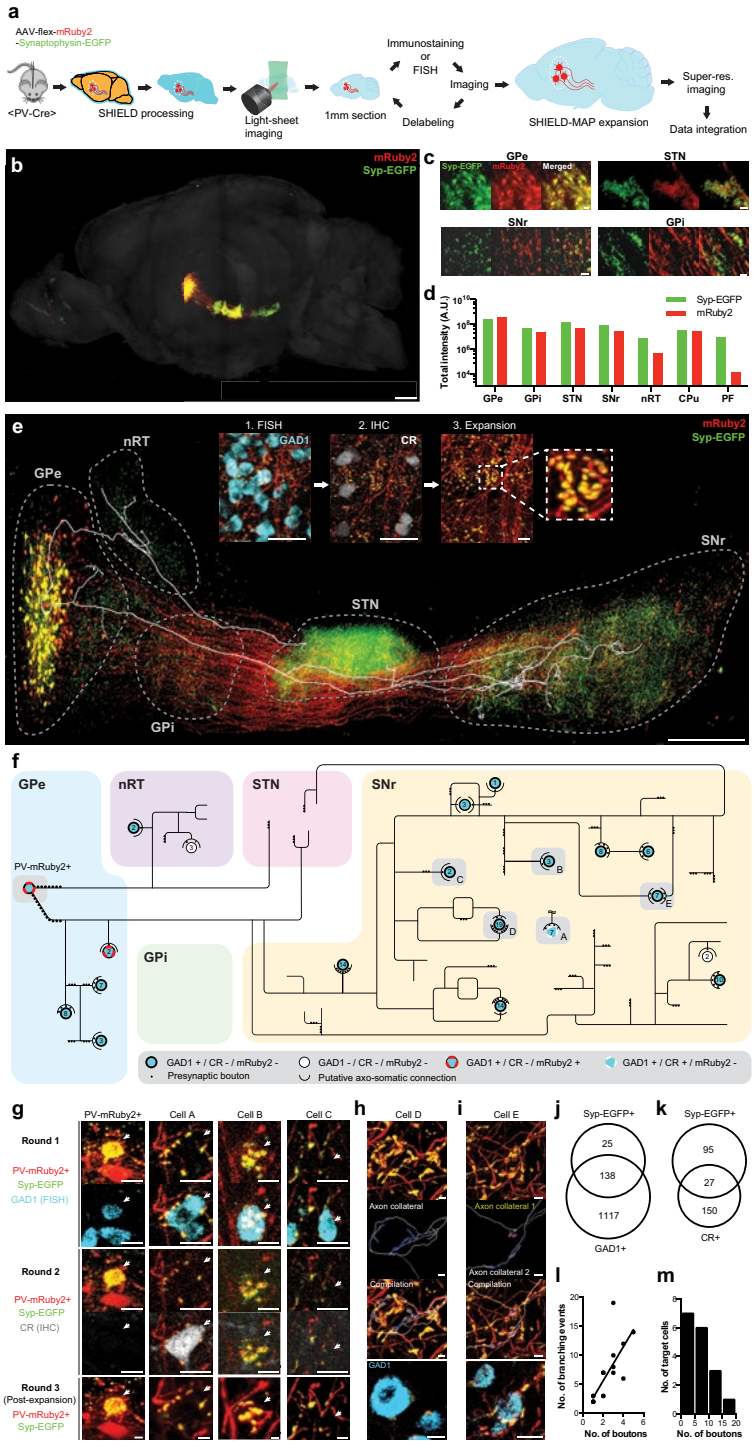


**Figure 2.** SHIELD combined with MAP and SE enables integrated circuit reconstruction at single-cell resolution. ***a***, Pipeline. ***b***, 3D rendering of the intact mouse hemisphere showing brainwide projection patterns of labeled GPe-PV$^+$ neurons. ***c***, Representative images of labeled neurons and their presynaptic terminals in GPe, STN, SNr, and GPi. ***d***, Total pixel intensity of mRuby2 and EGFP in seven brain regions to which the labeled GPe-PV$^+$ neurons project. ***e***, 3D rendering of labeled GPe-PV$^+$ neuronal circuitry with the overlaid axon trace of a single labeled neuron. Insets, Sample images from multiround staining and multiscale imaging. Scale bar, 1 mm (50 μm for insets). ***f***, Reconstructed axon arborization of the neuron and its downstream targets. Each circle represents a neuron. The number of putative axosomatic boutons is marked inside each circle. ***g***, Images of the circuit components from multiround imaging. Arrows indicate the target cell body. Scale bars, 20 μm. ***h***, Reconstructed putative axosomatic connectivity. Ramified axons (gray) and EGFP-positive presynaptic boutons (blue) are segmented. Scale bars, 20 μm. ***i***, Convergence of two axon collaterals branched remotely from the target cell body. ***j–k***, Venn diagram showing three different neuronal populations in the SNr. ***j***, GAD1$^+$/Syp-EGFP$^-$, GAD1$^+$/Syp-EGFP$^+$ and GAD1$^-$/Syp-EGFP$^+$ ***k***, CR$^+$/Syp-EGFP$^-$, CR$^+$Syp-EGFP$^+$ and CR$^-$/Syp-EGFP$^+$ Unbiased sampling was used. ***l***, Relationship between the number of axosomatic boutons and the axonal branching events of the reconstructed PV-mRuby2$^+$ neuron near the target neuronal soma. Linear regression, $R^2 = 0.55$; *F*-test = 17.40; $p = 0.0009$. ***m***, Distribution of the number of putative axosomatic boutons. Reprinted with permission from Park et al. (2018), Fig. 6. Copyright 2018, Springer Nature.

NOTES

versatile platform built on a rationally designed crosslinker with controllable molecular interactions, and it should find wide application in the study of complex biological systems.

### MAP

MAP (Ku et al., 2016) linearly magnifies organ architecture fourfold while preserving its 3D proteome organization. The magnified proteome library preserves both fine subcellular details and organ-scale intercellular connectivity. We achieved multiplexed labeling and imaging of a tissue's magnified proteome using off-the-shelf antibodies with an 82% success rate (100/122). With MAP, sample size can be reversibly modulated to accommodate proteomic imaging of interregional connections as well as fine synaptic architectures in the brain. Integrated multiscale mapping of the proteome within an intact tissue may enable new approaches for studying the organization and function of complex biological systems.

## Engineering Chemical Interactions: SWITCH

SWITCH stands for system-wide control of interaction time and kinetics of chemicals (Murray et al., 2015). It tightly controls a broad range of chemical reactions in tissue processing to achieve uniform sample treatment regardless of tissue size and type. SWITCH dynamically modulates chemical reaction kinetics to synchronize the reaction time between molecules throughout the system. This strategy enables all endogenous molecular targets in a large intact tissue to experience similar reaction conditions (time and concentration). As a result, large tissue can be uniformly processed.

We use a set of buffers in SWITCH. A SWITCH-On buffer facilitates chemical reactions between exogenous chemicals and endogenous biomolecules, and a SWITCH-Off buffer suppresses the reaction. SWITCH-mediated fixation transforms tissue into a heat-resistant and chemical-resistant hybrid while preserving tissue architecture, native molecules, and their antigenicity to a degree suitable for multiplexed proteomic imaging. For example, in SHIELD, we homogenously disperse the flexible epoxide crosslinker in tissue by suppressing epoxide reactivity in SWITCH-Off condition (4°C, pH 7.4) before initiating samplewide crosslinking by moving the sample to SWITCH-On condition (37°C, pH 10). This method does not require perfusion and is thus applicable to both animal and large human samples. In molecular labeling of the processed samples, SWITCH controls probe-target binding kinetics to improve probe penetration depth and the uniformity of molecular labeling. This method is simple, passive, and does not require any special equipment or reagents. Using SWITCH, we demonstrated that 22 rounds of molecular labeling datasets of a single banked postmortem human tissue can be precisely coregistered at single-cell resolutio.

## Engineering Chemical Transport: Stochastic Electrotransport

The transport of molecules is fundamental to life as well as many engineered systems. Brownian diffusion is among the most universal transport mechanisms, controlling a broad range of chemical and biological phenomena. In this type of transport, particles are dispersed via random thermal motion. Such passive diffusion is a simple and effective transport strategy for small-length-scale applications, but it becomes increasingly inefficient for macromolecules in a large-scale sample with a dense mesh architecture (e.g., biological tissues). For decades, the slow nature of Brownian diffusion has fundamentally limited the application of many powerful techniques in biology and medicine (e.g., immunohistology) to small-scale samples.

External forces can enhance transport if the surrounding matrix remains stable. For instance, hydrodynamic pressure can generate a convective flow in a highly porous matrix. However, for nanoporous soft meshes (e.g., biological tissues), the high pressure that is required to generate flow damages matrices. A stationary electrical gradient can enhance the transport of ions in a nanoporous matrix, but it also irreversibly deforms the matrix if the mesh is made of soft and charged polymeric materials. Therefore, a fundamentally new strategy is required to selectively boost the transport of freely moving ions without damaging the surrounding charged matrix.

To meet this challenge, we developed a new transport concept we termed "stochastic electrotransport" (Kim et al., 2015). Unlike a static electric field, a stochastically changing electric field induces an electrophoretically driven random walk of ions. We demonstrated theoretically and experimentally that during SE, the mean displacement of an ion scales quadratically with the product of the ion's electromobility and the field strength, whereas in electrophoretic one-dimensional transport, it scales linearly with the product of the two parameters. This unique quadratic dependence selectively boosts migration of only freely moving ions with high electromobility while suppressing the movement of a charged matrix with low electromobility. Therefore, the charged matrix remains virtually stationary while unbound ions disperse rapidly and selectively at a

NOTES

speed that is several orders of magnitude faster than Brownian diffusion. We have demonstrated that SE enables complete clearing or labeling of intact animal organs within 1 to 3 days (versus weeks to months using traditional methods).

## Conclusions

In this tutorial, we have demonstrated that we can engineer (1) the physicochemical properties of brain tissues, (2) molecular interactions, and (3) molecular transport all together to achieve integrated brainwide molecular phenotyping at unprecedented speed and resolution. SHIELD combined with SWITCH can effectively preserve endogenous molecules, protein fluorescence, and tissue architecture uniformly in both intact mouse hemispheres and long-banked clinical samples. SHIELD combined with pioneering genetic and viral tools may serve as a powerful platform for multiscale interrogation of neural circuits. In addition, we demonstrated that global projection patterns can be mapped brainwide using SHIELD followed by SHIELD-MAP for super-resolution imaging of regions of interest in the same brain to reconstruct individual axonal projections and synaptic structures. Integration of SHIELD with SE and light-sheet microscopy enables unbiased organwide visualization of FP and endogenous proteins. The pipeline enables complete processing of an intact mouse brain hemisphere from preservation, clearing, and immunolabeling to imaging within 10 days. These technologies synergize with a wide range of existing technologies and will enable new integrated approaches for studying complex biological systems. Detailed protocols and resources are freely available online at http://www.chunglabresources.org.

## References


Chen F, Tillberg PW, Boyden ES (2015) Optical imaging. Expansion microscopy. Science 347:543–548.

Chung K, Deisseroth K (2013) CLARITY for mapping the nervous system. Nat Methods 10:508–513.

Chung K, Wallace J, Kim SY, Kalyanasundaram S, Andalman AS, Davidson TJ, Mirzabekov JJ, Zalocusky KA, Mattis J, Denisin AK, Pak S, Bernstein H, Ramakrishnan C, Grosenick L, Gradinaru V, Deisseroth K (2013) Structural and molecular interrogation of intact biological systems. Nature 497:332–337.

Kim SY, Cho JH, Murray E, Bakh N, Choi H, Ohn K, Ruelas L, Hubbert A, McCue M, Vassallo SL, Keller PJ, Chung K (2015) Stochastic electrotransport selectively enhances the transport of highly electromobile molecules. Proc Natl Acad Sci USA 112:E6274-83.

Ku T, Swaney J, Park JY,, Albanese A, Murray E, Cho JH, Park YG, Mangena V, Chen J, Chung K (2016) Multiplexed and scalable super-resolution imaging of three-dimensional protein localization in size-adjustable tissues. Nat Biotechnol 34:973–981.

Murakami TC, Mano T, Saikawa S, Horiguchi SA, Shigeta D, Baba K, Sekiya H, Shimizu Y, Tanaka KF, Kiyonari H, Iino M, Mochizuki H, Tainaka K, Ueda HR (2018) A three-dimensional single-cell-resolution whole-brain atlas using CUBIC-X expansion microscopy and tissue clearing. Nat Neurosci 21:625–637.

Murray E, Cho JH, Goodwin D, Ku T, Swaney J, Kim SY, Choi H, Park YG, Park JY, Hubbert A, McCue M, Vassallo S, Bakh N, Frosch MP, Wedeen VJ, Seung HS, Chung K (2015) Simple, scalable proteomic imaging for high-dimensional profiling of intact systems. Cell 163:1500–1514.

Pan C, Cai R, Quacquarelli FP, Ghasemigharagoz A, Lourbopoulos A, Matryba P, Plesnila N, Dichgans M, Hellal F, Ertürk A (2016) Shrinkage-mediated imaging of entire organs and organisms using uDISCO. Nat Methods 13:859–867.

Park YG, Sohn CH, Chen R, McCue M, Yun DH, Drummond GT, Ku T, Evans NB, Oak HC, Trieu W, Choi H, Jin X, Lilascharoen V, Wang J, Truttmann MC, Qi HW, Ploegh HL, Golub TR, Chen SC, Frosch MP, et al. (2018) Protection of tissue physicochemical properties using polyfunctional crosslinkers. Nat Biotechnol. doi: nbt.4281.

Renier N, Wu Z, Simon DJ, Yang J, Ariel P, Tessier-Lavigne M (2014) iDISCO: a simple, rapid method to immunolabel large tissue samples for volume imaging. Cell 159:896–910.

Richardson DS, Lichtman JW (2015) Clarifying tissue clearing. Cell 162:246–257.

Susaki EA, Tainaka K, Perrin D, Kishino F, Tawara T, Watanabe TM, Yokoyama C, Onoe H, Eguchi M, Yamaguchi S, Abe T, Kiyonari H, Shimizu Y, Miyawaki A, Yokota H, Ueda HR (2014). Whole-brain imaging with single-cell resolution using chemical cocktails and computational analysis. Cell 157:726–739.

Tillberg PW, Chen F, Piatkevich KD, Zhao Y, Yu CC, English BP, Gao L, Martorell A, Suk HJ, Yoshida F, DeGennaro EM, Roossien DH, Gong G, Seneviratne U, Tannenbaum SR, Desimone R, Cai D, Boyden ES (2016) Protein-retention expansion microscopy of cells and tissues labeled using standard fluorescent proteins and antibodies. Nat Biotechnol 34:987–992.

# Holographic Illumination for Two-Photon Optogenetics

Dimitrii Tanese, PhD, and Valentina Emiliani, PhD

Wavefront-Engineering Microscopy Group
Photonics Department
Research Center Vision Institute
Unités Mixtes de Recherche 968
Sorbonne Université
Institut National de la Santé et de la Recherche Médicale
Centre National de la Recherche Scientifique
Paris, France

NOTES

## Introduction

Light patterning through spatial light modulators (SLMs), whether they modulate amplitude or phase, is gaining an important place within optical methods used in neuroscience, especially for manipulating neuronal activity with optogenetics. The ability to selectively direct light in specific neurons expressing an optogenetic actuator, rather than in a large neuronal population within the microscope field of view, is becoming attractive for studies that require high spatiotemporal precision for perturbing neuronal activity in a microcircuit. Computer-generated holography (CGH) is a phase-modulation light-patterning method that provides significant advantages in terms of spatial and temporal resolution of photostimulation. It offers flexible three-dimensional (3D) light illumination schemes that are easily reconfigurable, is able to address a significant excitation field simultaneously, and is applicable to both visible and infrared light excitation. Its implementation complexity depends on the level of accuracy that a certain application demands: CGH can stand alone or be combined with temporal focusing (TF) in two-photon (2P) excitation schemes, producing depth-resolved excitation patterns that are robust to scattering. In this chapter, we present an overview of CGH's properties regarding spatiotemporal resolution and penetration depth, particularly focusing on its applications in optogenetics. The coordinated activation of neuronal microcircuits is proposed to regulate brain functioning in health and disease. A common approach to investigate the mechanisms that reduce network complexity is to outline microcircuits and infer their functional role by selectively modulating them. Combined with suitable illumination approaches, today optogenetics offers the possibility of achieving such selective control with its ever-growing toolbox of reporters and actuators.

Wide-field single-photon (1P) illumination was the first method employed to activate optogenetic actuators (Boyden et al., 2005; Nagel et al., 2005; Adamantidis et al., 2007; Aravanis et al., 2007; Gradinaru et al., 2007; Zhang et al., 2007; Huber et al., 2008; Anikeeva et al., 2012) and continues to be widely used for neural circuit dissection (Makinson et al., 2017; Weible et al., 2017). Using genetic tools, including viruses, Cre-dependent systems, and transgenic lines to target optogenetic actuators to neurons of interest, investigators have used wide-field illumination to dissect correlation and causal interactions in neuronal subpopulations both *in vitro* (Petreanu et al., 2007, 2009; Joshi et al., 2016; Morgenstern et al., 2016; Tovote et al., 2016) and *in vivo* (Adesnik et al., 2012; Atallah et al., 2012; Lee et al., 2012; Tovote et al., 2016). With this approach, population specificity is achieved through genetic targeting, and temporal resolution and precision are limited only by the channels' temporal kinetics and cell properties (e.g., opsin expression level and membrane potential). Suitable combinations of opsins have also enabled independent optical excitation of distinct cell populations (Klapoetke et al., 2014). The primary drawback of wide-field illumination is that all opsin-expressing neurons are stimulated simultaneously, and thus, wide-field schemes lack the temporal flexibility and spatial precision necessary to mimic the spatiotemporal distribution of naturally occurring microcircuit activity.

Replacing 1P visible light excitation with 2P near-infrared light illumination enables improved axial resolution and penetration depth (Denk et al., 1990). However, the small single-channel conductance of actuators such as channelrhodopsin-2 (ChR2) (40–80 fS) (Feldbauer et al., 2009), combined with the low number of channels excitable within a femtoliter 2P focal volume, makes it difficult to generate photocurrents strong enough to bring a neuron to the firing threshold. This challenge has prompted the development of 2P-stimulation approaches that increase the excitation volume.

2P-stimulation approaches for optogenetics can be grouped into two main categories: scanning and parallel excitation techniques. 2P laser scanning methods use galvanometric mirrors to quickly scan a laser beam across several positions covering a single cell or multiple cells (Rickgauer and Tank, 2009; Andrasfalvy et al., 2010; Prakash et al., 2012). Parallel approaches enable investigators to simultaneously cover the surface of a single cell or multiple cells using either beams with low numerical aperture (NA) (Andrasfalvy et al., 2010; Rickgauer et al., 2014) or CGH (Bègue et al., 2013; Chaigneau et al., 2016; Ronzitti et al., 2017a) and generalized phase contrast (Papagiakoumou et al., 2010). In this chapter, we will focus on the description of CGH and its application to optogenetic neuronal control. A broader overview of the different approaches to 2P optogenetics can be found in Oron et al. (2012), Vaziri and Emiliani (2012), Packer et al. (2013), Bovetti and Fellin (2015), Ronzitti et al. (2017b), and Chen et al. (2018).

## Computer-Generated Holography

The experimental scheme for CGH (Fig. 1*a*) was originally proposed for generating multiple optical

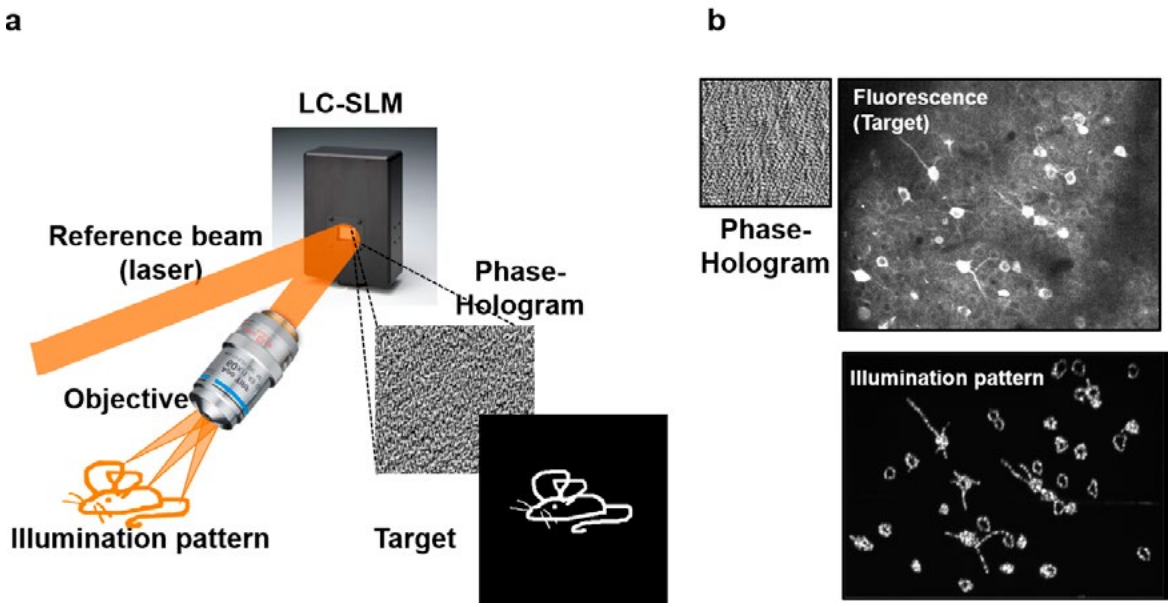


**Figure 1**. Computer-generated holography. ***a***, In CGH, an arbitrary light distribution (target) is used as the input source for a Fourier transform–based iterative algorithm to calculate the interference pattern or phase hologram, which, after interfering with the reference beam (laser) at the diffraction plane, would reproduce the target at the imaging plane. The calculated phase hologram is addressed to an LC-SLM. After diffraction through the LC-SLM, the reference beam plane will generate a light distribution (illumination pattern) at the objective focal plane, reproducing the original target shape. ***b***, For precise light stimulation, the whole fluorescence image or a defined region of interest can be used to select the excitation targets that will be sent to the iterative algorithm for producing the corresponding phase hologram. Reprinted with permission from Papagiakoumou et al. (2018), Fig. 1. Copyright 2018, Springer Science+Business Media LLC.

gradient traps (also called optical tweezers) (Curtis et al., 2002). It consists of computing with a Fourier transform–based iterative algorithm (Gerchberg and Saxton, 1972) the interference pattern or phase hologram that back-propagating light from a defined target (input image) will form with a reference beam on a defined "diffractive" plane. Next, the computer-generated phase hologram is converted into a gray-scale image and then addressed to a liquid-crystal (LC) matrix SLM, which is placed at the diffractive plane. In this way, each pixel of the phase hologram controls (in proportion to the corresponding gray-scale level) the voltage applied across the corresponding pixel of the LC matrix so that the refractive index, and thus the phase modulation, of each pixel can be precisely modulated. As a result, the calculated phase hologram is converted into a pixelated refractive screen, and illumination of the screen with the laser (or reference) beam will generate a light pattern at the objective focal plane that reproduces the desired template. This template can be any kind of light distribution in two dimensions (2D) or 3D, ranging from diffraction-limited spots or larger spots (with a larger surface area) to arbitrary extended light patterns.

Precise manipulation of neuronal activity via holographic light patterns requires an accurate control of the spatial colocalization between the generated light pattern and the target. To do so, a few years ago we proposed a way to generate the template for calculating phase holograms on the base of the fluorescence image (Lutz et al., 2008). Briefly, a fluorescence image of the preparation is recorded and used to draw the excitation pattern. In this way, it is possible to generate a holographic laser pattern reproducing the fluorescence image or a user-defined region of interest (Fig. 1*b*) (Oron et al., 2012; Papagiakoumou, 2013).

In CGH, the pixel size and number of pixels of the LC-SLM define the lateral and axial field of excitation (FOE). The maximum lateral FOE ($FOE_{xy}$) is expressed as follows (Golan et al., 2009; Yang et al., 2011; Hernandez et al., 2016):

$$FOE_{xy} = \Delta X \times \Delta Y = \left(2 \cdot \frac{\lambda f_{eq}}{2dn}\right) \times \left(2 \cdot \frac{\lambda f_{eq}}{2dn}\right), \quad (1)$$

where λ is the excitation wavelength, $d$ is the LC-SLM pixel size, $n$ is the medium refractive index, and feq is the equivalent focal lens, including all the lenses located between the LC-SLM and the sample plane.

Within this region, the diffraction efficiency, $\delta(x,y)$, defined as the intensity ratio of the incoming to the

diffracted beam, depends on the lateral spot-position coordinates, $x$, $y$:

$$\delta(x,y) = b\left(sinc^2\left(\frac{\pi d}{\lambda f_{eq}}x\right)sinc^2\left(\frac{\pi d}{\lambda f_{eq}}y\right)\right), \quad (2)$$

with $b$ being a proportionality factor considering the frontal window LC-SLM reflectivity. Consequently, $\delta(x, y)$ reaches its maximum value at the center of the $FOE_{xy}$ and its minimum value at the borders of the $FOE_{xy}$. Nowadays, existing LC-SLM devices are able to reach diffraction efficiency values of ~95% at the center and ~38% at the border—values close to the theoretical limits. The remaining light is distributed among the higher-diffraction orders and an undiffracted component (so-called zero-order), resulting in a tightly focused spot at the center of the FOE. Depending on the applied phase profile, the intensity of the zero-order spot can reach 25% of the input light. This value can be reduced to 2–5%, regardless of the projected hologram, by performing *ad hoc* precompensation of the LC-SLM-phase pixel values (Ronzitti et al., 2012). Although the focused zero-order spot can be removed from the FOE by adding a block or diaphragm at a plane conjugated to the sample plane (Polin et al., 2005; Zahid et al., 2010), doing so limits the accessible FOE. Alternatively, the intensity of the zero-order component can be strongly reduced by using a cylindrical lens placed in front of the LC-SLM, which stretches the zero-order spot into a line (Hernandez et al., 2014). A phase hologram compensating for the cylindrical lens effect is then addressed onto the LC-SLM in addition to the original phase hologram generating the target spot so that the holographic pattern shape is restored (Fig. 2). Importantly, the use of cylindrical lenses enables removing the zero-order component from the $FOE_{xy}$ without using intermediate blocks, thus enabling access to the entire FOE.

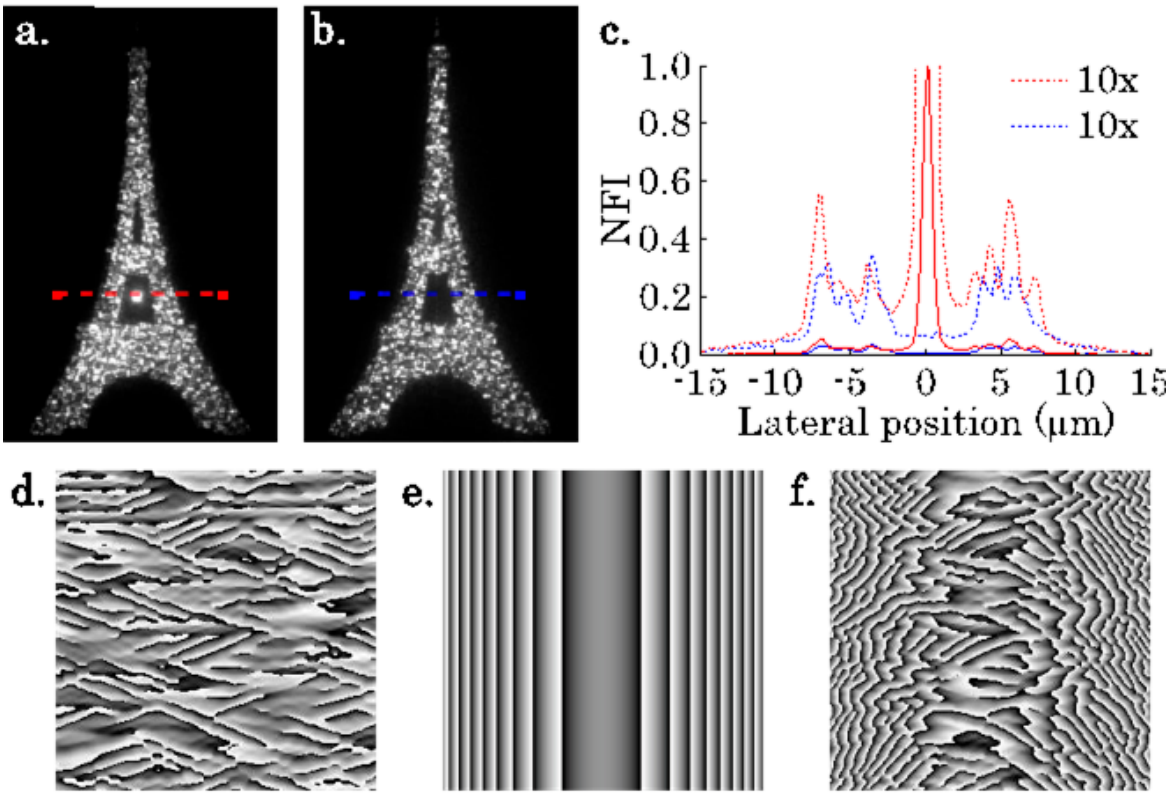


**Figure 2.** Zero-order spot removal using cylindrical lenses. Comparison between a CGH image of the Eiffel Tower (***a***) without and (***b***) with a single 1 m cylindrical lens, aberrating the zero-order in the optical path. ***c***, 2P normalized fluorescence intensity (NFI) profiles along the lines drawn in ***a***, red, and ***b***, blue. Dotted lines represent the signal of solid lines multiplied by 10 for a better view. ***d***, Phase mask reproducing the image of the Eiffel Tower at the focal plane of the objective, calculated with a Gerchberg–Saxton algorithm. ***e***, Conjugated cylindrical Fresnel lens hologram added to that of ***d*** for aberration compensation. ***f***, Final corrected phase mask addressed to the SLM. Reprinted with permission from Hernandez et al. (2014), Fig. 2. Copyright 2014, The Optical Society.

NOTES

Intensity inhomogeneities due to diffraction efficiency are a limiting factor for applications requiring lateral displacement of a single spot or multiple spots within the FOE. Therefore, we have proposed approaches that compensate for these inhomogeneities by keeping the spot intensity constant, independently on the lateral position. In the case of single-spot generation, homogenization of light distribution can be achieved by projecting one or multiple spots outside the $FOE_{xy}$ and tuning their brightness or size to compensate for the intensity loss due to the diffraction efficiency curve. Thus, a constant intensity value in the excitation spot is maintained for each position of the $FOE_{xy}$. The extra spots can be blocked by adding an external diaphragm placed at an intermediate imaging plane of the optical system, conjugated to the sample plane (Hernandez et al., 2016). For multispot excitation, one can use graded input images to generate brighter spots into regions that border the FOE, where the diffraction efficiency is lower, and dimmer spots into the central part of the FOE, where diffraction efficiency is higher (Conti et al., 2016; Koshelev et al., 2016; Shemesh et al., 2017). Graded input patterns can also be used to compensate for sample inhomogeneity. For example, they can be applied to equalize photocurrents from cells with different expression levels (Conti et al., 2016).

CGH pattern generation also suffers from "speckle": undesired intensity variations of high spatial frequency within the same spot. This is an intrinsic limitation of CGH that results from phase discontinuities at the sample plane inherent in the Gerchberg–Saxton algorithm (Gerchberg and Saxton, 1972), the most commonly used Fourier transform–based iterative algorithm. Speckle fluctuations reach 20% in 1P CGH and 50% in 2P CGH implementations. Different approaches have been proposed to reduce or eliminate speckles, each with their advantages and limitations. Temporally averaging speckle patterns can be achieved by mechanically rotating a diffuser (Papagiakoumou et al., 2008) or by generating multiple shifted versions of a single hologram (Golan and Shoham, 2009). Also, smoother intensity profiles can be created using *ad hoc* algorithms that remove phase vortices in the holographic phase mask (Guillon et al., 2017). Alternatively, the interferometric method known as generalized phase contrast (GPC) (Glückstad, 1996) has proven to generate speckle-free 2D extended shapes with the necessary precision, e.g., to precisely reproduce the shape of a thin dendritic process (Papagiakoumou et al., 2010). Recently, researchers have shown that GPC can also be extended to 3D by combining it with CGH, an approach called Holo-GPC (holographic generalized phase contrast) (Bañas and Glückstad, 2017). In this case, a holographic phase mask is used to multiplex a GPC pattern in different lateral or axial positions.

## Spatial resolution

In general, the lateral spatial resolution of an optical microscope is defined by the maximum spatial frequency that can be transferred through the focusing objective. This frequency is related to the maximum angle of convergence of the illumination rays, i.e., to the objective angular aperture. Consequently, in CGH, the smallest obtainable illumination pattern is a diffraction-limited Gaussian spot whose full width at half maximum (FWHM) is equal to $\Delta x \approx \lambda/NA_{eff}$, where $NA_{eff}$ is the effective NA (with $NA_{eff}$ < NA for an underfilled pupil). Along with the concept of resolution, it is useful to introduce the notion of spatial localization accuracy, i.e., the precision with which one can target a certain position in the sample plane (Schmitz et al., 2005). Spatial localization accuracy is ultimately related to the minimum displacement, $\Delta\delta_{min}$, of the illumination spot that is possibly achieved by spatially modulating the phase of the incoming light beam. In particular, an illumination spot can be laterally shifted by a certain step $\Delta\delta$ by applying at the objective's back aperture a prism-like phase modulation of slope $\alpha \approx \Delta\delta f_{obj}$ , where $f_{obj}$ is the objective focal length. The spatial localization accuracy therefore depends on the SLM's ability to approximate a prism-like phase shift (Schmitz et al., 2005). This ability is ultimately limited by the number of pixels, $N$, and gray levels, $g$, of the SLM. More precisely, the theoretical upper limit for the minimum step $\Delta\delta_{min}$ is inversely proportional to $N \cdot g$ (Schmitz et al., 2005; Engström et al., 2008).

In CGH, axial resolution scales linearly with the lateral spot size, and inversely with the objective *NA*. To be precise, if the holographic spot radius is defined as $s$, and the speckle size is $\sigma \approx \lambda/(NA\sqrt{8 \cdot \ln(2)})$, then the 1P and 2P axial resolution is twice the axial distance, $\Delta z$, at which the 2P intensity drops at 50% FWHM, where $\Delta z$ is given by:

$$\Delta z(s)_{1P} = \frac{2\sqrt{3}z_R\sigma}{\sqrt{s^2+\sigma^2}};\ \Delta z(s)_{2P} = \frac{2z_R\sigma}{\sqrt{s^2+\sigma^2}}, \qquad (3)$$

with $z_R = \pi \cdot s^2/2\lambda$. This means that a spot size of 10 µm wide would correspond to an axial resolution of 14 µm using an NA = 0.9 objective and 2P illumination at 900 nm (Hernandez Cubero, 2016). The corresponding illumination volume would be roughly the size of a cell soma (yellow circle,

NOTES

Fig. 3*a*), thereby enabling (in principle) optical photostimulation with single-cell precision.

Optical stimulation with near cellular resolution was indeed achieved in freely moving mice using 1P holographic stimulation (Szabo et al., 2014). Briefly, holographic light patterning coupled to a fiber bundle with a micro-objective at the end was used to photostimulate and monitor functional responses in cerebellar molecular layer interneurons coexpressing a calcium indicator (GCaMP5-G) and an opsin (ChR2-tdTomato) in freely behaving mice (Fig. 4). These

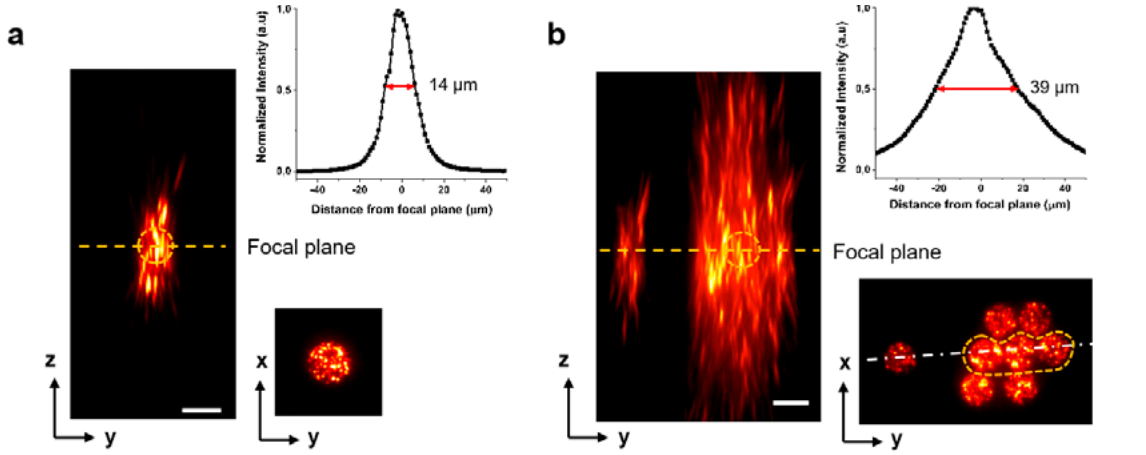


**Figure 3.** Axial propagation of holographic beams. Experimental *y–z* and *x–y* intensity cross-sections for holographic beams generated to produce at the objective focal plane (***a***) a circular spot or (***b***) multiple spots of 10 µm diameter. The *y–z* cross-section in ***b*** is shown along the white dashed-dotted line. The yellow circle in both panels approximates the size of a cell soma. Integrated-intensity profiles of *y–z* cross-sections around the circular spot (***a***) and in an area covering three spots (dashed yellow line) of the multispot light configuration (***b***) are shown on the top of the panels. For comparison, the FWHM of the axial integrated-intensity profile of the single 10 µm spot is ~14 µm. Scale bars, 10 µm. Reprinted with permission from Papagiakoumou et al (2018), Fig. 4. Copyright 2018, Springer Science+Business Media LLC.

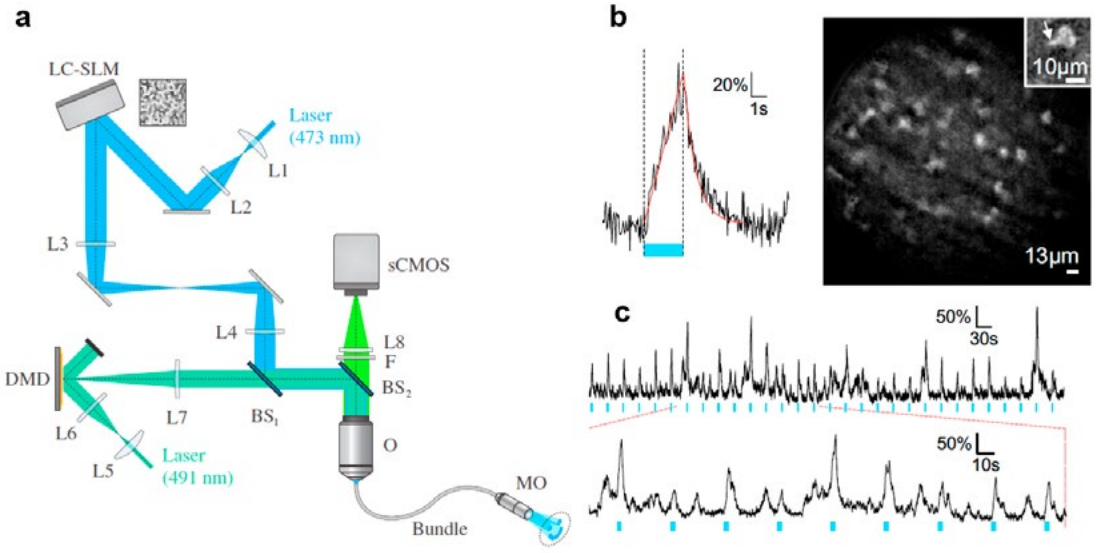


**Figure 4.** Holographic photostimulation and functional imaging in freely behaving mice. ***a***, Schematic of the holographic fiberscope comprising two illumination paths: one for photoactivation with CGH, including an LC-SLM, and a second for fluorescence imaging, including a digital micromirror device (DMD). Backward fluorescence was detected on a scientific complementary metal oxide semiconductor (sCMOS) camera. Both paths were coupled to the sample using a fiber bundle attached to a micro-objective (MO). L, Lens; BS, beam splitter; F, emission filter; O, microscope objective. ***b***, Left, Calcium signal triggered by photoactivation (blue line; photostimulation power, 50 mW/mm$^2$) with a 5-µm-diameter holographic spot placed on the soma of a ChR2-expressing cell recorded in a freely behaving mouse coexpressing GCaMP5-G and ChR2 in cerebellar molecular layer interneurons. Right, Structure illumination image recorded in a freely behaving mouse and showing molecular layer interneuron somata and a portion of a dendrite (inset). Scale bar, 10 µm. ***c***, Top, The same photoactivation protocol as in (***a***) was repeated every 30 s for 15 min (photostimulation power, 50 mW/mm$^2$; imaging power, 0.28 mW/mm$^2$). Bottom, Expansion of the top trace showing that spontaneous activity frequently occurs between evoked transients. Adapted with permission from Szabo et al. (2014), Figs. 1*A*, 5*C*, 6*A*, and 6*C*. Copyright 2014, Elsevier.

NOTES

experiments showed that optical photostimulation could achieve near cellular resolution using sparse staining and sparse distribution of excitation spots. However, a similar approach would not reach the same precision if applied to multisite photostimulation of a densely labeled neuronal population; as seen in Figure 3*b*, the axial resolution would quickly deteriorate using both 1P and 2P excitation.

A few years ago, we demonstrated that micrometer-size optical sectioning, independent of the lateral spot dimension (Papagiakoumou et al., 2008), can be achieved by combining CGH and GPC with TF. Briefly, the technique of TF, originally demonstrated to perform wide-field 2P microscopy (Oron et al., 2005; Zhu et al., 2005), uses a dispersive grating to diffract the different frequencies comprising the ultrashort excitation pulse in different directions. The various frequencies thus propagate toward the objective focal plane at different angles so that the pulse is temporally smeared above and below the focal plane, which remains the only region irradiated at peak-power efficiency for 2P excitation.

TF and CGH can be combined by adding an LC-SLM and a focusing lens (L1) to the conventional TF optical path so that the TF grating lies at the focal plane of L1 and is illuminated by the holographic pattern. A second telescope, made by a second lens (L2) and the objective, conjugates the TF plane with the sample plane, enabling the generation of spatiotemporally focused patterns (Fig. 5*a*). Notably, TF enables decoupling lateral and axial resolution so that the same axial resolution is achieved independently on the lateral extension of the excitation spot (Figs. 5*b*,*c*) (Papagiakoumou et al., 2008). Also, using TF combined with low-NA Gaussian beams, GPC and CGH has enabled efficient 2P optogenetic excitation with micrometer axial resolution and millisecond temporal resolution both *in vitro* and *in vivo* (Andrasfalvy et al., 2010; Papagiakoumou et al., 2010; Bègue et al., 2013; Rickgauer et al., 2014).

Although wavefront shaping and TF enable precise sculpting of the excitation volume, the ultimate spatial precision achievable for 2P optogenetics also depends on the opsin distribution within the

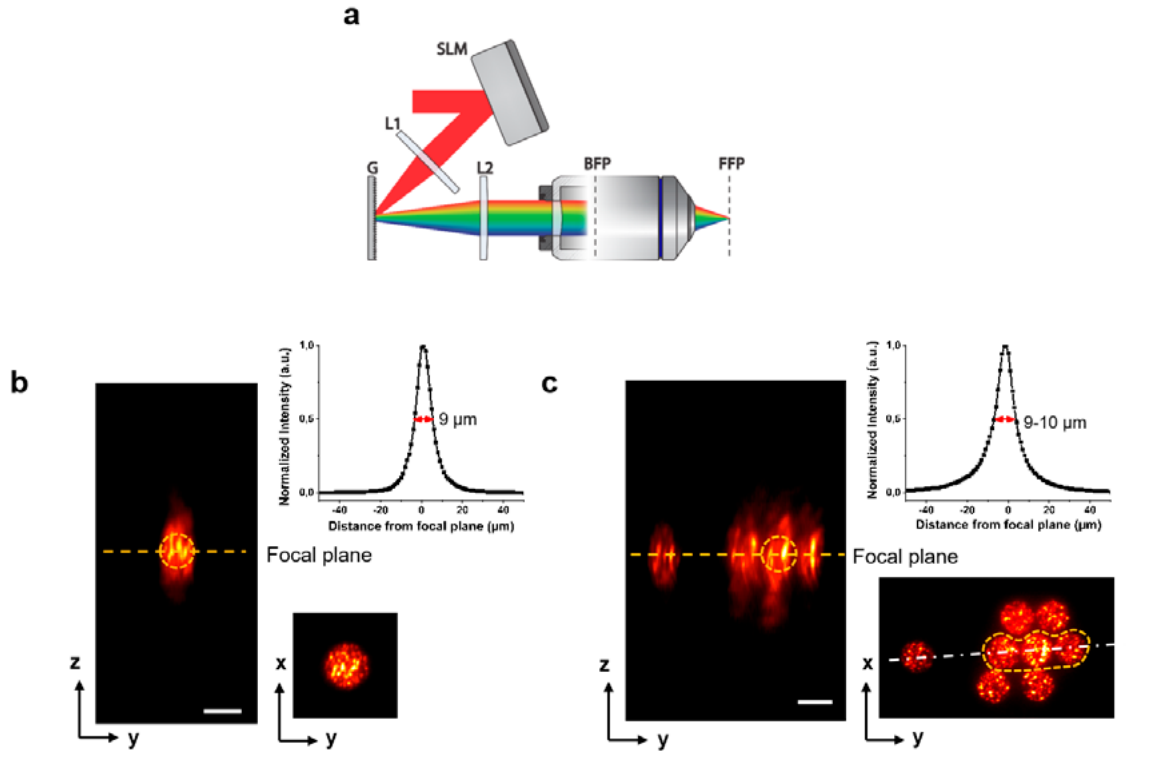


**Figure 5.** ***a***, Schematic representation of an experimental setup combining CGH with TF. G, grating; L1 and L2, lenses; BFP, Back focal plane; FFP, Front focal plane. ***b–c***, Experimental *y–z* and *x–y* intensity cross-sections for temporally focused holographic beams generated to produce at the objective focal plane a circular spot (***b***) or multiple spots of 10 µm diameter (***c***). *y–z* cross-section in (***c***) is shown along the white dashed-dotted line. Yellow circles approximate the size of a cell soma. Top panels, Integrated-intensity profiles of *y–z* cross-sections around the circular spot (***b***) and in an area covering three spots (dashed yellow line) of the multispot light configuration (***c***). For comparison, the FWHM of the axial integrated-intensity profile of the single 10 µm spot is ~9 µm. Thanks to TF, the axial confinement is well preserved even when multiple spots are projected close together. Scale bars: ***b–c***, 10 µm. Reprinted with permission from Papagiakoumou et al (2018), Fig. 5. Copyright 2018, Springer Science+Business Media LLC.

NOTES

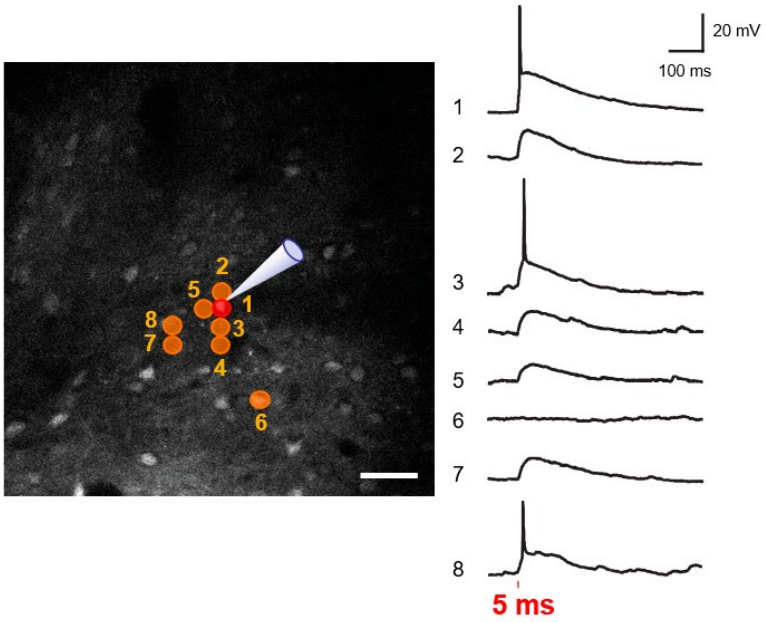


**Figure 6.** 2P holographic photostimulation of ReaChR-expressing cells *in vivo*. The opsin ReaChR was expressed in neurons at layer 2/3 of mouse visual cortex by injecting the viral vector rAAV1-Ef1α-ReaChR-P2A-tdTomato. Positive neurons expressing ReaChR (left panel, fluorescent cells in the 2P fluorescence image) in isoflurane-anesthetized mouse were photostimulated with a 12-μm-diameter excitation spot for 5 ms illumination duration at 0.15 mW/μm$^2$ and $\lambda$ = 1030 nm (left panel, red shaded area). APs were induced by holographic excitation of one positive cell soma (spot 1), whose membrane potential was measured using 2P-guided whole-cell recording (trace 1). Subthreshold or suprathreshold activation was induced in the patched cell (traces 2–8) upon holographic excitation of spots targeting the cell's soma at radial distances from spot 1 of 12 μm (spot 2), 12 μm (spot 3), 24 μm (spot 4), 12 μm (spot 5), 67.6 μm (spot 6), 40.4 μm (spot 7), and 35 μm (spot 8). Activation was caused by exciting opsin channels distributed into axon, proximal, and distal dendrites of the patched neuron. Scale bar, 40 μm; calibration: 20 mV, 100 ms. Reprinted with permission from Papagiakoumou et al (2018), Fig. 7. Copyright 2018, Springer Science+Business Media LLC.

expressing neurons: opsins are efficiently trafficked to the membranes of cell soma, as well as to dendrites and axons. Consequently, illumination with a theoretically micrometer-sized focal volume could depolarize all cells whose processes (dendrites and axons) cross the target excitation volume, even if their somata were located micrometers away from the illumination spot (Fig. 6). This activation crosstalk needs to be carefully considered, for example, when performing connectivity experiments. It could prevent investigators from distinguishing whether a postsynaptic response, recorded while photostimulating a presynaptic cell, originated from a true connection between the two cells rather than from direct stimulation of postsynaptic dendrites or axons crossing the photostimulation volume. Reaching a true cellular resolution for exciting densely labeled samples requires combining optical focusing with molecular strategies that enable confined opsin expression in restricted cell areas (e.g., soma or axonal hillock) (Baker et al., 2016; Shemesh et al., 2017; Mardinly et al., 2018).

## Temporal resolution

Parallel light illumination enables simultaneous excitation of all selected targets. Temporal resolution is therefore limited only by the illumination time needed to evoke, e.g., an action potential (AP), a detectable $Ca^{2+}$ response, or a defined behavioral change (Oron et al., 2012; Vaziri and Emiliani, 2012). The illumination time ultimately depends on opsin conductance, virus promoter, serotype, titer, kinetics parameters, and excitation power. In the following discussion, we will specifically review how the opsin kinetics parameters determine temporal resolution, temporal precision (temporal jitter), and AP spiking rate.

Light illumination of an opsin-expressing cell with a hundred-millisecond illumination pulse generates a characteristic photocurrent trace (Fig. 7*a*) in which one can distinguish an activation, inactivation, and deactivation part characterized by temporal decay: $\tau_{on}$, $\tau_{inact}$, and $\tau_{off}$, respectively. The overall kinetics of the current, as well as its ratio of peak to plateau, can be qualitatively reproduced using a three-state or four-state model (Nagel et al., 2003; Hegemann et al., 2005; Nikolic et al., 2006, 2009; Williams et al., 2013) (Fig. 7*b*). The four-state model is more accurate for reproducing the biexponential decay of the light-off current and the photocurrent voltage dependence (Williams et al., 2013). A qualitative value for the characteristic temporal decay, $\tau_{on}$,

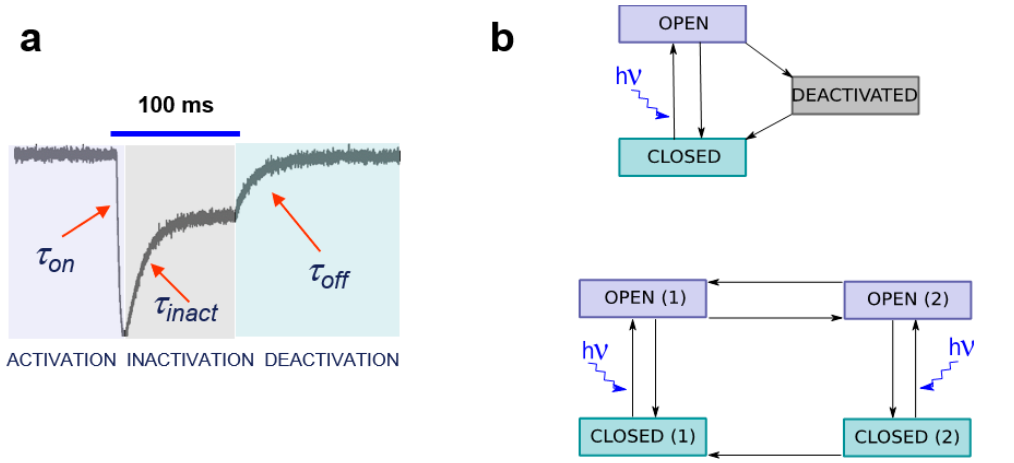


**Figure 7.** ChR2 photocurrent and photocycle. ***a***, Typical photocurrent trace of a CHO cell expressing ChR2 under visible light illumination (1P excitation) for 100 ms. ***b***, Top, schematic of the three-state model comprising the closed/ground state, the open state, and the closed/desensitized state. Bottom, Schematic of the four-state model with two closed and two open states. hυ, incident photon. For a detailed description of the model, see Nikolic et al. (2009). Reprinted with permission from Papagiakoumou et al (2018), Fig. 8. Copyright 2018, Springer Science+Business Media LLC.

$\tau_{inact}$, and $\tau_{off}$, can be directly extracted by assuming a monoexponential process for the three transitions. In Table 1, we report the values of $\tau_{on}$ (at saturation), $\tau_{inact}$, and $\tau_{off}$, measured under 2P holographic illumination of Chinese hamster ovary (CHO) cells expressing a fast (Chronos) (Klapoetke et al., 2014), an intermediate (CoChR) (Klapoetke et al., 2014), and a slow (ReaChR) (Lin et al., 2013) opsin.

| | Chronos | CoChR | ReaChR |
|---|---|---|---|
| $\tau_{on}$ (ms) | 0.73 | 2.4 | 8 |
| $\tau_{inact}$ (ms) | 9.3 | 200 | 443 |
| $\tau_{off}$ (ms) | 4.2 | 31 | 94 |

**Table 1**. Kinetics parameters for different opsins. Chronos, CoChR, and ReaChR were expressed in CHO cells and excited using 2P ($\lambda$ = 950 nm; pulse duration 4 s for ReaChR and CoChR, and 1 s for Chronos; power = 0.05–1.1 mW/μm$^2$). The current curves at saturation (the power at which the peak current reaches 90% of its maximum) were fitted using a monoexponential decay for the three transitions: activation, inactivation, and deactivation. The corresponding decay times, $\tau_{on}$ (ms), $\tau_{off}$ (ms), and $\tau_{inact}$ (ms), are reported in the table and correspond to power close to saturation (0.86 mW/μm$^2$, 0.54 mW/μm$^2$, and 0.28 mW/μm$^2$ for Chronos, CoChR, and ReaChR, respectively). Adapted with permission from A. Picot, M. Gajowa, et al., unpublished observations.

In practice, the efficient current integration obtained under parallel photostimulation enables using photostimulation pulses much shorter than the channel rise time. This enables *in vitro* AP generation at millisecond temporal resolution (Fig. 8*a*) (Chaigneau et al., 2016; Ronzitti et al., 2017a) and submillisecond temporal jitter (Chaigneau et al., 2016; Ronzitti et al., 2017a; Shemesh et al., 2017), independently on $\tau_{on}$. Conversely, the value of $\tau_{off}$ has a key role in limiting the achievable spiking rate, as shown in Figure 8*b*, which displays *in vitro* spike generation under 2P holographic illumination of interneurons (layer 2/3 of visual cortex) expressing different opsins (Chronos, ReaChR, and CoChR). Fast opsins, such as Chronos, enabled generation of light-evoked AP trains at ≤100 Hz spiking rate (Ronzitti et al., 2017a), whereas ReaChR, with a ~50 times slower $\tau_{off}$, enabled a light-evoked firing rate limited to ~35 Hz (~15 Hz for pyramidal cells) (Chaigneau et al., 2016). Photostimulation of interneurons expressing CoChR, which has an intermediate value of $\tau_{off}$ (~30 ms), could still generate light-evoked trains at 100 Hz, but temporal precision and fidelity were progressively lost across the train.

Interestingly, the efficient current integration that is achievable with parallel holographic illumination enables reliable AP generation with millisecond temporal resolution and submillisecond precision. This system uses, at depths of ~100 μm, excitation densities <1 mW/μm$^2$ or 100 μW/μm$^2$ with a conventional mode-locked high-repetition-rate (80 MHz) laser oscillator or a low-repetition-rate (500 kHz) amplifier, respectively (Chaigneau et al., 2016; Ronzitti et al., 2017a; Shemesh et al., 2017).

## Penetration depth

As previously described, TF coupled with CGH or GPC enables micrometer-range axial confinement. A further advantage of this approach is that it

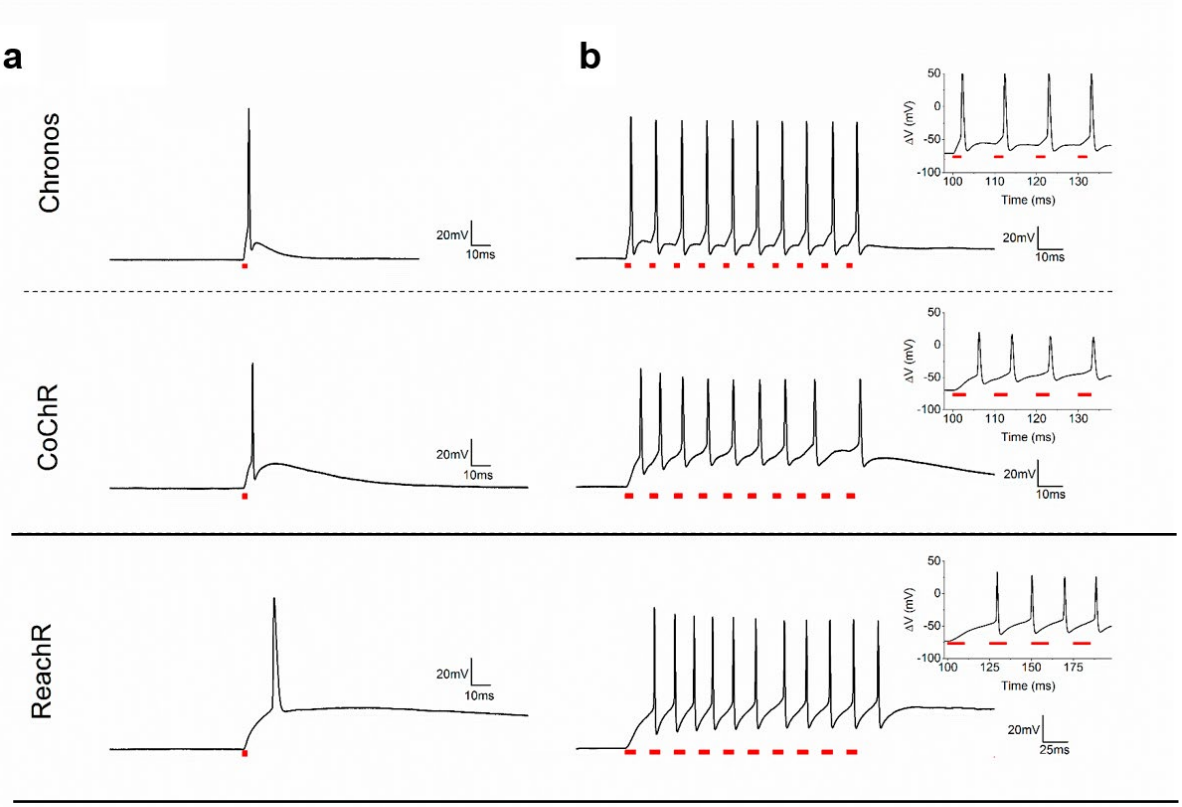


**Figure 8.** Temporal resolution and spiking rate. ***a***, Light-elicited single spike by 2P holographic illumination (spot diameter, 15 μm; $\lambda$ = 1030 nm). Short light illumination pulses ($t$ = 2 ms) of Chronos ($p$ = 0.09 mW/μm$^2$), CoChR ($p$ = 0.1 mW/μm$^2$) (V. Zampini, unpublished observations), and ReaChR ($p$ = 0.07 mW/μm$^2$) expressing interneurons from layer 2/3 of the mouse visual cortex. ***b***, Light-driven firing fidelity in opsin-positive interneurons achieved by illuminating with a train of 10 light pulses, Chronos ($t$ = 2 ms; $f$ = 100 Hz; $p$ = 0.12 mW/μm$^2$), CoChR ($t$ = 3 ms; $f$ = 100 Hz; $p$ = 0.1 mW/μm$^2$), and ReaChR ($t$ = 10 ms; $f$ = 40 Hz; $p$ = 0.04 mW/μm$^2$). Insets, The first four pulses enlarged. Chronos and CoChR data are adapted from Ronzitti et al. (2017a), and ReaChR data are adapted from Chaigneau et al. (2016). Calibration: ***a***, 20 mV, 100 ms; ***b***, Top and middle, 20 mV, 100 ms; bottom, 20 mV, 100 ms. Reprinted with permission from Papagiakoumou et al (2018), Fig. 9. Copyright 2018, Springer Science+Business Media LLC.

enables robust light propagation through scattering media (Bègue et al., 2013; Papagiakoumou et al., 2013; Hernandez et al., 2016). Scattering deviates the original photon trajectory, thus deforming the excitation spot shape at the focal plane. For light illumination with diffraction-limited spots, this translates mainly into occurrence of aberrations and loss of axial and lateral resolution. Moreover, scattered photons do not contribute to signal arising from the focal volume, which translates into loss of light intensity (Booth et al., 2012).

For large illumination areas, the presence of scattering also generates speckles in the excitation spot due to the random interference between ballistic and scattered photons (Fig. 9*a*). A few years ago, we demonstrated that TF, combined with both CGH (Bègue et al., 2013) and GPC (Papagiakoumou et al., 2013), reduces this effect because scattered photons have a lower probability of interfering with ballistic photons (Fig. 9*a*). Light propagation of patterns generated using CGH (Bègue et al., 2013) and GPC (Papagiakoumou et al., 2013) through cortical brain slices or zebrafish larvae (Hernandez et al., 2016) have revealed robust conservation of lateral shape and axial resolution up to depths twice the scattering length (Fig. 9*b*), thereby enabling in-depth optogenetic stimulation (Papagiakoumou et al., 2013).

## Multicell volumetric photoactivation

Parallel approaches present the great advantage of minimizing illumination time compared with their scanning counterparts. For example, the total illumination time for scanning activation, $T_{1.scan}$, roughly equals the illumination time per spot ($t_{dwell}$) multiplied by the number of scanned positions and the number of targets. In contrast, the total illumination time for parallel approaches, $T_{1.paral}$, is given only by $t_{dwell}$. As a consequence, for volumetric multicell targeting, $T_{1.scan}$ can largely exceed the value of $T_{1.paral}$, and 3D parallel illumination remains the only option for achieving multitarget activation with millisecond temporal resolution (Ronzitti et al., 2017b).

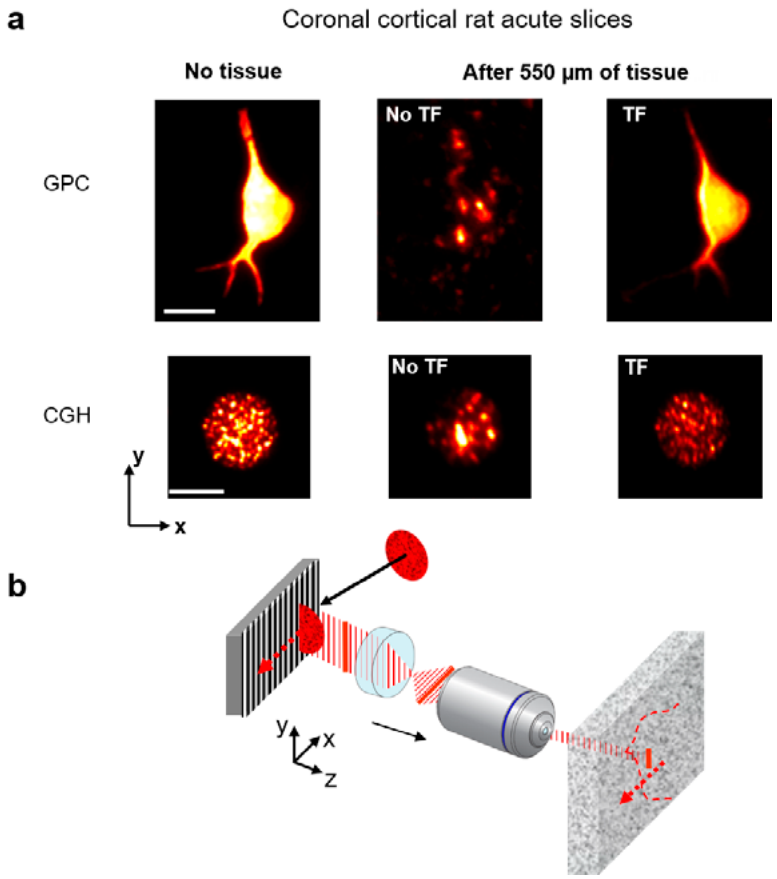


**Figure 9.** TF and penetration depth. ***a***, 2P fluorescence *x–y* cross-sections of GPC-generated excitation patterns mimicking a neuron with small processes (top left) and a 15-µm-diameter CGH spot (bottom left) after propagation through 550 µm of acute coronal cortical rat brain slices without (middle panel) and with (right panel) TF ($\lambda$ = 950 nm). Nontemporally focused beams are transformed into speckled patterns after traveling through the tissue. ***b***, The propagation of a large beam (a holographic spot) diffracted by the grating produces an ultrafast line scanning of the sample. Scattering events off the scanning line at a single moment in time cannot interfere with the ballistic photons in the line. Modified with permission from Papagiakoumou et al., (2018), Figs. 10*a*, 11. Copyright 2018, Springer Science+Business Media LLC.

As originally demonstrated for multitrap optical tweezers (Curtis et al., 2002), CGH can generate multiple 3D foci using algorithms for "prisms and lenses" (Leach et al., 2006). Similar algorithms, combined with visible or infrared light, have been successively used for 3D neuronal stimulation with 1P or 2P uncaging (Nikolenko et al., 2008; Daria et al., 2009; Anselmi et al., 2011; Yang et al., 2011). However, optogenetic activation requires illumination of membrane areas greater than the micrometric size of spots typically adopted for uncaging. Thus, a possible solution (originally proposed by Packer et al., 2012) consists of generating in parallel multiple diffraction-limited spots via CGH at the positions of the targeted cells and simultaneously scanning the spots over the cell membranes using a galvanometric mirror–based system. Even so, the need for scanning the spots over the cell body limited achievable temporal resolution (illumination time for AP generation, ≥11 ms; latency, ≥20 ms; jitter, ≥6 ms) (Packer et al., 2012, 2014). Lately, high-peak-power–amplified excitation laser sources have been employed to reduce both latency (<10 ms) and jitter (~1 ms) using illumination durations of 10 ms and ~4.5 mW average illumination power per cell. Shorter illumination durations (e.g., 1 ms) also could be used to excite neurons; however, these require two to five times more power per cell (~10–20 mW) (Yang et al., 2018). Because efficient current integration under scanning photoactivation requires slow opsins, this approach limits the maximum achievable spiking rate. Moreover, the need for using focused light at saturation power to compensate for the small spot surface generates significant out-of-focus excitation (Rickgauer and Tank, 2009).

Alternatively, multitarget stimulation can be achieved using scanless 3D generation of extended patterns with a 3D extension of the Gerchberg–Saxton (Gerchberg and Saxton, 1972) algorithm in combination with low-NA objectives (Piestun et al., 1996; Haist et al., 1997). More recently 3D CGH, after being adapted to high-NA objectives and incorporated into intensity compensation protocols (Hernandez et al., 2016), was used to generate shaped patterns with uniform light distribution

NOTES

within an excitation field of 240 × 240 × 260 μm³. This approach made it possible to drive tail bending by selective photoactivation of a specific ensemble of premotor neurons in the larval zebrafish brain (dal Maschio et al., 2017). Similarly to 2D CGH, however, illumination of spatially closed targets quickly deteriorates axial resolution (Papagiakoumou et al., 2018). On the other hand, using 3D illumination with TF is a challenge because the axially shifted holographic planes cannot be simultaneously imaged on the TF grating (Chen et al., 2018).

As a solution, we demonstrated an optical scheme using two SLMs (Fig. 10*a*) to independently control the lateral shape and position of multiple patterns (SLM1) and their axial position (SLM2)

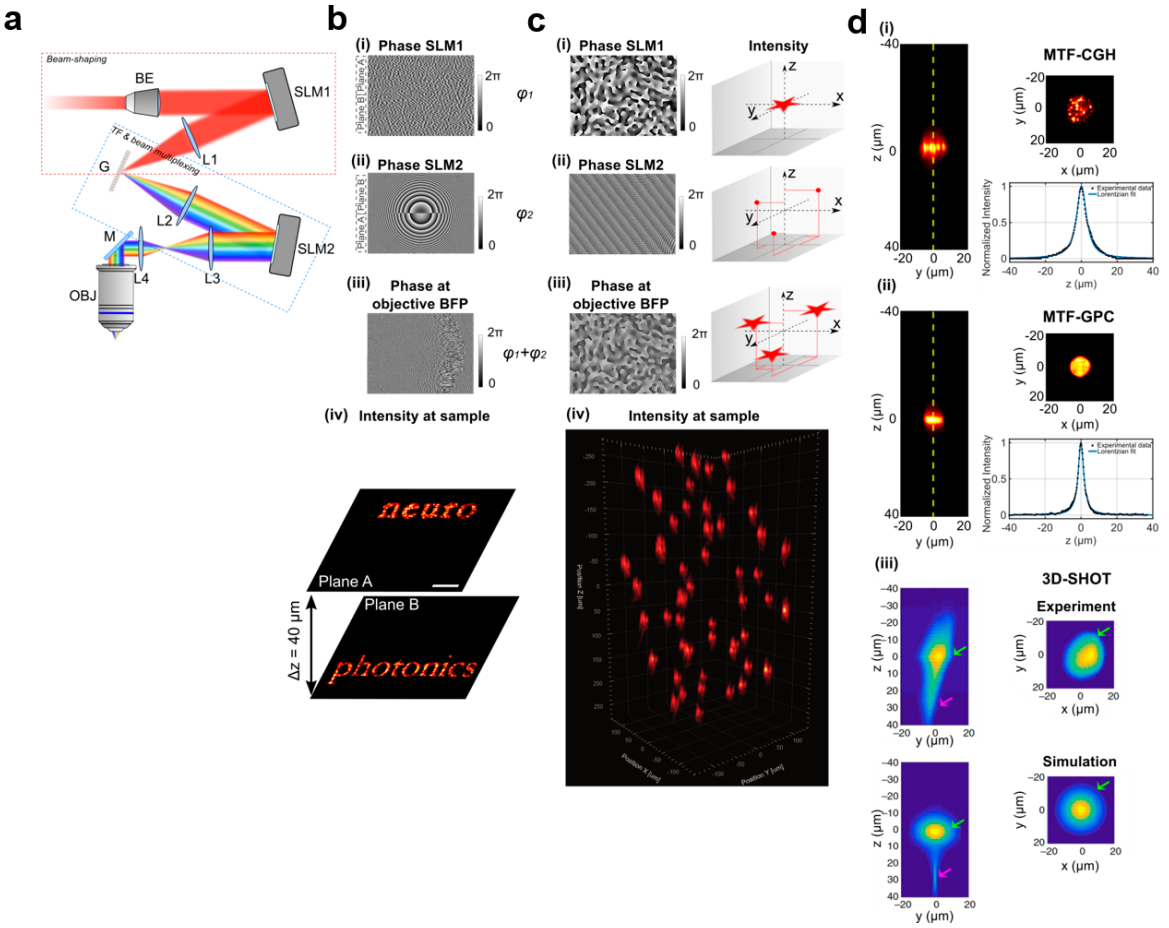


**Figure 10.** Multiplane temporally focused pattern projection. ***a***, Experimental scheme for multiplane temporally focused patterns. The system comprises a first beam-shaping part, which, according to experimental needs, can generate a Gaussian, a holographic, or a GPC beam. Here, a CGH beam is shown (red dashed box). The second part performs TF through the diffraction grating G and lenses L2 and L3, and spatial beam multiplexing through SLM2 and L3 via CGH (blue dashed box). L4 and OBJ (the objective) rescale the 3D pattern configuration at the sample volume. Modified with permission from Accanto et al. (2017), Fig. 1*a*. Copyright 2017, The Authors. ***b–c***, Examples of different ways of addressing the two SLMs in the scheme presented in a for MTF-CGH: ***b***(*i*), SLM1 is vertically tiled in different areas, each addressed with independent phase profiles, which in the present paradigm project the words "neuro" and "photonics" in two different planes A and B. ***b***(*ii*), SLM2 is addressed with two Fresnel lens phase profiles to axially displace each holographic pattern generated by SLM1 on separate planes, in this case at +20 μm (plane A) and –20 μm (plane B). ***b***(*iii*), Phase profile resulting at the objective back focal plane (BFP) for a single spectral frequency. ***b***(*iv*), Intensity distribution at the focal plane of the objective. Scale bar, 20 μm. Modified with permission from Hernandez et al. (2016), Fig. 3*b*. Copyright 2016, The Optical Society. ***c***, Multiplexed temporally focused CGH. ***c***(*i*), SLM1 is addressed with a phase hologram encoding the desired excitation pattern, e.g., a star. ***c***(*ii*), SLM2 is addressed with a phase profile encoding a 3D diffraction-limited spot distribution. ***c***(*iii*), Resulting phase profile at the objective BFP creating multiple replicas of the pattern generated by the first SLM. ***c***(*iv*), Application of the method for projecting 50 15-μm-diameter circular, temporally focused spots in a volume of 300 × 300 × 500 μm³. Adapted with permission from Accanto et al. (2017), Fig. 1*b*. Copyright 2017, The Authors. ***d***, Illustration of different beam-shaping methods that could be used in MTF-LS configurations. The *x*–*y*, *y*–*z* cross-sections are shown for (*i*) MTF-CGH, (*ii*) MTF-GPC, and (*iii*) large Gaussian beams (3D-SHOT: 3D scanless holographic optogenetics with temporal focusing). In ***d***(*iii*), both experimental data and simulation are shown. Green arrows indicate the primary focus of the method, and magenta arrows indicate the secondary focus. Excerpted with permission from Pégard et al. (2017), Figs. 2*c*, *d*. Copyright 2017, The Authors. For MTF-CGH and MTF-GPC, the axial intensity profiles along the yellow dashed lines of the *y*–*z* cross-sections are reported.

NOTES

(Hernandez et al., 2016). We did so by addressing the SLMs in vertical tiles equaling the number of planes to be illuminated (Fig. 10*b*). For the first time, this strategy enabled the generation of temporally focused patterns at axially distinct planes whose axial selectivity was demonstrated by 3D photoconversion of multiple targets in the zebrafish larva spinal cord and brain (Hernandez et al., 2016). The main drawback of vertically tiling the SLMs is the need for using holograms with a reduced pixel number, $N$, in the vertical direction (orthogonal to the dispersion direction) (Hernandez et al., 2016), so for $N \leq 100$, the lateral resolution consequently deteriorates. This deterioration limits the maximum number of achievable planes to $\approx N_{SLM}/100$, with $N_{SLM}$ being the total number of pixels in the SLM vertical direction (6–12 planes for the most commonly used LC-on-silicon [LCOS] devices). This limitation can be overcome by using the second SLM for both lateral and axial beam multiplexing, as illustrated in Figure 10*c* (Accanto et al., 2017). This scheme enables multiplexed TF light shaping (MTF-LS), which has several advantages. First, because each spot is the exact replica of what the first SLM generates at the TF grating, the spot quality in the 3D volume is independent on the number of generated planes and axial position. Second, MTF-LS is compatible with different light-shaping approaches, including dynamic CGH (Accanto et al., 2017), GPC (Go et al., 2011; Accanto et al., 2017; Bañas and Glückstad, 2017), CGH with a fixed phase mask (Accanto et al., 2017), and low-NA Gaussian beams (Pégard et al., 2017; Sun et al., 2018).

Dynamic CGH has maximal flexibility and enables fast lateral shaping. Replacing the bulky SLM with a smaller static phase mask makes the system less flexible but leads to a simpler, more compact optical design. GPC, on the other hand, permits the generation of illumination patterns with superior axial resolution and higher uniformity, that is, speckle-free (Fig. 10*d*). This feature is particularly advantageous for applications requiring spot sizes to be comparable with the speckle size or for multisite functional imaging. For conventional GPC, the conditions for achieving maximum interferometric contrast impose some restrictions on the optimal spot size and FOE (Papagiakoumou et al., 2010); moreover, intensity light shaping is limited to a single plane (conjugated to the SLM plane). However, when GPC is implemented in a MTF-GPC scheme, these limitations can all be overcome: the GPC setup can be designed to generate a shape with optimal diffraction efficiency, and multiplexed laterally and axially by the second SLM, thus enabling 3D spot generation within the same FOE reached in CGH (Go et al., 2011; Accanto et al., 2017; Bañas and Glückstad, 2017).

The MTF-LS approach can be further simplified by replacing the first light-shaping module with an expanded Gaussian beam, as independently demonstrated by two groups, led by M. Booth (Sun et al., 2018) and H. Adesnik (Pégard et al., 2017). However, as for MTF-GPC, the use of low-NA Gaussian beams limits the beam size on the SLM in the unchirped direction to a few millimeters. This limitation restricts the maximum power that can be used, the number of pixels illuminated, and therefore, the maximum number of achievable targets. Introducing a curvature on the incident Gaussian beam, as proposed by Pégard and colleagues (2017), enabled investigators to cover the entire SLM and generate hundreds of spots in a $400 \times 400$ x 400 $\mu m^3$ excitation volume. However, this solution inevitably separates the spatial from the temporal focal plane and leaves a secondary spatial focus, which deteriorates the axial resolution (Fig. 10*d*). Placing a rotating diffuser on an intermediate image plane can decrease the contribution of the secondary spatial focus (Mardinly et al., 2018), but the use of a low-NA Gaussian beam is limited to the generation of a nonreconfigurable, single-size spot. Additionally, the smooth edges of a Gaussian beam, unlike the sharp edges of GPC and CGH spots, can deteriorate the lateral resolution when using excitation power close to saturation.

Designing complex, multitarget experiments requires taking into account possible sources of photo damage to set the maximum number of achievable targets. Sources include thermal damage related to the linear absorption of light and nonlinear photochemical and ablation damage (Boulnois, 1986; Koester et al., 1999; Hopt and Neher, 2001). Scanning approaches require higher intensity but lower average power, so they will be limited mostly by nonlinear damage. Parallel approaches, in contrast, use very low intensity but an average power that is two to three times higher than scanning methods (Picot et al., 2018; Yang et al., 2018). Therefore, the latter will be limited mostly by thermal damage.

In a recent work, we developed a theoretical model of 3D light propagation and heat diffusion. This model is capable of simulating with micrometric resolution and millisecond precision the laser-induced temperature rise produced by 2P optogenetic activation (Picot et al., 2018). Different illumination approaches (e.g., scanning, parallel) can be

reproduced, and heating can be investigated as a function of multiple parameters (e.g., laser power, number and distribution of spots, frequency of stimulation pulses) (Picot et al., 2018). This model's predictions can provide useful information for designing multitarget 2P optogenetics experiments with minimal sample heating.

## Outlook

CGH, combined with 2P excitation, enables in-depth optical stimulation with millisecond temporal resolution and submillisecond temporal precision. Combining CGH with TF enables the generation of excitation volumes with micrometer axial resolution and robust propagation through scattering media. For neuronal activation, efficient current integration is achievable using parallel holographic illumination combined with laser amplifiers at a low-repetition rate (500 kHz). This enables reliable AP generation with millisecond temporal resolution and submillisecond-precision excitation densities (<100 $\mu W/\mu m^2$). These findings, together with the high average power available in commercially available laser systems (>10 W at laser output), indicate that laser power is not the limiting factor for the maximum achievable number of targets using CGH. More likely, target number will be limited by other factors, such as sample heating (discussed above) or deterioration of the photostimulation spatial resolution. Indeed, for multiple-cell stimulation, photostimulating neurites crossing the illumination volume affects cellular resolution, thereby limiting the number of targets that can be stimulated with single-cell precision. Recent progress in engineering somatic opsins (Baker et al., 2016; Mardinly et al., 2018; Shemesh et al., 2017) should enable us to transcend these limitations in the near future.

## Acknowledgments

This chapter was adapted with permission from two previously published articles: Papagiakoumou et al. (2018) Two-photon optogenetics by computer-generated holography. In: Optogenetics: a roadmap, Vol 133, Neuromethods series (Stroh A, ed), pp 175–197 (New York: Humana Press). Copyright 2018, Springer Science+Business Media LLC; and Chen et al. (2018) Towards circuit optogenetics. Curr Opin Neurobiol 50:179–189. Copyright 2018, Elsevier.

## References

Accanto N, Tanese D, Ronzitti E, Molinier C, Newman ZL, Wyart C, Isacoff E, Papagiakoumou E, Emiliani V (2017) Multiplexed temporally focused light shaping for high-resolution multi-cell targeting. bioRxiv doi: 10.1101/216135.

Adamantidis AR, Zhang F, Aravanis AM, Deisseroth K, de Lecea L (2007) Neural substrates of awakening probed with optogenetic control of hypocretin neurons. Nature 450:420–424.

Adesnik H, Bruns W, Taniguchi H, Huang ZJ, Scanziani M (2012) A neural circuit for spatial summation in visual cortex. Nature 490:226–231.

Andrasfalvy BK, Zemelman BV, Tang J, Vaziri A (2010) Two-photon single-cell optogenetic control of neuronal activity by sculpted light. Proc Natl Acad Sci USA 107:11981–11986.

Anikeeva P, Andalman AS, Witten I, Warden M, Goshen I, Grosenick L, Gunaydin LA, Frank LM, Deisseroth K (2012) Optetrode: a multichannel readout for optogenetic control in freely moving mice. Nat Neurosci 15:163–170.

Anselmi F, Ventalon C, Bègue A, Ogden D, Emiliani V (2011) Three-dimensional imaging and photostimulation by remote-focusing and holographic light patterning. Proc Natl Acad Sci USA 108:19504–19509.

Aravanis AM, Wang LP, Zhang F, Meltzer LA, Mogri MZ, Schneider MB, Deisseroth K (2007) An optical neural interface: *in vivo* control of rodent motor cortex with integrated fiberoptic and optogenetic technology. J Neural Eng 4:S143–S156.

Atallah BV, Bruns W, Carandini M, Scanziani M (2012) Parvalbumin-expressing interneurons linearly transform cortical responses to visual stimuli. Neuron 73:159–170.

Baker CA, Elyada YM, Parra A, Bolton MM (2016) Cellular resolution circuit mapping in mouse brain with temporal-focused excitation of soma-targeted channelrhodopsin. eLife 5:e14193.

Bañas A, Glückstad J (2017) Holo-GPC: Holographic Generalized Phase Contrast. Opt Commun 392:190–195.

NOTES

NOTES

Bègue A, Papagiakoumou E, Leshem B, Conti R, Enke L, Oron D, Emiliani V (2013) Two-photon excitation in scattering media by spatiotemporally shaped beams and their application in optogenetic stimulation. Biomed Opt Express 4:2869–2879.

Booth MJ, Débarre D, Jesach A (2012) Adaptive optics for biomedical microscopy. Opt Phot News 23:22–29.

Boulnois JL (1986) Photophysical processes in recent medical laser developments: a review. Lasers Med Sci 1:47–66.

Bovetti S, Fellin T (2015) Optical dissection of brain circuits with patterned illumination through the phase modulation of light. J Neurosci Methods 241:66–77.

Boyden ES, Zhang F, Bamberg E, Nagel G, Deisseroth K (2005) Millisecond-timescale, genetically targeted optical control of neural activity. Nat Neurosci 8:1263–1268.

Chaigneau E, Ronzitti E, Gajowa MA, Soler-Llavina GJ, Tanese D, Brureau AY, Papagiakoumou E, Zeng H, Emiliani V (2016) Two-photon holographic stimulation of ReaChR. Front Cell Neurosci 10:234.

Chen I-W, Papagiakoumou E, Emiliani V (2018) Towards circuit optogenetics. Curr Opin Neurobiol 50:179–189.

Conti R, Assayag O, De Sars V, Guillon M, Emiliani V (2016) Computer generated holography with intensity-graded patterns. Front Cell Neurosci 10:236.

Curtis JE, Koss BA, Grier DG (2002) Dynamic holographic optical tweezers. Opt Commun 207:169–175.

dal Maschio M, Donovan JC, Helmbrecht TO, Baier H (2017) Linking neurons to network function and behavior by two-photon holographic optogenetics and volumetric imaging. Neuron 94:774–789.e5.

Daria VR, Stricker C, Bowman R, Redman S, Bachor HA (2009) Arbitrary multisite two-photon excitation in four dimensions. Appl Phys Lett 95:93701.

Denk W, Strickler JH, Webb WW (1990) Two-photon laser scanning fluorescence microscopy. Science 248:73–76.

Engström D, Bengtsson J, Eriksson E, Goksör M (2008) Improved beam steering accuracy of a single beam with a 1D phase-only spatial light modulator. Opt Express 16:18275–18287.

Feldbauer K, Zimmermann D, Pintschovius V, Spitz J, Bamann C, Bamberg E (2009) Channelrhodopsin-2 is a leaky proton pump. Proc Natl Acad Sci USA 106:12317–12322.

Gerchberg RW, Saxton WO (1972) A practical algorithm for the determination of the phase from image and diffraction pictures. Optik (Stuttg) 35:237–246.

Glückstad J (1996) Phase contrast image synthesis. Opt Commun 130:225–230.

Go MA, Ng P-F, Bachor H, Daria VR (2011) Optimal complex field holographic projection. Opt Lett 36:3073–3075.

Golan L, Shoham S (2009) Speckle elimination using shift-averaging in high-rate holographic projection. Opt Express 17:1330–1339.

Golan L, Reutsky I, Farah N, Shoham S (2009) Design and characteristics of holographic neural photo-stimulation systems. J Neural Eng 6:66004.

Gradinaru V, Thompson KR, Zhang F, Mogri M, Kay K, Schneider MB, Deisseroth K (2007) Targeting and readout strategies for fast optical neural control *in vitro* and *in vivo*. J Neurosci 27:14231–14238.

Guillon M, Forget BC, Foust AJ, De Sars V, Ritsch-Marte M, Emiliani V (2017) Vortex-free phase patterns for uniform patterning with computer-generated holography. Opt Express 25:12640–12652.

Haist T, Schönleber M, Tiziani HJ (1997) Computer-generated holograms from 3D-objects written on twisted-nematic liquid crystal displays. Opt Commun 140:299–308.

Hegemann P, Ehlenbeck S, Gradmann D (2005) Multiple photocycles of channelrhodopsin. Biophys J 89:3911–3918.

Hernandez O, Guillon M, Papagiakoumou E, Emiliani V (2014) Zero-order suppression for two-photon holographic excitation. Opt Lett 39:5953–5956.

Hernandez O, Papagiakoumou E, Tanese D, Fidelin K, Wyart C, Emiliani V (2016) Three-dimensional spatiotemporal focusing of holographic patterns. Nat Commun 7:11928.

Hernandez Cubero OR (2016). Advanced optical methods for fast and three-dimensional control of neural activity. Paris: Descartes University.

Hopt A, Neher E (2001) Highly nonlinear photodamage in two-photon fluorescence microscopy. Biophys J 80:2029–2036.

NOTES

Huber D, Petreanu L, Ghitani N, Ranade S, Hromádka T, Mainen Z, Svoboda K (2008) Sparse optical microstimulation in barrel cortex drives learned behaviour in freely moving mice. Nature 451:61–64.

Joshi A, Kalappa BI, Anderson CT, Tzounopoulos T (2016) Cell-specific cholinergic modulation of excitability of layer 5B principal neurons in mouse auditory cortex. J Neurosci 36:8487–8499.

Klapoetke NC, Murata Y, Kim SS, Pulver SR, Birdsey-Benson A, Cho YK, Morimoto TK, Chuong AS, Carpenter EJ, Tian Z, Wang J, Xie Y, Yan Z, Zhang Y, Chow BY, Surek B, Melkonian M, Jayaraman V, Constantine-Paton M, Wong GK, Boyden ES (2014) Independent optical excitation of distinct neural populations. Nat Methods 11:338–346.

Koester HJ, Baur D, Uhl R, Hell SW (1999) $Ca^{2+}$ fluorescence imaging with pico- and femtosecond two-photon excitation: signal and photodamage. Biophys J 77:2226–2236.

Koshelev A, Calafiore G, Piña-Hernandez C, Allen FI, Dhuey S, Sassolini S, Wong E, Lum P, Munechika K, Cabrini S (2016) High refractive index Fresnel lens on a fiber fabricated by nanoimprint lithography for immersion applications. Opt Lett 41:3423–3426.

Leach J, Wulff K, Sinclair G, Jordan P, Courtial J, Thomson L, Gibson G, Karunwi K, Cooper J, Laczik ZJ, Padgett M (2006) Interactive approach to optical tweezers control. Appl Opt 45:897–903.

Lee SH, Kwan AC, Zhang S, Phoumthipphavong V, Flannery JG, Masmanidis SC, Taniguchi H, Huang ZJ, Zhang F, Boyden ES, Deisseroth K, Dan Y (2012) Activation of specific interneurons improves V1 feature selectivity and visual perception. Nature 488:379–383.

Lin JY, Knutsen PM, Muller A, Kleinfeld D, Tsien RY (2013) ReaChR: a red-shifted variant of channelrhodopsin enables deep transcranial optogenetic excitation. Nat Neurosci 16:1499–1508.

Lutz C, Otis TS, DeSars V, Charpak S, DiGregorio DA, Emiliani V (2008) Holographic photolysis of caged neurotransmitters. Nat Methods 5:821–827.

Makinson CD, Tanaka BS, Sorokin JM, Wong JC, Christian CA, Goldin AL, Escayg A, Huguenard JR (2017) Regulation of thalamic and cortical network synchrony by Scn8a. Neuron 93:1165–1179.

Mardinly AR, Oldenburg IA, Pégard NC, Sridharan S, Lyall EH, Chesnov K, Brohawn SG, Waller L, Adesnik H (2018) Precise multimodal optical control of neural ensemble activity. Nat Neurosci 21:881–893.

Morgenstern NA, Bourg J, Petreanu L (2016) Multilaminar networks of cortical neurons integrate common inputs from sensory thalamus. Nat Neurosci 19:1034–1040.

Nagel G, Szellas T, Huhn W, Kateriya S, Adeishvili N, Berthold P, Ollig D, Hegemann P, Bamberg E (2003) Channelrhodopsin-2, a directly light-gated cation-selective membrane channel. Proc Natl Acad Sci USA 100:13940–13945.

Nagel G, Brauner M, Liewald JF, Adeishvili N, Bamberg E, Gottschalk A (2005) Light activation of channelrhodopsin-2 in excitable cells of *Caenorhabditis elegans* triggers rapid behavioral responses. Curr Biol 15:2279–2284.

Nikolenko V, Watson BO, Araya R, Woodruff A, Peterka DS, Yuste R (2008) SLM microscopy: scanless two-photon imaging and photostimulation with spatial light modulators. Front Neural Circuits 2:5.

Nikolic K, Degenaar P, Toumazou C (2006) Modeling and engineering aspects of ChannelRhodopsin2 system for neural photostimulation. Conf Proc IEEE Eng Med Biol Soc 1626–1629.

Nikolic K, Grossman N, Grubb MS, Burrone J, Toumazou C, Degenaar P (2009) Photocycles of channelrhodopsin-2. Photochem Photobiol 85:400–411.

Oron D, Tal E, Silberberg Y (2005) Scanningless depth-resolved microscopy. Opt Express 13:1468–1476.

Oron D, Papagiakoumou E, Anselmi F, Emiliani V (2012) Two-photon optogenetics. In: Optogenetics: tools for controlling and monitoring neuronal activity, Vol 196, Progress in brain research, Chap 7, Ed 1 (Knöpfel T, Boyden E, eds), pp 119–144. New York: Elsevier BV.

Packer AM, Peterka DS, Hirtz JJ, Prakash R, Deisseroth K, Yuste R (2012) Two-photon optogenetics of dendritic spines and neural circuits. Nat Methods 9:1202–1205.

Packer AM, Roska B, Häusser M (2013) Targeting neurons and photons for optogenetics. Nat Neurosci 16:805–815.

NOTES

Packer AM, Russell LE, Dalgleish HWP, Häusser M (2014) Simultaneous all-optical manipulation and recording of neural circuit activity with cellular resolution *in vivo*. Nat Methods 12:140–146.

Papagiakoumou E. Optical developments for optogenetics (2013) Biol Cell 105:443–464.

Papagiakoumou E, de Sars V, Oron D, Emiliani V (2008) Patterned two-photon illumination by spatiotemporal shaping of ultrashort pulses. Opt Express 16:22039–22047.

Papagiakoumou E, Anselmi F, Bègue A, de Sars V, Glückstad J, Isacoff EY, Emiliani V (2010) Scanless two-photon excitation of channelrhodopsin-2. Nat Methods 7:848–854.

Papagiakoumou E, Bègue A, Leshem B, Schwartz O, Stell BM, Bradley J, Oron D, Emiliani V (2013) Functional patterned multiphoton excitation deep inside scattering tissue. Nat Photonics 7:274–278.

Papagiakoumou E, Ronzitti E, Chen I-W, Gajowa M, Picot A, Emiliani V (2018) Two-photon optogenetics by computer-generated holography. In: Optogenetics: a roadmap, Neuromethods series, Vol 133 (Stroh A, ed), pp 175–197. New York: Humana Press.

Pégard NM, Mardinly AR, Oldenburg IA, Sridharan S, Waller L, Adesnik H (2017) 3D scanless holographic optogenetics with temporal focusing (3D-SHOT). Nat Commun 8:1228.

Petreanu L, Huber D, Sobczyk A, Svoboda K (2007) Channelrhodopsin-2-assisted circuit mapping of long-range callosal projections. Nat Neurosci 10:663–668.

Petreanu L, Mao T, Sternson SM, Svoboda K (2009) The subcellular organization of neocortical excitatory connections. Nature 457:1142–1145.

Picot A, Dominguez S, Liu C, Chen IW, Tanese D, Ronzitti E, Berto P, Papagiakoumou E, Oron D, Tessier G, Forget BC, Emiliani V (2018) Temperature rise under two-photon optogenetic brain stimulation. Cell Rep 24:1243–1253.

Piestun R, Spektor B, Shamir J (1996) Wave fields in three dimensions: Analysis and synthesis. J Opt Soc Am A 13:1837–1848.

Polin M, Ladavac K, Lee S-H, Roichman Y, Grier DG (2005) Optimized holographic optical traps. Opt Express 13:5831–5845.

Prakash R , Yizhar O, Grewe B, Ramakrishnan C, Wang N, Goshen I, Packer AM, Peterka DS, Yuste R, Schnitzer MJ, Deisseroth K (2012) Two-photon optogenetic toolbox for fast inhibition, excitation and bistable modulation. Nat Methods 9:1171–1179.

Rickgauer JP, Tank DW (2009) Two-photon excitation of channelrhodopsin-2 at saturation. Proc Natl Acad Sci USA 106:15025–15030.

Rickgauer JP, Deisseroth K, Tank DW (2014) Simultaneous cellular-resolution optical perturbation and imaging of place cell firing fields. Nat Neurosci 17:1816–1824.

Ronzitti E, Guillon M, de Sars V, Emiliani V (2012) LCoS nematic SLM characterization and modeling for diffraction efficiency optimization, zero and ghost orders suppression. Opt Express 20:17843–17855.

Ronzitti E, Conti R, Zampini V, Tanese D, Foust AJ, Klapoetke N, Boyden ES, Papagiakoumou E, Emiliani V (2017a) Sub-millisecond optogenetic control of neuronal firing with two-photon holographic photoactivation of Chronos. J Neurosci 37:10679–10689.

Ronzitti E, Ventalon C, Canepari M, Forget BC, Papagiakoumou E, Emiliani V (2017b) Recent advances in patterned photostimulation for optogenetics. J Opt 19:113001.

Schmitz CHJ, Spatz JP, Curtis JE (2005) High-precision steering of multiple holographic optical traps. Opt Express 13:8678–8685.

Shemesh OA, Tanese D, Zampini V, Linghu C, Piatkevich K, Ronzitti E, Papagiakoumou E, Boyden ES, Emiliani V (2017) Temporally precise single-cell-resolution optogenetics. Nat Neurosci 20:1796–1806.

Sun B, Salter PS, Roider C, Jesacher A, Strauss J, Heberle J, Schmidt M, Booth MJ (2018) Four-dimensional light shaping: manipulating ultrafast spatio-temporal foci in space and time. Light Sci Appl. 7:17117.

Szabo V, Ventalon C, De Sars V, Bradley J, Emiliani V (2014) Spatially selective holographic photoactivation and functional fluorescence imaging in freely behaving mice with a fiberscope. Neuron 84:1157–1169.

NOTES

Tovote P, Esposito MS, Botta P, Chaudun F, Fadok JP, Markovic M, Wolff SB, Ramakrishnan C, Fenno L, Deisseroth K, Herry C, Arber S, Lüthi A (2016) Midbrain circuits for defensive behaviour. Nature 534:206–212.

Vaziri A, Emiliani V (2012) Reshaping the optical dimension in optogenetics. Curr Opin Neurobiol 22:128–137.

Weible AP, Piscopo DM, Rothbart MK, Posner MI, Niell CM (2017) Rhythmic brain stimulation reduces anxiety-related behavior in a mouse model based on meditation training. Proc Natl Acad Sci USA 114:2532–2537.

Williams JC, Xu J, Lu Z, Klimas A, Chen X, Ambrosi CM, Cohen IS, Entcheva E (2013) Computational optogenetics: empirically-derived voltage- and light-sensitive channelrhodopsin-2 model. PLoS Comput. Biol. 9:e1003220.

Yang S, Papagiakoumou E, Guillon M, de Sars V, Tang CM, Emiliani V (2011) Three-dimensional holographic photostimulation of the dendritic arbor. J Neural Eng 8:046002.

Yang W, Carrillo-Reid L, Bando Y, Peterka DS, Yuste R (2018) Simultaneous two-photon imaging and two-photon optogenetics of cortical circuits in three dimensions. eLife 7:e32671.

Zahid M, Vélez-Fort M, Papagiakoumou E, Ventalon C, Angulo MC, Emiliani V (2010) Holographic photolysis for multiple cell stimulation in mouse hippocampal slices. PLoS One 5:e9431.

Zhang F, Wang LP, Brauner M, Liewald JF, Kay K, Watzke N, Wood PG, Bamberg E, Nagel G, Gottschalk A, Deisseroth K (2007) Multimodal fast optical interrogation of neural circuitry. Nature 446:633–639.

Zhu G, van Howe J, Durst M, Zipfel W, Xu C (2005) Simultaneous spatial and temporal focusing of femtosecond pulses. Opt Express 13:2153–2159.

# High-Speed Recording of Neural Spikes in Awake Mice and Flies with a Fluorescent Voltage Sensor

Yiyang Gong, PhD,[1,2,3] Cheng Huang, PhD,[1] Jin Zhong Li, DVM,[1,2]
Benjamin F. Grewe, PhD,[1,2] Yanping Zhang, MD,[1,2,4]
Stephan Eismann, MS,[1,2] and Mark J. Schnitzer, PhD[1,2,4]

[1]James H. Clark Center
Stanford University
Stanford, California

[2]CNC Program
Stanford University
Stanford, California

[3]Department of Biomedical Engineering
Duke University
Durham, North Carolina

[4]Howard Hughes Medical Institute
Stanford University
Stanford, California

NOTES

## Introduction

Genetically encoded voltage indicators (GEVIs) are a promising technology for fluorescence readout of millisecond-scale neuronal dynamics. Previous GEVIs had insufficient signaling speed and dynamic range to resolve action potentials in live animals. We coupled fast voltage-sensing domains from a rhodopsin protein to bright fluorophores via resonance energy transfer. The resulting GEVIs are sufficiently bright and fast to report neuronal action potentials and membrane voltage dynamics in awake mice and flies, resolving fast spike trains with 0.2 ms timing precision at spike-detection error rates orders of magnitude better than previous GEVIs. *In vivo* imaging revealed sensory-evoked responses, including somatic spiking, dendritic dynamics, and intracellular voltage propagation. These results empower *in vivo* optical studies of neuronal electrophysiology and coding and motivate further advancements in high-speed microscopy.

To dissect the mechanisms of high-speed neuronal information processing in the live brain, neuroscientists need to track cellular and subcellular electrophysiological activity with millisecond-scale resolution in identified neuron types. Genetically encoded fluorescent $Ca^{2+}$ indicators report isolated, individual action potentials from many cell types in live animals (Chen et al., 2013; Inoue et al., 2015). However, $Ca^{2+}$ indicators' slow kinetics (~50–1000 ms) precludes high-fidelity studies of fast-spiking cell types, determinations of spike waveforms, resolution of individual spikes in fast spike trains, and precise estimates of spike timing. Moreover, the magnitude of $Ca^{2+}$ influx in response to an action potential varies across cell types and even within individual cells (Chen et al., 2013; Inoue et al., 2015). *In vivo* $Ca^{2+}$ imaging also poorly tracks subthreshold or dendritic voltage dynamics, due to insensitivity to hyperpolarizations and confounds from synaptic $Ca^{2+}$ influx. Organic voltage-sensitive dyes typically have much faster kinetics than $Ca^{2+}$ indicators but are generally highly phototoxic, allow neither genetically targeted delivery nor long-term imaging studies of single cells, and have been incapable of reporting single spikes in the live mammalian brain (Peterka et al., 2011).

GEVIs combine genetic targeting and optical readout of transmembrane voltage (Peterka et al., 2011; Knopfel, 2012), and in principle can sense spikes and subthreshold dynamics. Nevertheless, to date, GEVIs have lacked the capabilities to detect individual action potentials and fast spike trains in live animals (Peterka et al., 2011; Knopfel, 2012). Past efforts fused fluorescent proteins to voltage-sensitive domains (VSDs) from voltage-sensitive phosphatases (Lundby et al., 2008; Tsutsui et al., 2008; Jin et al., 2012; St-Pierre et al., 2014; Hamel et al., 2015) or used Archaerhodopsin (Arch), which is both a fast VSD and a dim fluorophore (Hochbaum et al., 2014). Although Arch variants work well in cultured neurons, the intense illumination required (1–10 $W \cdot mm^{-2}$) plus the consequent heating, autofluorescence, and photo damage have precluded imaging studies in intact tissue over wide fields of view (Hochbaum et al., 2014).

Here we present fast GEVIs (<1 ms response) that fuse the *Acetabularia acetabulum* rhodopsin (Ace) (Tsunoda et al., 2006) and mNeonGreen (Shaner et al., 2013) fluorescent protein to enable voltage-sensitive fluorescence resonance energy transfer (FRET) (Fig. 1*A*; Table S1). We previously introduced this "FRET-opsin" configuration (Gong et al., 2014; Zou et al., 2014), which combines the fast kinetics of a rhodopsin VSD with a bright fluorophore and provides high-fidelity membrane potential and spike train readouts at illumination levels ~50–100 times lower than used with Arch indicators. A FRET-opsin indicator based on *Leptosphaeria maculans* (Mac) rhodopsin and yellow fluorescent mCitrine reported fast neural spiking in brain slices and Purkinje neurons' dendritic activation in live mice (Gong et al., 2014). These results had suggested that optical recordings of action potentials and dendritic voltage dynamics in live animals might be attainable. Ace-mNeon indicators now enable high-fidelity imaging of individual spikes and fast spike trains in live mice and flies, due to their faster kinetics and superior brightness compared with all previous GEVIs. Ace is approximately sixfold faster than Mac, and mNeonGreen has a ~50% higher extinction coefficient than mCitrine and nearly threefold better photostability (Shaner et al., 2013). We created Ace mutants (Ace1Q and Ace2N) with an inactivated proton pump; these have blue-shifted absorption spectra compared with Mac and Arch (Tsunoda et al., 2006; Gong et al., 2014), yielding superior FRET acceptors when paired with green or yellow emitters (Figs. S1, S2). When used together with protein trafficking signals, the fusions provide high FRET efficiency and minimal protein aggregation in live neurons (Figs. 1*A*,*B*)—key attributes of a FRET indicator (Gong et al., 2014; Zou et al., 2014).

We measured responses of Ace1Q-mNeon and Ace2N-mNeon to voltage depolarization steps in cultured HEK293T cells. These sensors responded five- to sixfold faster than MacQ-mCitrine (Gong

NOTES

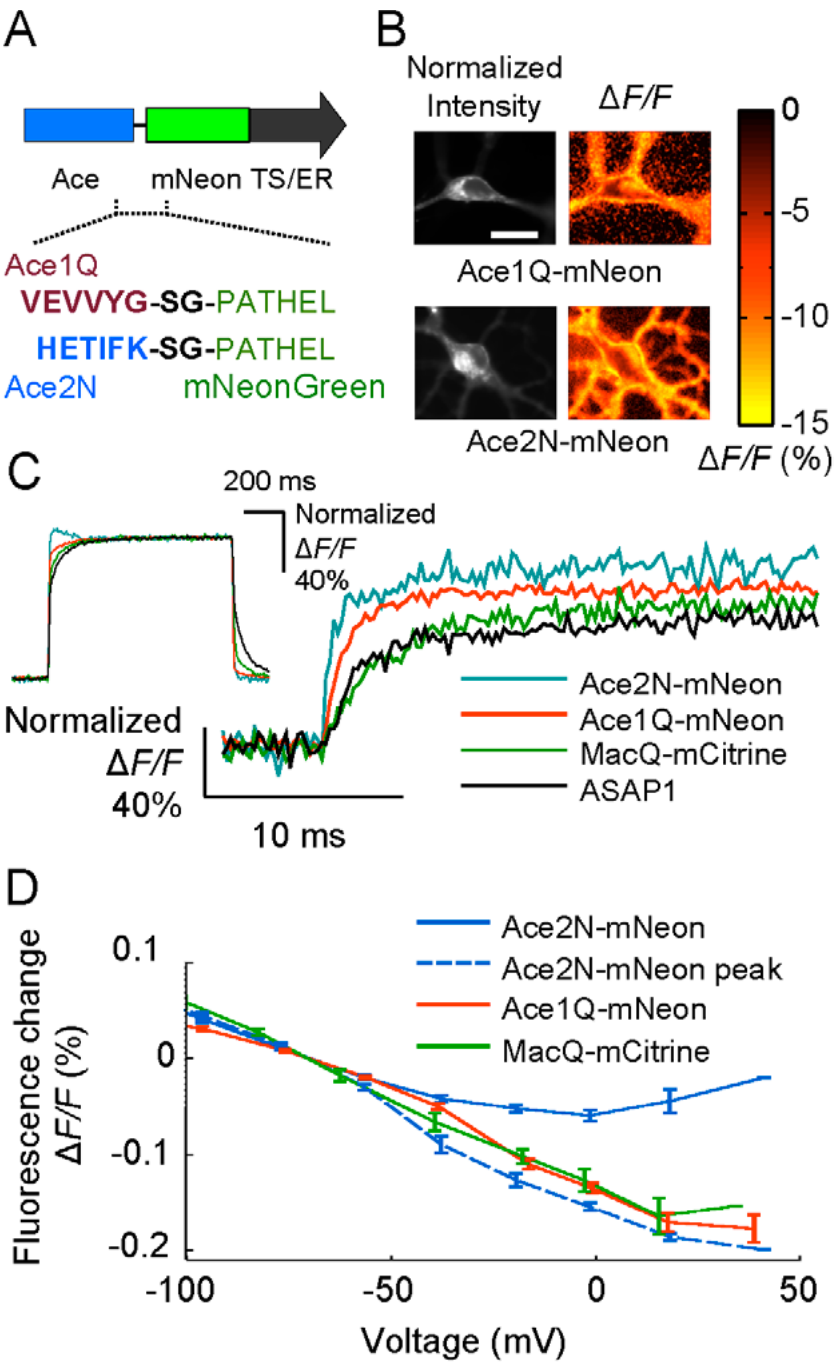


**Figure 1.** Ace FRET-opsin sensors report membrane voltage with ~1 ms response times. ***A***, Linker sequences bridging Ace1Q and Ace2N to mNeonGreen. Endoplasmic reticulum (ER) export sequence and Golgi export trafficking signal (TS) at the construct's C-terminus improve the sensor's membrane localization and hence the signaling dynamic range. ***B***, Fluorescence signals from neurons expressing Ace1Q-mNeon or Ace2N-mNeon. Left, Baseline fluorescence emissions from mNeonGreen. Right, Spatial maps of the fluorescence response (Δ*F*/*F*) to a voltage step of ~100 mV. Areas of fluorescence and voltage response were generally colocalized. Illumination intensity: 15 mW · $mm^{-2}$. Scale bar, 20 µm. ***C***, Step responses of the Ace sensors, ASAP1 and MacQ-mCitrine, to +100 mV command voltage steps, normalized to each sensor's maximum (or steady state) Δ*F*/*F* response to the command voltage. The initial rise of the Ace2N-mNeon sensor was more than sixfold faster than that of ASAP1 and MacQ-mCitrine (Table S2). Inset, The full step response of all sensors. Note that the trace for Ace2N-mNeon exhibits hysteresis ~40–200 ms after the voltage step, outside the interval shown in the main plot. Illumination intensity: 15–50 mW · $mm^{-2}$; image frame acquisition rate: 5 kHz. Inset traces were downsampled to 250 Hz. ***D***, Steady-state responses of FRET-opsin sensors as a function of membrane voltage in cultured neurons (*N* = 10 cells per trace). Since Ace2N-mNeon exhibited hysteric responses to voltage steps (Fig. S2), we also plot its peak initial responses. Illumination intensity: 15 mW · $mm^{-2}$; error bars: SEM. Reprinted with permission from Gong et al. (2015), Fig. 1. Copyright 2015, American Association for the Advancement of Science.

NOTES

et al., 2014) and the ASAP1 indicator (St-Pierre et al., 2014) (Fig. 1C; Table S2). At termination of a step depolarization, Ace2N-mNeon exhibited some hysteresis during its relaxation back to baseline fluorescence levels (Fig. S3). However, the steady-state response varied linearly with the transmembrane voltage within the physiological range of subthreshold potentials, and the initial peak response increased linearly between –100 mV and +30 mV (Fig. 1*D*). These relationships were similar to those of previous FRET-opsin sensors (Figs. 1*D*, S3), but the faster kinetics of the Ace indicators enabled superior spike-detection fidelity, even for rapid successions of spikes that would have blurred together with $Ca^{2+}$ imaging (Figs. 2*A*–*E*). During action potentials in cultured neurons, Ace2N-mNeon and Ace1Q-mNeon had peak changes in fluorescence intensity ($\Delta F/F$) of 12.0 ± 0.8% (mean ± SEM; $N$ = 12 cells) and 8.5 ± 0.7% ($N$ = 10 cells), respectively, while leaving the spike waveform unperturbed (Figs. 2*A*,*B*, S4). Photobleaching rates were those of the constituent mNeonGreen, which is more photostable than EGFP (enhanced green fluorescent protein) (Shaner et al., 2013) and comparable with those of other brightly fluorescent voltage indicators (Table S2).

To quantitatively compare multiple indicators, we used a metric of spike-detection fidelity, $d'$, from signal detection theory (Wilt et al., 2013; Hamel et al., 2015). This metric accounts for an indicator's optical waveform in response to a spike and thus captures rates of correct and false spike detection better than other metrics such as signal-to-noise ratio (Materials and Methods are available at www.sciencemag.org/content/350/6266/1361/suppl/DC1). Modest improvements in $d'$ can have huge benefits for experimentation because false detection rates decline faster than exponentially with increases in $d'$ (Wilt et al., 2013; Hamel et al., 2015). Compared with MacQ-mCitrine, the superior brightness and peak $\Delta F/F$ responses of the Ace indicators increased $d'$ by factors of 2.2–3.0, with $d'$ values of 100 ± 12 (Ace2N-mNeon, mean ± SEM) and 70 ± 8 (Ace1Q-mNeon) in cultured neurons (Fig. 2*C*). Our calculations predicted this should be sufficient to image spikes >0.4 ms in duration not only in brain slices but also in live animals (Fig. S5).

Studies in mouse brain slices and live mice validated these predictions (Figs. 2*B*,*D*,*E*, 3*A*–*F*). To facilitate spike detection, we sparsely expressed the GEVIs using the SAD-ΔG viral vector, which efficiently transduces neurons through axons (Osakada et al., 2011). This labeling approach reduced background fluorescence from out-of-focal-plane or nonspecifically labeled sources. Previous studies with this virus have shown there is minimal toxicity in neurons up to 10 d postinfection (Osakada et al., 2011). We imaged thick brain slices 3–5 d after viral injection and found Ace2N-mNeon reported action potentials with $\Delta F/F$ = 6.5 ± 1.5% and $d'$ = 32 ± 5 (mean ± SEM; $n$ = 5 cells) (Fig. 2*B*). Neurons expressing the GEVI had statistically indistinguishable spike waveforms compared with nonfluorescent neurons in the same slices (Fig. S4).

We next imaged Ace2N-expressing neurons in the mouse visual cortex, using an indicator variant (Ace2N-4AA-mNeon) with four extra amino acids in the linker domain (Table S1). This variant yielded improved expression and superior visualization of individual cells' dynamics in live mice (Figs. 2*D*, 3A inset). Because extending the linker left the VSD unchanged, the voltage-dependent kinetics were unaffected, though the increased distance between the FRET pairs reduced the peak $\Delta F/F$ response to neural spikes (Fig. S6; Table S2). In anesthetized (Figs. 2*D*,*E*) and awake mice (Fig. 3), we readily observed spiking waveforms in labeled neurons in cortical layer 2/3, with interspike intervals as brief as ~10 ms—i.e., an interval 20-fold briefer than the signal integration time of the fast $Ca^{2+}$ indicator GCaMP6f (Chen et al., 2013).

Ace2N-4AA-mNeon also provided a high level of spike-detection fidelity ($d'$ = 16 ± 1.5, mean ± SEM; $N$ = 56 layer 2/3 neurons, ~150 μm below the brain surface; $N$ = 20 awake mice) at which the frequency of spike-detection errors is vastly less than with previous GEVIs. Imaging at a 1 kHz frame rate at a $d'$ value of 16 corresponds to a mean rate of $<10^{-7}$ detection errors per day (Wilt et al., 2013). Consistent with this, during simultaneous optical and loose-patch electrical recordings in the same neocortical neurons of anesthetized mice (Fig. 2*D*), the spike trains attained using Ace-4AA-mNeon and those from the electrical recordings were in perfect concordance (837 total spikes detected in dual recordings; $N$ = 3 mice). Highlighting the importance of Ace2N's approximately threefold increase in $d'$ over the best previous GEVIs, *in vivo* imaging with a value threefold lower ($d'$ = 5.3) leads to an unacceptable four spike-detection errors per second. The nearly vanishing error rate predicted at $d'$ = 16 is unattainable over hours under true experimental conditions owing to the indicator's finite photostability and nonstationary noise sources in the live brain other than photon shot noise. Nevertheless, this calculation underscores the huge impact of modest rises in $d'$, in that Ace2N has an

NOTES

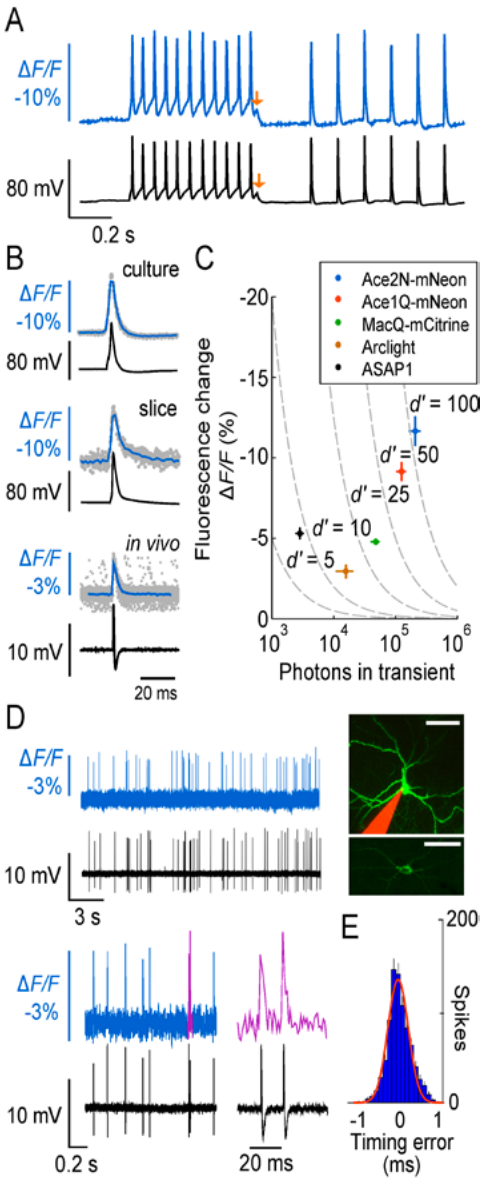


**Figure 2.** Ace sensors provide ~3- to 10-fold better spike-detection fidelity (*d'*) than previous GEVIs. ***A***, Fluorescence signals from cultured neurons expressing Ace2N-mNeon (blue trace) had sharp peaks closely matching action potentials in concurrent electrophysiological recordings (black trace). Red arrows mark a ~5 mV depolarization apparent in both traces. ***B***, Optical and electrical waveforms of single action potentials in example neurons expressing Ace2N-mNeon in cell culture (top), Ace2N-mNeon in mouse brain slice (middle), and Ace2N-4AA-mNeon in anesthetized mouse brain (bottom). Data (gray points) acquired optically from different spikes were temporally aligned to the corresponding peaks in the electrical traces. Mean waveforms of the optical data (blue traces; averaged over $N = 30$ spikes; resampled to 2 kHz) are aligned with the mean electrical waveforms (black traces; whole-cell patch recordings for cells in culture and brain slice; loose patch recording for live mouse). ***C***, Peak $\Delta F/F$ responses to action potentials, as a function of the total number of photons detected per spike in cultured neurons. Isocontours (dashed lines) of spike-detection fidelity, *d'*, were determined from measured brightness and optical waveforms, as in ***B***. Error bars: SEM. ***D***, Concurrent optical (colored) and juxtacellular electrical (black) recordings in an anesthetized mouse from V1 cells expressing Ace2N-4AA-mNeon. Magenta trace (lower right) shows the two magenta spikes in adjacent trace. Across 837 spikes, the electrical and optical traces were in perfect accord. Inset, Two different neocortical neurons imaged by two-photon microscopy. A maximum projection of a dual-color image stack (top) acquired in a live mouse shows an Ace2N-4AA-mNeon–labeled cell and a pipette, filled with red dye, that recorded somatic electrical activity. An image acquired in a brain slice (bottom) after *in vivo* experimentation shows the membrane localization of Ace2N-4AA-mNeon. Scale bars, 40 μm. ***E***, Histogram of timing errors for spikes detected optically, as in ***D***, using the electrical trace to provide the actual spike time ($N = 837$ spikes from 3 cells). Red line: Gaussian fit. Error bars: SD, estimated as counting errors. Illumination: 15, 25, and 25 mW · mm$^{-2}$, respectively, for studies in culture, brain slice, and live mice. Image acquisition rates: 440 Hz, 440 Hz, and 1000 Hz, respectively. Reprinted with permission from Gong et al. (2015), Fig. 2. Copyright 2015, American Association for the Advancement of Science.

NOTES

error rate that is orders of magnitude lower than previous GEVIs and is the first GEVI with acceptable error rates in the detection of single action potentials in live mammals.

Ace2N-4AA-mNeon also provided exquisite spike-timing accuracy, as determined from the dual optical and electrical recordings in live mice (Fig. 2*E*). Relative to the spike times in the electrical traces, the spike times in the optical traces differed by only 0.24 ± 0.01 ms (SEM; $N$ = 837 spikes) (see Materials and Methods available online). This degree of spike-timing accuracy approached the theoretical physical limits: 0.14 ± 0.03 ms set by quantum mechanical photon shot noise (Wilt et al., 2013; Hamel et al., 2015; Materials and Methods available online).

We also examined in awake mice whether individual cells' ongoing fluctuations in baseline Ace2N-4AA-mNeon emissions reflect subthreshold membrane voltage dynamics. If so, periods of optically reported membrane hyperpolarization should have reduced spike rates, and periods of reported depolarization should have elevated firing rates. This prediction proved correct for all 56 layer 2/3 neurons imaged in awake mice (Fig. 3*B*). As determined optically, each neuron fired spikes from baseline voltage levels that were significantly higher than its median resting potential ($p < 0.05$ for all 56 cells; Wilcoxon rank-sum test). As a population, the 56 cells were far more likely to fire spikes when the optically reported membrane voltages were above median resting levels ($p < 10^{-15}$; binomial test). Ace2N-4AA-mNeon also revealed submillisecond-scale features of dendritic voltage dynamics during spike generation (Fig. 3C; Movie S1). Thus, Ace2N reports aspects of individual cells' subthreshold, dendritic, and high-speed membrane potential dynamics in the live brain.

We next studied visually evoked spiking responses. To illustrate targeting of specific subclasses of visual cortical neurons, we expressed Ace2N-4AA-mNeon selectively in cells of the primary visual cortex (V1) that sent axons to the lateromedial area (LM) (denoted V1 → LM neurons), one of 15 cortical areas in mice that receive inputs from V1 (Wang and Burkhalter, 2007; Materials and Methods available online). We presented drifting grating visual stimuli to awake mice and imaged the cells' evoked responses. Generally, layer 2/3 V1 → LM neurons' evoked spiking was preferentially elicited by gratings of one orientation (4.1 ± 1.1 spikes · $s^{-1}$; mean ± SEM) versus the response (or suppression of activity) to gratings of the orthogonal orientation (1.0 ± 0.2 spikes · $s^{-1}$) (Figs. 3*D–F*; $N$ = 7 neurons from 5 mice; $p < 10^{-3}$; permutation test for each cell; $10^5$ permutations). The mean orientation selectivity index (0.82 ± 0.03; mean ± SEM), as determined from Ace2N-4AA-mNeon fluorescence traces, fit well with values determined by $Ca^{2+}$ imaging in the same neurons (Fig. 3*E*) and with previous studies (Niell and Stryker, 2008; Materials and Methods available online). There were also light-sensitive V1 → LM neurons that responded at the onset or offset of visual illumination regardless of the grating orientation (Fig. S8).

We also studied sensory-driven neural dynamics in live fruit flies, in which electrical recordings are often challenging. Beyond *in vivo* imaging of fast somatic spike trains, GEVIs have the potential to reveal fast voltage dynamics in genetically identified dendrites and axons. To illustrate, we imaged fast dynamics in the olfactory system and first examined local neurons (LNs) of the olfactory glomeruli (Chou et al., 2010), in which we used the R55D11-GAL4 fly driver line (Jenett et al., 2012) to express an Ace2N variant with two extra amino acids in the linker domain (Ace2N-2AA-mNeon) (Figs. 4A, S6; Table S2). The baseline spike rate in the absence of odor stimulation was 7.4 ± 2.8 $s^{-1}$ ($N$ = 8 neurons from 8 flies), comparable with electrophysiological measurements (Chou et al., 2010). In response to odor stimuli, we observed fast evoked spike trains in single trials at firing rates significantly above baseline ($p < 10^{-3}$; Wilcoxon signed rank test) (Fig. 4*B*). The peak odor-evoked spike rate was 65 ± 7 $s^{-1}$, i.e., the individual spikes fired about an order of magnitude faster than what $Ca^{2+}$ imaging can resolve.

As in mice, we performed dual optical and electrical recordings to verify the spike trains, this time using whole-cell patch-clamp electrodes to access LN neurons' intracellular potentials in intact fly brain explants (Fig. 4C, left). Across 18,141 recorded spikes, the spike trains provided by Ace2N-2AA-mNeon perfectly matched those from the patch-clamp recordings ($N$ = 4 fly brains) and had spike-timing errors of 0.19 ± 0.002 ms (SEM; $N$ = 18,141 spikes), close to the theoretical optimum of 0.11 ± 0.03 ms (Fig. 4C, right). Subthreshold dynamics were readily apparent in the optical traces, including plateau potentials and the rising and falling voltage waveforms surrounding action potentials. Ace2N-2AA-mNeon also reported the submillisecond-scale dynamics of spike back-propagation into the dendritic tree, revealing ~0.5–1.0 ms delays between the initiating voltage peak at the soma and those in the dendrites (Fig. 4*D*; Movie S2).

NOTES

We next imaged olfactory projection neurons (PNs), which generally have more selective odor tuning than LNs (Wilson et al., 2004; Olsen et al., 2007). We used live flies and focused on R26B04-GAL4–labeled PN dendritic arbors (Fig. 4*A*), which exclusively innervate the DL3 glomerulus (Wilson et al., 2004). In response to specific odors, the arbors exhibited fast, odor-evoked voltage dynamics with temporal structure at the 10–100 ms time scale (Figs. 4*E*,*F*). We compared these dynamics with those seen by $Ca^{2+}$ imaging using the GCaMP6f indicator (Fig. S9). The odor-tuning profiles determined from the two modalities were in broad agreement, but voltage imaging with Ace2N revealed both small-amplitude responses and fast temporal signals that GCaMP6f failed to convey (Fig. S9). Finally, we imaged the PN

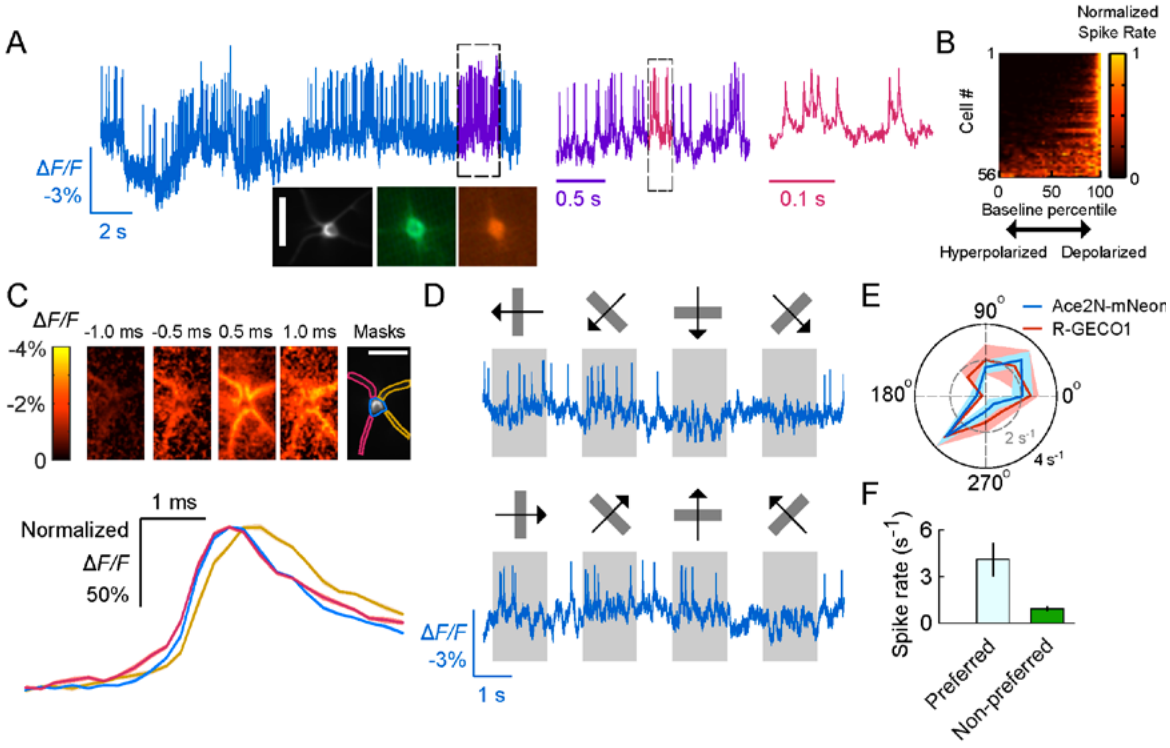


**Figure 3.** Imaging single action potentials and subthreshold membrane voltage fluctuations in layer 2/3 visual cortical neurons of awake mice. ***A***, Optical voltage trace acquired in an awake mouse, showing spiking by a V1 layer 2/3 neuron expressing Ace2N-4AA-mNeon via the SAD-Ace2N-4AA-mNeon-RGECO1 virus. Dashed boxes, Intervals shown at successively expanded time scales. Insets, Image acquired *in vivo* of the cell that provided the optical trace, and a pair of fluorescence images taken in a fixed tissue slice of an identically labeled V1 neuron from the same preparation expressing Ace2N-4AA-mNeon (green) and RGECO1 (red). Scale bar, 40 µm. ***B***, Periods of reduced spiking arose when Ace2N-4AA-mNeon reported a hyperpolarization. To track each cell's membrane voltage apart from its spikes, we applied a median filter (50 ms window) to the trace. For nonparametric comparisons, we matched each spike to the voltage at which the spike occurred, quantified as a percentile of the cell's full range of membrane voltages over the full recording. For each cell, the plot shows the spike rate (normalized to each cell's peak rate) at voltages across all percentiles. ***C***, Top, Spike-triggered average image frames for the cell in ***A***, showing the mean dendritic activation before and after firing an action potential. Times are relative to the spike peak at the soma. The left two dendrites activate before the right two dendrites. We calculated mean time traces for the soma and the left and right dendrite pairs using the spatial masks shown. Bottom, Mean fluorescence time courses (Δ*F*/*F*) for each of the three masks, normalized to the same maximum. The traces confirm the left-to-right activation pattern; the right dendrites exhibit a voltage peak 0.25–0.5 ms after the left dendrites. The Δ*F*/*F* image series and time traces were sampled in 0.25 ms time bins, using data from 1900 spikes mutually aligned to their peaks. Shaded regions on the time traces denote SEM and are barely discernible. ***D***, Example optical traces from a cortical V1 → LM neuron in an awake mouse, showing visually evoked responses to drifting gratings (orientations and motion directions marked above each trace). Spiking responses to the cell's preferred grating orientation (second column) differed from the activity suppression in response to the orthogonal orientation (fourth column). ***E***, Mean spike rates of the cell in ***D***, determined from the optical voltage trace in response to gratings moving in different orientations (10 trials per stimulus). Solid black and dashed gray circles indicate spike rates of 4 $s^{-1}$ and 2 $s^{-1}$, respectively. $Ca^{2+}$ imaging using RGECO1 in the same cell yielded similar orientation tuning. Evoked $Ca^{2}$ signals were integrated over 1 s and normalized so that $Ca^{2}$ and spiking responses to the preferred orientation (225°) were plotted at the same radius on the polar plot. Shaded areas indicate SEM. ***F***, Mean ± SEM spike rates in response to gratings at the preferred orientation were higher than to those oriented orthogonally ($p < 0.01$ for each of 7 cells; permutation test; $10^5$ permutations). Frame acquisition rates: voltage imaging, 1 kHz; $Ca^{2}$ imaging, 20 Hz. Illumination intensity: 20 and 10 mW · $mm^{-2}$, respectively, for voltage and $Ca^{2}$ imaging. Labeled neurons were ~150 µm below the brain surface. Reprinted with permission from Gong et al. (2015), Fig. 3. Copyright 2015, American Association for the Advancement of Science.

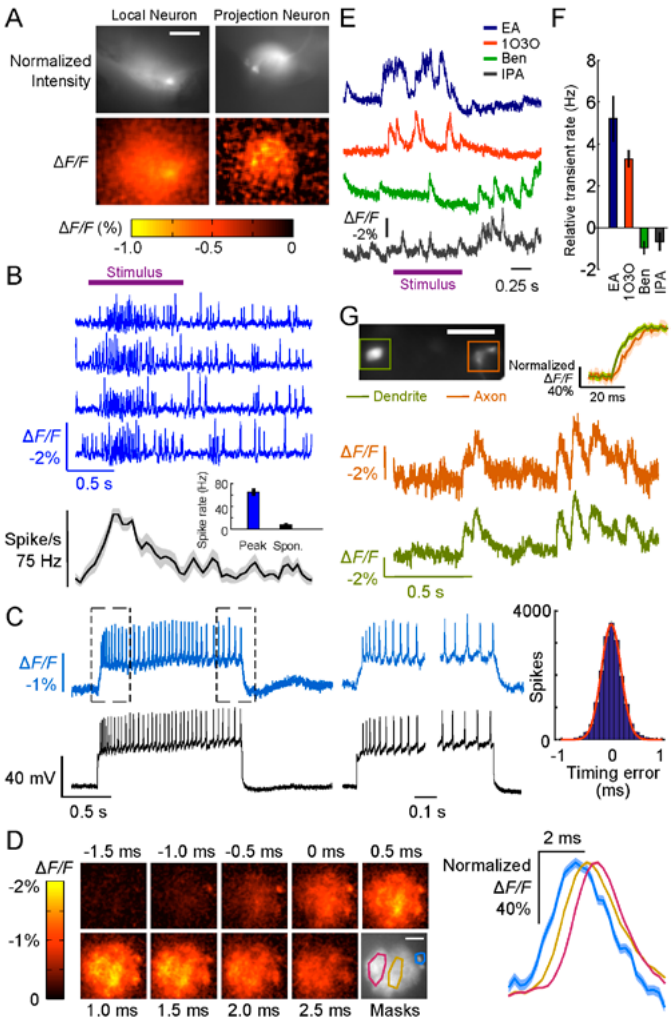


**Figure 4.** Odor-evoked spiking, dendritic dynamics, and voltage propagation delays in fly olfactory neurons. ***A***, Top, Fluorescence images of an LN (left) and a PN (right) expressing Ace2N-2AA-mNeon in the fly antenna lobe. Bottom, Spatial maps of the fluorescence response (Δ*F*/*F*) at the peak of an odor-evoked transient. Scale bar, 40 µm. ***B***, Top, Optical voltage traces (blue traces) from the LN in ***A*** reveal increased spiking during 5% benzaldehyde odor presentation (purple bar). Bottom, Odor-evoked spike rate as a function of time, averaged over five trials (shaded area denotes SEM). Inset, Mean peak spike rate during odor presentation was higher than baseline rates without odor ($p < 10^{-3}$; Wilcoxon signed rank test; $N = 8$ neurons and 8 flies [20 × UAS-Ace2N-2AA-mNeon/+; R55D11-GAL4/+]). ***C***, Left, Concurrent optical voltage and whole-cell patch electrical recordings in whole-brain explants from the same cell type as in ***B***. Spikes were evoked by current injection. Middle, Paired optical and electrical traces, taken from periods enclosed by dashed boxes in the left panel. Spikes are clearly distinguished in the optical traces from both the plateau of subthreshold depolarization and each rise to spike threshold. Right, Histogram of timing errors for the spikes detected optically, relative to the spike times in the whole-cell patch recordings ($N = 18{,}141$ spikes from 4 flies). Red line: Gaussian fit. SD of the timing errors: 0.19 ± 0.002 ms. Error bars estimating the SD as counting errors are too small to be seen. ***D***, Left, Spike-triggered average image frames for the cell in ***C***, showing the mean activation in the neural processes before and after firing a somatic spike, as determined from spike times in the electrical recording. Depolarization started at ~ –1.0 ms in the soma (upper right of each image) and propagated right to left across the dendritic tree during a spike. We calculated mean time traces for the soma and two subportions of the dendrites using the spatial masks in the lower right panel (cyan line encloses the soma; red and gold lines enclose dendritic regions). Scale bar, 40 µm. Right, Mean fluorescence traces (Δ*F*/*F*) for each of the three spatial masks, normalized to the same maximum. The traces confirm the right-to-left activation pattern; the left dendrites exhibited a voltage peak 0.5–0.7 ms after the right dendrites. Mean Δ*F*/*F* image series and traces were sampled in 0.25 ms bins, using data from 1300 spikes, temporally aligned to the spike peaks. Shaded regions denote SEM and are discernible only for the soma. ***E***, Odor-evoked, optical voltage traces from the DL3 projection neuron dendrites of ***A***, with significant rises in activity over baseline for some (10% ethyl acetate [EA] and 3-octanol [1O3O]; $p < 0.04$ for both EA and 1O3O) but not other odors (10% benzaldehyde [Ben] and isopropanol (IPA); $p = 1.0$ and 0.4 for Ben and IPA, respectively; Wilcoxon signed-rank tests; $N = 6$ flies; [20 × UAS-Ace2N-2AA-mNeon/+; R26B04-GAL4/+]). ***F***, Odor-evoked dendritic activation levels, relative to baseline levels. ***G***, Top, Example fly expressing Ace2N-2AA-mNeon in DL3 cells in which we concurrently imaged dendrites and axons. Bottom, Optical traces from both regions show concurrent activity. Inset, Averaged traces aligned to onset of dendritic activity reveal a ~4 ms propagation delay between dendrites and axons ($N = 30$ transients; shaded regions denote SEM). Scale bar, 50 µm. Illumination: 20 mW · mm$^{-2}$; frame acquisition rate: 1 kHz. For display only, each optical trace in ***B*** was high-pass filtered by subtracting a median-filtered (50 ms window) version of the trace. Traces in ***E*** were processed the same way for display, but with a 1 s filter window. Reprinted with permission from Gong et al. (2015), Fig. 4. Copyright 2015, American Association for the Advancement of Science.

NOTES

dendritic arbors and axonal boutons simultaneously. Odor-evoked voltage signals in the two structures were similar, but there was a 3.7 ± 0.4 ms (mean ± SEM; $N = 3$ flies) propagation delay from dendrites to axons (Fig. 4G). Neither $Ca^{2+}$ imaging nor electrical recordings have been capable of revealing this type of fast, intracellular signal propagation in a live animal.

By virtue of their bright emissions, fast (<1 ms) kinetics, and targeted expression, Ace2N GEVIs open a wide range of experimental avenues in optical neurophysiology. Their capabilities to track fast spiking, subthreshold dynamics, and sensory-evoked and back-propagating dendritic voltage activity *in vivo* enable direct visualization of many temporal features of neural dynamics, plasticity induction, and coding that have long been inaccessible. When combined with chronic animal preparations (Hamel et al., 2015), it will be possible to track these phenomena over multiple days. Ace2N sensors resolved sensory-evoked spike trains with firing rates as high as ~75 $s^{-1}$ (the fastest we encountered) with ~0.2 ms timing accuracy. Whereas *in vivo* $Ca^{2+}$ imaging usually resolves successive spikes if they are ~50–250 ms apart and has ~20–100 ms timing accuracy for isolated spikes (Chen et al., 2013; Inoue et al., 2015), Ace2N sensors directly reveal the constituent spikes in bursts—a widespread and important means of neural signaling (Lisman, 1997; Mathy et al., 2009). The Ace2N sensors' timing precision is also key to resolving long-standing debates over the temporal attributes of neural coding (Diba et al., 2014; Zuo et al., 2015).

The retrograde labeling strategy we used to express the Ace2N indicator in live mice also holds importance for future work, in that every soma we imaged had an axon at the virus injection site. This allowed us to target the subclass of V1 neurons with projections to area LM. A logical next step in the study of V1 would be systematic voltage imaging of visually evoked spiking across all 15 subclasses of V1 neurons, as categorized by their axonal projections (Wang and Burkhalter, 2007). There are long-standing *in vivo* electrophysiological methods for identifying cells with specific axonal projections (Hahnloser et al., 2002), but they are technically onerous to an extent that has precluded widespread and routine use. Voltage imaging is now poised to make commonplace the study of neural dynamics in live mammals in chosen anatomical projection pathways.

Until now, subthreshold neural voltage dynamics have usually been inaccessible in live animals, especially in fine neural processes in which intracellular recordings are nearly prohibitive. As shown here, Ace-mNeon reveals fast dendritic activity, including stimulus-evoked dynamics and spike back-propagation. This is especially important for studies of flies and other species in which fine neurites are vital to information processing (Borst et al., 2010). There is also rising appreciation of the importance of dendritic computation in mammalian neurons (Smith et al., 2013; Sheffield and Dombeck, 2015). Ace-2N should allow direct observations of such phenomena *in vivo*.

For our *in vivo* imaging studies, we used wide-field epifluorescence microscopy, 1 kHz imaging rates, and sparse fluorescence labeling. Fluorescent V1 → LM neural somata were usually ~150 μm below the brain surface and separated by ~40–60 μm (Fig. S7). This separation enabled high-fidelity tracking of neural spiking despite the lack of optical sectioning and the consequent background fluorescence. Comparable performance should also be feasible in deep brain areas by using microendoscopes to access deep tissues (Hamel et al., 2015). Studies of both surface and deep neural ensembles would benefit from improved scientific-grade cameras for fast imaging (1 kHz) at cellular resolution over broader fields of view than are possible today. For comparison, $Ca^{2+}$ imaging studies (10–20 Hz) capture 100-fold larger specimen areas than those sampled here at 1 kHz (Hamel et al., 2015).

In principle, microscopy modalities with optical sectioning should also allow denser fluorescence labeling patterns and deeper optical penetration through thick tissue. A challenge, however, is that nearly all extant *in vivo* microscopy modalities with sectioning involve laser scanning, with pixel dwell times typically ~0.1–2 μs for frame rates of ~10–20 Hz. Given the importance of detecting as many signal photons as possible with voltage imaging, conventional laser scanning is plainly insufficient at the faster frame rates used for *in vivo* voltage imaging (~0.5–1 kHz). The introduction of Ace2N indicators for *in vivo* voltage imaging puts a premium on the innovation of microscopes that provide optical sectioning without conventional laser scanning. The emergence of scanless forms of optical sectioning microscopy holds particular interest for the further development of *in vivo* voltage imaging capabilities (Watson et al., 2010; Prevedel et al., 2014). Even with existing optical hardware, Ace-mNeon's capacities for targeted imaging of cells of identified types or axonal projections, resolution of fast spike trains, accurate estimation of spike timing, and observation of subthreshold and dendritic voltage dynamics open many questions to empirical study that hitherto could not be examined in live animals.

NOTES

## Acknowledgments

This chapter was reprinted with permission from a previously published article: Gong et al. (2015) High-speed recording of neural spikes in awake mice and flies with a fluorescent voltage sensor. Science 350:1361–1366. Copyright 2015, American Association for the Advancement of Science. We gratefully acknowledge research funding from the Defense Advanced Research Projects Agency, a National Institutes of Health (NIH) Pioneer award, an NIH Brain Research through Advancing Innovative Neurotechnologies (BRAIN) Initiative U01 grant, and the Stanford Neurosciences Institute CNC (Cracking the Neural Code) program. We thank Jane Li for animal husbandry. Genetic sequence data, as well as supplementary tables, figures, and movies, are available online at www.sciencemag.org/content/350/6266/1361/suppl/DC1.

## References

Borst A, Haag J, Reiff DF (2010) Fly motion vision. Annu Rev Neurosci 33:49–70.

Chen TW, Wardill TJ, Sun Y, Pulver SR, Renninger SL, Baohan A, Schreiter ER, Kerr RA, Orger MB, Jayaraman V, Looger LL, Svoboda K, Kim DS (2013) Ultrasensitive fluorescent proteins for imaging neuronal activity. Nature 499:295–300.

Chou YH, Spletter ML, Yaksi E, Leong JC, Wilson RI, Luo L (2010) Diversity and wiring variability of olfactory local interneurons in the *Drosophila* antennal lobe. Nat Neurosci 13:439–449.

Diba K, Amarasingham A, Mizuseki K, Buzsáki G (2014) Millisecond timescale synchrony among hippocampal neurons. J Neurosci 34:14984–14994.

Gong Y, Wagner MJ, Li JZ, Schnitzer MJ (2014) Imaging neural spiking in brain tissue using FRET-opsin protein voltage sensors. Nat Commun 5:3674.

Gong Y, Huang C, Li JZ, Grewe BF, Zhang Y, Eismann S, Schnitzer MJ (2015) High-speed recording of neural spikes in awake mice and flies with a fluorescent voltage sensor. Science 350:1361–1366.

Hahnloser RH, Kozhevnikov AA, Fee MS (2002) An ultra-sparse code underlies the generation of neural sequences in a songbird. Nature 419:65–70.

Hamel EJ, Grewe BF, Parker JG, Schnitzer MJ (2015) Cellular level brain imaging in behaving mammals: an engineering approach. Neuron 86:140–159.

Hochbaum DR, Zhao Y, Farhi SL, Klapoetke N, Werley CA, Kapoor V, Zou P, Kralj JM, Maclaurin D, Smedemark-Margulies N, Saulnier JL, Boulting GL, Straub C, Cho YK, Melkonian M, Wong GK, Harrison DJ, Murthy VN, Sabatini BL, Boyden ES, et al. (2014) All-optical electrophysiology in mammalian neurons using engineered microbial rhodopsins. Nat Methods 11:825–833.

Inoue M, Takeuchi A, Horigane S, Ohkura M, Gengyo-Ando K, Fujii H, Kamijo S, Takemoto-Kimura S, Kano M, Nakai J, Kitamura K, Bito H (2015) Rational design of a high-affinity, fast, red calcium indicator R-CaMP2. Nat Methods 12: 64–70.

Jenett A, Rubin GM, Ngo TT, Shepherd D, Murphy C, Dionne H, Pfeiffer BD, Cavallaro A, Hall D, Jeter J, Iyer N, Fetter D, Hausenfluck JH, Peng H, Trautman ET, Svirskas RR, Myers EW, Iwinski ZR, Aso Y, DePasquale GM, et al. (2012) A GAL4-driver line resource for *Drosophila* neurobiology. Cell Rep 2:991–1001.

Jin L, Han Z, Platisa J, Wooltorton JR, Cohen LB, Pieribone VA (2012) Single action potentials and subthreshold electrical events imaged in neurons with a fluorescent protein voltage probe. Neuron 75:779–785.

Knopfel T (2012) Genetically encoded optical indicators for the analysis of neuronal circuits. Nat Rev Neurosci 13:687–700.

Lisman JE (1997) Bursts as a unit of neural information: making unreliable synapses reliable. Trends Neurosci 20:38–43.

Lundby A, Mutoh H, Dimitrov D, Akemann W, Knöpfel T (2008) Engineering of a genetically encodable fluorescent voltage sensor exploiting fast Ci-VSP voltage-sensing movements. PLoS One 3:e2514.

Mathy A, Ho SS, Davie JT, Duguid IC, Clark BA, Häusser M (2009) Encoding of oscillations by axonal bursts in inferior olive neurons. Neuron 62:388–399.

Niell CM, Stryker MP (2008) Highly selective receptive fields in mouse visual cortex. J Neurosci 28:7520–7536.

Olsen SR, Bhandawat V, Wilson RI (2007) Excitatory interactions between olfactory processing channels in the *Drosophila* antennal lobe. Neuron 54:89–103.

Osakada F, Mori T, Cetin AH, Marshel JH, Virgen B, Callaway EM (2011) New rabies virus variants for monitoring and manipulating activity and gene expression in defined neural circuits. Neuron 71:617–631.

Peterka DS, Takahashi H, Yuste R (2011) Imaging voltage in neurons. Neuron 69:9–21.

Prevedel R, Yoon YG, Hoffmann M, Pak N, Wetzstein G, Kato S, Schrödel T, Raskar R, Zimmer M, Boyden ES, Vaziri A (2014) Simultaneous whole-animal 3D imaging of neuronal activity using light-field microscopy. Nat Methods 11:727–730.

Shaner NC, Lambert GG, Chammas A, Ni Y, Cranfill PJ, Baird MA, Sell BR, Allen JR, Day RN, Israelsson M, Davidson MW, Wang J (2013) A bright monomeric green fluorescent protein derived from *Branchiostoma lanceolatum*. Nat Methods 10:407–409.

Sheffield ME, Dombeck DA (2015) Calcium transient prevalence across the dendritic arbour predicts place field properties. Nature 517:200–204.

Smith SL, Smith IT, Branco T, Häusser M (2013) Dendritic spikes enhance stimulus selectivity in cortical neurons *in vivo*. Nature 503:115–120.

St-Pierre F, Marshall JD, Yang Y, Gong Y, Schnitzer MJ, Lin MZ (2014) High-fidelity optical reporting of neuronal electrical activity with an ultrafast fluorescent voltage sensor. Nat Neurosci 17:884–889.

Tsunoda SP, Ewers D, Gazzarrini S, Moroni A, Gradmann D, Hegemann P (2006) H+-pumping rhodopsin from the marine alga *Acetabularia*. Biophys J 91:1471–1479.

Tsutsui H, Karasawa S, Okamura Y, Miyawaki A (2008) Improving membrane voltage measurements using FRET with new fluorescent proteins. Nat Methods 5:683–685.

Wang Q, Burkhalter A (2007) Area map of mouse visual cortex. J Comp Neurol 502:339–357.

Watson BO, Nikolenko V, Araya R, Peterka DS, Woodruff A, Yuste R (2010) Two-photon microscopy with diffractive optical elements and spatial light modulators. Front Neurosci 4:29.

Wilson RI, Turner GC, Laurent G (2004) Transformation of olfactory representations in the *Drosophila* antennal lobe. Science 303:366–370.

Wilt BA, Fitzgerald JE, Schnitzer MJ (2013) Photon shot noise limits on optical detection of neuronal spikes and estimation of spike timing. Biophys J 104:51–62.

Zou P, Zhao Y, Douglass AD, Hochbaum DR, Brinks D, Werley CA, Harrison DJ, Campbell RE, Cohen AE (2014) Bright and fast multicoloured voltage reporters via electrochromic FRET. Nat Commun 5:4625.

Zuo Y, Safaai H, Notaro G, Mazzoni A, Panzeri S, Diamond ME (2015) Complementary contributions of spike timing and spike rate to perceptual decisions in rat S1 and S2 cortex. Curr Biol 25:357–363.

NOTES

# High-Resolution and High-Speed *In Vivo* Imaging of the Brain

Cristina Rodriguez, PhD,[1] and Na Ji, PhD[2]

[1]Department of Physics, University of California, Berkeley
Berkeley, California

[2]Department of Physics, Department of
Molecular and Cellular Biology
Helen Wills Neuroscience Institute
University of California, Berkeley
Lawrence Berkeley National Laboratory
Berkeley, California

NOTES

## Introduction

Understanding neural computation requires the ability to measure how a neuron integrates its multitude of synaptic inputs, as well as how neural ensembles work together during sensory stimulation and motor control. Optical microscopy enables the discovery of physical structures and phenomena otherwise invisible or unresolvable to the naked eye. Starting with Ramón y Cajal's identification using optical microscopes of neurons as the elementary computational unit of the brain (Cajal, 2002), neuroscience has greatly benefited from the development of optical microscopy technology. This chapter reviews select recent works on high-resolution and high-speed *in vivo* imaging of the brain.

## High-Resolution *In Vivo* Imaging Using Adaptive Optics

Owing to the wave nature of light, the resolution of conventional optical microscopes is limited by diffraction to approximately half the wavelength of light. In practice, however, optimal performance of microscopes is achievable only under limited conditions, requiring specific coverglass thickness and immersion medium. Additionally, the optical properties of the specimen and the immersion medium need to be matched. The latter is seldom achieved for most biological samples, including the brain, whose very own mixture of ingredients (e.g., water, proteins, nuclear acids, and lipids) gives rise to spatial variations in its refractive index. Such inhomogeneities induce wavefront aberrations, leading to a degradation in the resolution and contrast of microscope images that further deteriorates with imaging depth (Schwertner et al., 2004a,b).

By measuring the accumulated distortion of light as it travels through inhomogeneous specimens, and correcting for it using wavefront shaping devices such as deformable mirrors and liquid-crystal spatial light modulators (SLMs), adaptive optics (AO) can recover diffraction-limited performance deep within living systems. The optical aberrations involved in image formation (Fig. 1) can be detected by measuring the point-spread function (PSF) of the microscope, typically by imaging a point object of subdiffraction dimensions (e.g., fluorescent bead) in three dimensions (3*D*). Deviation from the ideal PSF indicates the presence of aberrations, an effect that is often easier to detect on the axial plane (Fig. 1*b*).

The implementation of AO in microscopy depends on how image formation is attained in the specific microscopy modality. For example, in laser scanning microscopy (e.g., confocal and multiphoton microscopy), specimen-induced aberrations distort the wavefront of the excitation light and prevent the formation of a diffraction-limited focal spot (Fig. 1). For multiphoton microscopes, where the signal is detected by a nonimaging detector (e.g., a photomultiplier tube [PMT]), aberration correction is needed only for the excitation light. In a confocal microscope, aberration correction is implemented in both the excitation light (providing a diffraction-limited excitation confinement) and the fluorescence emission (ensuring the in-focus fluorescence passes through the confocal pinhole), and can be accomplished using the same wavefront correction device located in a common path. In a wide-field microscope, aberration correction is usually applied only to the emitted fluorescence, which has to travel through the aberrating sample before image formation takes place on a camera.

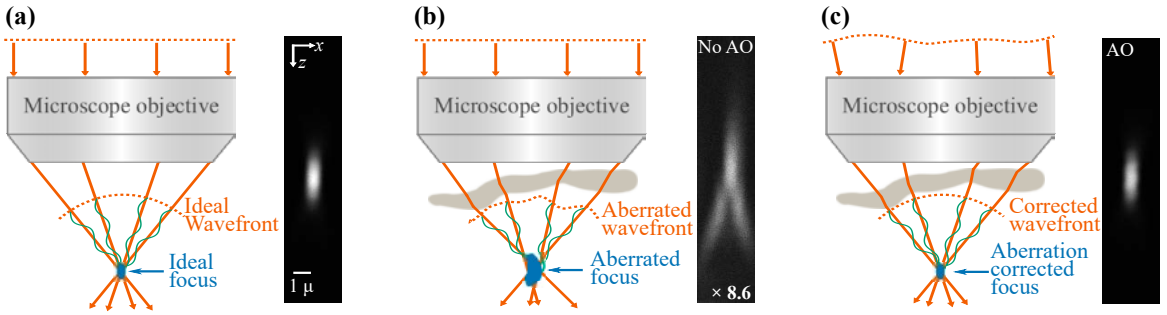


**Figure 1.** The effect of aberrations on image quality. ***a***, An aberration-free wavefront leads to a diffraction-limited focal spot in a point-scanning (e.g., two-photon fluorescence) microscope. ***b***, Specimen refractive-index mismatches distort the wavefront of the excitation light, leading to a dim, enlarged focus. ***c***, Optimal imaging performance can be recovered by preshaping the wavefront of the excitation light to cancel out the specimen-induced aberration. The sinusoidal curves denote the phase relationship among the rays. Axial images obtained from two-photon excitation of 1 μm fluorescent red beads are shown for three different cases: ***a***, ideal, aberration-free imaging conditions; ***b***, an artificial aberration is introduced, causing a 8.6-fold decrease in brightness and a degradation of axial resolution; and ***c***, AO is used to recover ideal imaging performance. Scale bar: ***a***, 1 μm. Modified with permission from Rodríguez and Ji (2018), Fig. 1. Copyright 2018, Elsevier.

NOTES

## Adaptive Optics Methods in Microscopy

The different implementations of AO in microscopy (Kubby, 2013; Booth, 2014; Booth et al., 2015; Ji, 2017) differ mainly in how the aberration is measured and are commonly classified into direct and indirect wavefront sensing methods.

### Direct wavefront sensing methods

Direct wavefront sensing methods make use of a dedicated wavefront sensor, such as a Shack–Hartmann (SH) wavefront sensor, to directly measure wavefront aberrations (Fig. 2) from a light-emitting point-like source generated via fluorescence excitation or backscattering of the excitation light (Rodriguez and Ji, 2018). Light from such a "guide star" accumulates aberrations as it propagates through the sample and the instrument before reaching the SH sensor, consisting of a two-dimensional (2D) array of lenses and a camera (Fig. 2*a*). The local slope of each wavefront segment can be determined from the displacement of the focus of the corresponding light ray from its aberration-free position on a camera placed at the focal plane of the lenslet array (Fig. 2*b*). By assuming a continuous wavefront, the phase offset of each segment can be calculated (Southwell, 1980) and the wavefront reconstructed. This information is then used to control the wavefront shaping device in order to compensate for instrument-induced and sample-induced aberrations before image formation. Because wavefront aberration is obtained in a single measurement, direct sensing and correction can operate at high speed (e.g., milliseconds). Accurate wavefront aberration measurements from such a direct wavefront sensing scheme are possible only when enough ballistic (unscattered) light reaches the wavefront sensor. As such, this method works well in brains that are either transparent or weakly scattering.

### Indirect wavefront sensing schemes

Indirect wavefront sensing schemes, needing only a wavefront shaping device, are typically easier to implement in existing microscopes and can be readily used for scattering samples (Fig. 3).

#### *Pupil segmentation*

One of several indirect methods, based on pupil segmentation, relies on similar physical principles as SH wavefront sensors. By measuring lateral image shifts when different pupil subregions are sequentially illuminated, the local slope of each wavefront segment can be calculated (Ji et al., 2010). The phase of each segment can then be obtained by direct interference measurements (Liu et al., 2014) or through reconstruction algorithms. By illuminating one pupil segment at a time, each image is taken under a lower numerical aperture (NA) with an enlarged focus. As a result, the images can contain contributions from structures originally beyond the excitation volume under full-pupil illumination, making image-shift measurements difficult in densely labeled samples. Alternatively, the entire pupil can be illuminated at all times (Milkie et al.,

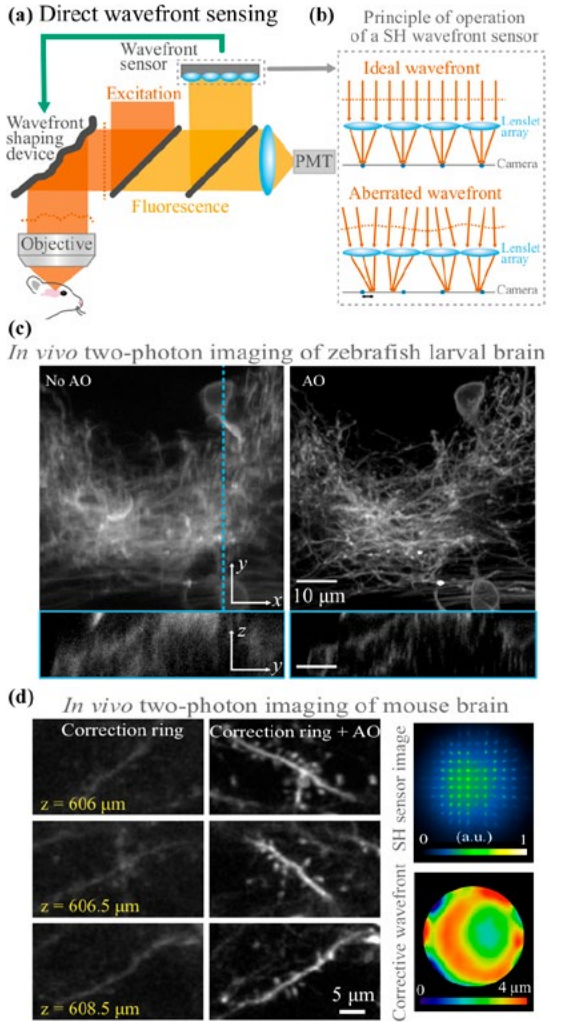


**Figure 2.** AO microscopy using direct wavefront sensing. ***a***, 2PFM using an SH sensor. ***b***, A wavefront is incident on a SH wavefront sensor, where an array of lenslets focuses the light into a 2D array of foci onto a camera. The local slopes of wavefront segments can be measured from the displacements of the foci relative to their aberration-free positions. ***c***, Two-photon *in vivo* imaging of zebrafish larval brain obtained without (left) and with (right) AO correction (Wang et al., 2014a). ***d***, Two-photon *in vivo* imaging of dendritic spines in the mouse brain obtained without (left) and with (center) AO correction, and an SH sensor image with its corresponding corrective wavefront (right) (Wang et al., 2015). Scale bars: ***c***, 10 μm; ***d***, 5 μm. Modified with permission from Rodríguez and Ji (2018), Fig. 2. Copyright 2018, Elsevier.

NOTES

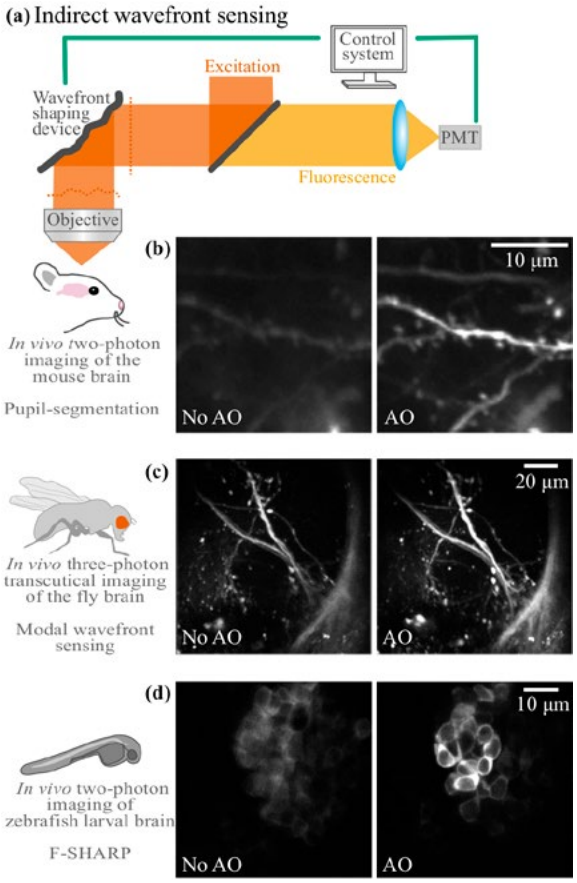


**Figure 3.** AO microscopy using indirect wavefront sensing. ***a***, An AO two-photon fluorescence microscope. ***b***, Two-photon maximal-intensity projection images of dendrites at 376–395 μm below dura measured without (left) and with (right) AO in the mouse brain *in vivo*, using the frequency-multiplexed pupil-segmentation method (Wang et al., 2014b). ***c***, *In vivo* three-photon transcutical imaging in the lateral horn of the fly brain (Tao et al., 2017). ***d***, Two-photon *in vivo* imaging of zebrafish larval brain obtained without (left) and with (right) AO correction, 300 μm under the brain surface, using F-SHARP (Papadopoulos et al., 2017). Scale bars: ***b***, 10 μm; ***c***, 20 μm; ***d***, 10 μm. Modified with permission from Rodríguez and Ji (2018), Fig. 3. Copyright 2018, Elsevier.

2011), thus maintaining the full excitation NA and rendering this approach applicable to samples of arbitrary labeling density. Scanning one ray around the aberrated reference focus formed by the remaining rays, while monitoring the variation of the signal strength, reveals the additional tilt needed for maximal interference, ultimately yielding the local slope of this wavefront segment. To speed up the aberration measurement and improve the signal-to-noise ratio, gradients of multiple wavefront segments can be determined in parallel through frequency multiplexing (Wang et al., 2014b).

### *Modal wavefront sensing*

Another indirect approach, known as modal wavefront sensing, involves acquiring a series of images while intentionally distorting the wavefront by a known combination of orthogonal aberration modes (e.g., Zernike polynomials) using a wavefront shaping device. The wavefront is adjusted iteratively until a certain image metric is optimized, such as brightness or sharpness (Booth, 2006; Débarre et al., 2007; Zeng et al., 2012; Galwaduge et al., 2015).

### *Focus scanning holographic aberration probing: F-SHARP*

A different wavefront correction approach, termed "focus scanning holographic aberration probing" (F-SHARP), directly measures the amplitude and phase of the scattered electric field PSF via the interference of two excitation beams, allowing for fast wavefront correction of both aberrations and scattering at high resolution (Papadopoulos et al., 2017). Placing a wavefront shaping element at a Fourier plane to the image plane, the required correction pattern is the 2D Fourier transform of the measured PSF of the scattered electric field.

## High-Resolution Morphological Imaging of Neurons *In Vivo*

In the following sections, we review a number of recent experimental findings that illustrate how neurobiology has benefited from using AO microscopy to correct for brain-induced aberrations and achieve high-resolution imaging *in vivo*, allowing individual synaptic terminals to be resolved at greater depth.

### Fast direct wavefront sensing schemes

Using a fast direct wavefront sensing scheme with two-photon excited visible fluorescent guide stars, diffraction-limited two-photon imaging was demonstrated in large volumes (>240 μm per side) in zebrafish larval brains *in vivo* (Fig. 2*c*) (Wang et al., 2014a). This correction scheme was also applied to multicolor diffraction-limited confocal imaging in the zebrafish brain down to 200 μm resolution, allowing for the study of subcellular organelles (Wang et al., 2014a). By making use of the reduced tissue scattering of near infrared guide stars, the applicability of direct wavefront sensing was extended to tissues that strongly scatter visible light (Wang et al., 2015). Such an approach allowed *in vivo* two-photon microscopy imaging of the mouse brain at greater depth (Fig. 2*d*), with the ability to resolve synaptic structures down to 760 μm.

NOTES

## Indirect wavefront sensing methods

To use the visible fluorescent signal for wavefront sensing in scattering brain tissue at depth, indirect wavefront sensing methods need to be used. In one of the early demonstrations of AO microscopy for *in vivo* brain imaging, a pupil-segmentation approach with single-segment illumination allowed for diffraction-limited two-photon imaging 450 μm below the surface of the mouse brain *in vivo* (Ji et al., 2012). The same method has also been used to correct for system aberrations in two-photon fluorescence microendoscopy (Wang and Ji, 2012; Wang et al., 2012, 2013). For more densely labeled samples, the frequency-multiplexed pupil-segmentation method proved successful at measuring and correcting for aberrations during *in vivo* two-photon imaging of *Caenorhabditis elegans*, zebrafish larva, and mouse brains (Wang et al., 2014b). With synaptic-level resolution achievable using such a scheme, it was possible to resolve submicrometer-sized spines inside a *thy1-YFP* line H mouse brain at depth (Fig. 3*b*). For a more densely labeled brain—wild-type mouse with viral GCaMP6s (Chen et al., 2013) expression—a single correction improved image quality from 427 μm to 547 μm depth; after AO correction, fine neuronal processes and even the much larger somata went from invisible to clearly resolvable.

Other indirect wavefront sensing methods have been used to improve the signal and contrast during *in vivo* brain imaging. Modal approaches have been used to improve image quality in two-photon imaging of the mouse brain *in vivo* (Galwaduge et al., 2015; Park et al., 2017). Three-photon fluorescence microscopy, where longer excitation wavelengths lead to reduced light scattering and larger *in vivo* imaging depth (Horton et al., 2013; Ouzounov et al., 2017), also benefits from AO correction (Sinefeld et al., 2015). The greater penetration depth of three-photon excitation allowed transcuticle three-photon imaging of neuronal structures in the lateral horn of the fly brain, where a modal approach was used to correct the aberration introduced by the cuticle and the brain (Fig. 3*c*) (Tao et al., 2017). F-SHARP (Papadopoulos et al., 2017) can compensate for both aberrations and scattering, enabling the acquisition of high-contrast images inside turbid tissue, including zebrafish larva and mouse brain *in vivo* (Fig. 3*d*).

## General rules

Some general rules can be recognized from these studies:

(1) Aberrations in the adult brains are usually temporally stable when compared with the imaging period (Ji et al., 2012). This makes the speed of aberration correction a less crucial factor and allows both direct and indirect wavefront sensing methods to achieve effective corrections.

(2) The mouse brain has limited curvature (often further reduced by the cranial window that presses on the brain), which allows a single correction to improve image quality over hundreds of micrometers in 3D (Ji et al., 2012; Wang et al., 2014b, 2015). The low spatiotemporal variation of brain-induced aberrations therefore facilitates the application of AO microscopy to mouse brains, where aberration correction needs to be performed only at the beginning of an imaging session, with the resulting correction improving the image quality throughout the hours of experiments to follow. In contrast, in highly curved samples such as zebrafish larval brain (Wang et al., 2015) or *C. elegans* (Wang et al., 2014b), corrective patterns are often highly local, and a single aberration correction may improve image quality only in the close vicinity (tens of micrometers) of where the wavefront was measured. For such samples, direct wavefront sensing, if applicable, is the preferred choice due to its high correction speed.

(3) In scattering tissue (e.g., adult brains), to compensate for the exponential loss of ballistic photons with imaging depth, one has to increase the excitation power exponentially. Eventually, the electric field strength at the surface of the brain becomes high enough to generate a two-photon fluorescence signal without the need for focal confinement. When the out-of-focus fluorescence signal overwhelms the in-focus signal, the ultimate imaging depth limit of two-photon fluorescence microscopy (2PFM) is reached (Theer et al., 2003). Because AO increases focal intensity and thus in-focus signal, but affects out-of-focus signal minimally (Wang et al., 2014b), correcting brain-induced aberrations increases the imaging depth limits.

(4) One consistent observation is that correcting the same specimen-induced aberration improves the brightness of small features (e.g., synaptic terminals) more than large features (e.g., somata) (Ji et al., 2012; Wang et al., 2014b). This is because aberrations lead to an enlarged focal volume and weaker light intensity. The signal of small features approaching a point object depends on local light intensity, and thus is substantially reduced by the focal intensity loss in an aberrated focus. For large extended features, on the other hand, the

NOTES

reduction of focal intensity is partly compensated by the increase in focal volume, which allows more fluorophores to contribute to the final signal. In other words, whereas fluorescent probes and excitation strategies utilizing a longer wavelength range allow cell bodies to be visualized at increasing depths (Dana et al., 2016; Kondo et al., 2017; Ouzounov et al., 2017), AO is required when synapse-sized structures are to be imaged at depth.

## High-Resolution Functional Imaging of Neurons *In Vivo*

An important class of neurobiology experiments involves measuring neural activity with fluorescent indicators. The most popular example is measuring calcium transients using genetically encoded calcium indicators (GECIs) (Chen et al., 2013; Yang and Yuste, 2017). AO correction leads to a more accurate characterization of the functional properties of neurons.

Similar to morphological imaging, AO correction improves the brightness and contrast of functional images (Fig. 4*a*). In addition, it has been consistently observed that the amplitude of calcium transients increases after AO correction (Ji et al., 2012; Wang et al., 2014b; Wang et al., 2015; Sun et al., 2016), a result of the reduced excitation focal volume and enhanced focal brightness after aberration correction. In brains densely labeled with fluorescent sensors (e.g., through bulk loading [Ji et al., 2012], viral injection [Wang et al., 2014b], or transgenic expression [Wang et al., 2015; Park et al., 2017]), another challenge arises: In addition to the more brightly labeled neurons of interest (the ones from which regions of interest [ROIs] are chosen), a spatially diffuse neuropil

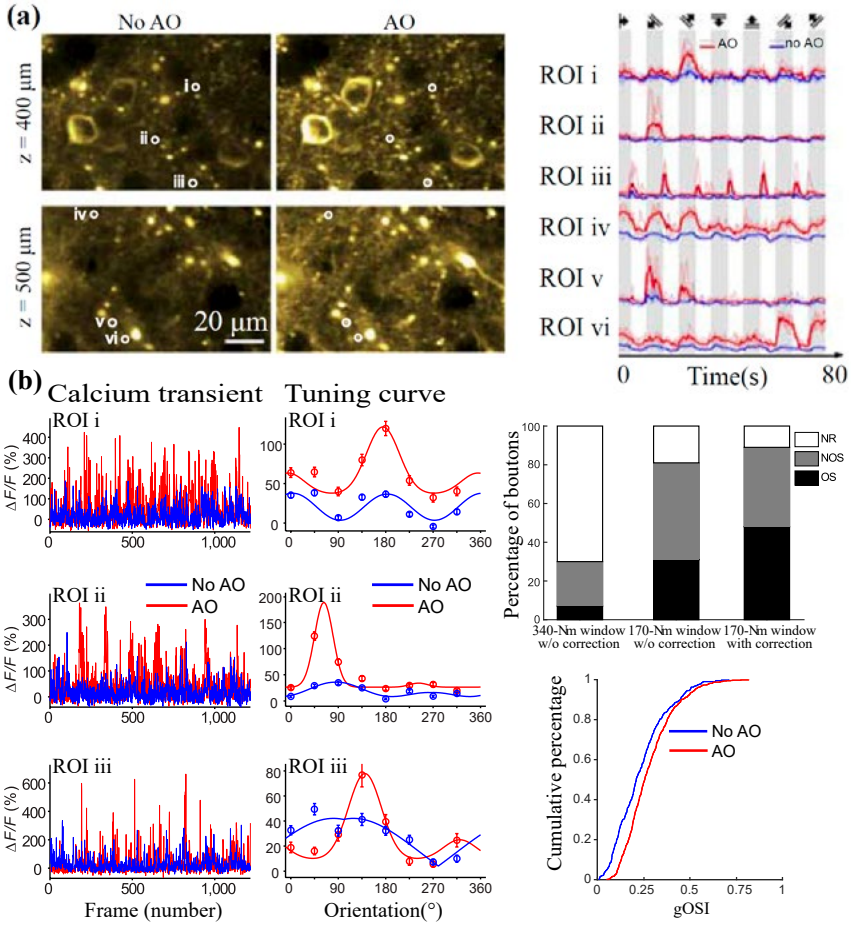


**Figure 4.** AO improves the accuracy of calcium activity measurements. ***a***, Calcium transients evoked by the stimulation of a drifting grating, 400 and 500 µm below pia in the primary visual cortex of a mouse (*Thy1*-GCaMP6s line GP4.3) without (left) and with (center) AO correction. Calcium transients at ROIs i–vi, without and with AO correction (right). ***b***, Calcium transients (left) and tuning curves (center) for three different ROIs taken from images of GCaMP6s$^+$ thalamic axons without (blue traces) and with (red traces) AO, at a depth of 170 µm. Top right, Percentages of nonresponsive (NR), not orientation selective (NOS), and orientation selective (OS) boutons; Bottom right, Cumulative distributions of gOSI for boutons measured without and with AO. Cranial window thickness is 170 µm. Scale bar: ***a***, 20 µm. Modified with permission from Rodríguez and Ji (2018), Fig. 4. Copyright 2018, Elsevier.

NOTES

background consists of more weakly labeled neurons. Because this signal is an average of many neurons and is generally less correlated with the stimulus feature, it is considered a contamination (Göbel and Helmchen, 2007). As explained in the previous sections, however, aberration correction increases the signal from our spatially confined ROI more than that from the neuropil contamination, and thus increases the strength of calcium transients.

AO correction also leads to a sharpening of the tuning curves for orientation in the mouse visual pathway, characterized by the selectivity of neurons toward drifting gratings of various orientations (Fig. 4). When imaging thalamic boutons located in the primary visual cortex of awake mice (Fig. 4*b*), the percentage of visually responsive boutons (as well as those classified as orientation selective) was found to steadily increase with decreasing amounts of aberration (Sun et al., 2016). For example, with a 340-μm-thick cranial window, 70% of all imaged boutons appeared to be nonresponsive to visual stimuli and only 7% satisfied orientation-selective criteria; with a thinner cranial window of 170 μm, 31% of boutons were found to satisfy orientation-selective criteria. After AO correction, 48% of boutons were found to satisfy orientation-selective criteria when the same boutons were imaged. Between the latter two conditions, correcting aberrations sharpens the orientation tuning curves and leads to an overall shift in the global orientation selectivity index (gOSI) distribution toward higher selectivity, more accurately reflecting the tuning properties of these synaptic inputs.

## High-Speed *In Vivo* Imaging of the Brain with Bessel Focus Scanning

Because circuits and neurons are 3D structures that can extend over hundreds or thousands of micrometers, understanding their operations requires monitoring their activity at synaptic and cellular resolution in 3D at image rates that capture all activity events. In brains that strongly scatter light (e.g., adult brains), 2PFM is the only optical imaging method that provides submicrometer spatial resolution for imaging synapses and subsecond temporal resolution for capturing calcium events associated with action potentials. The most common applications of 2PFM involve scanning an excitation focus within a 2D plane while recording the fluorescence signals of GECIs, which provide information on both neuronal morphology and activity in this plane. The AO methods reviewed above allow 2PFM to achieve high-resolution images of the brain at depth. For volumetric imaging, however, conventional two-photon fluorescence microscopes step the microscope objective or the sample in $z$ to obtain 3D image stacks. There, the limited brightness of calcium indicators and the inertia of laser scanning units lead to low volume rates and preclude the study of activity synchrony in neurons distributed in a volume.

Recently, a volumetric imaging approach was developed based on Bessel focus scanning technology (Lu et al., 2017). For most *in vivo* brain imaging experiments, the positions of neurons and their synapses remain unchanged during each imaging session; thus, they rarely need to be constantly monitored and tracked in 3D. Therefore, volume imaging speed can be increased substantially by sacrificing axial resolution. Scanning an axially elongated Bessel focus in 2D (Fig. 5*a*) creates projected views of 3D volumes (Welford, 1960), leading to ten- to hundredfold increases in imaging throughput and reductions in total data size.

In Figure 5*b*, the volume imaging module is composed of a phase-only SLM and an annular mask array and incorporated into a two-photon microscope by placing it between the excitation laser and the microscope. A concentric binary phase pattern on the SLM generates a ring illumination at the focal plane of lens L1. After spatial filtering with an annular mask, the ring pattern is imaged onto the galvanometer scanners by lenses L2 and L3. This leads to an annular illumination on the back pupil plane of the microscope objective and an axially extended focus approximating a Bessel beam. With different phase patterns on the SLM, the Bessel module can generate foci extending 20–400 μm axially.

In one example that demonstrated the speed and resolution of Bessel volume scanning, sparse GCaMP6s$^+$ neurites were imaged in the primary visual cortex of awake mice. With a Gaussian focus (NA 1.05; axial FWHM [full-width at half maximum] 1.4 μm), conventional 3D scanning required at least 36 2D frames to cover all spines with a volume extending 60 μm in $z$ (upper panel, 60 frames, Fig. 5*c*). In contrast, scanning with a Bessel focus (NA 0.4; axial FWHM 53 μm) in 2D

NOTES

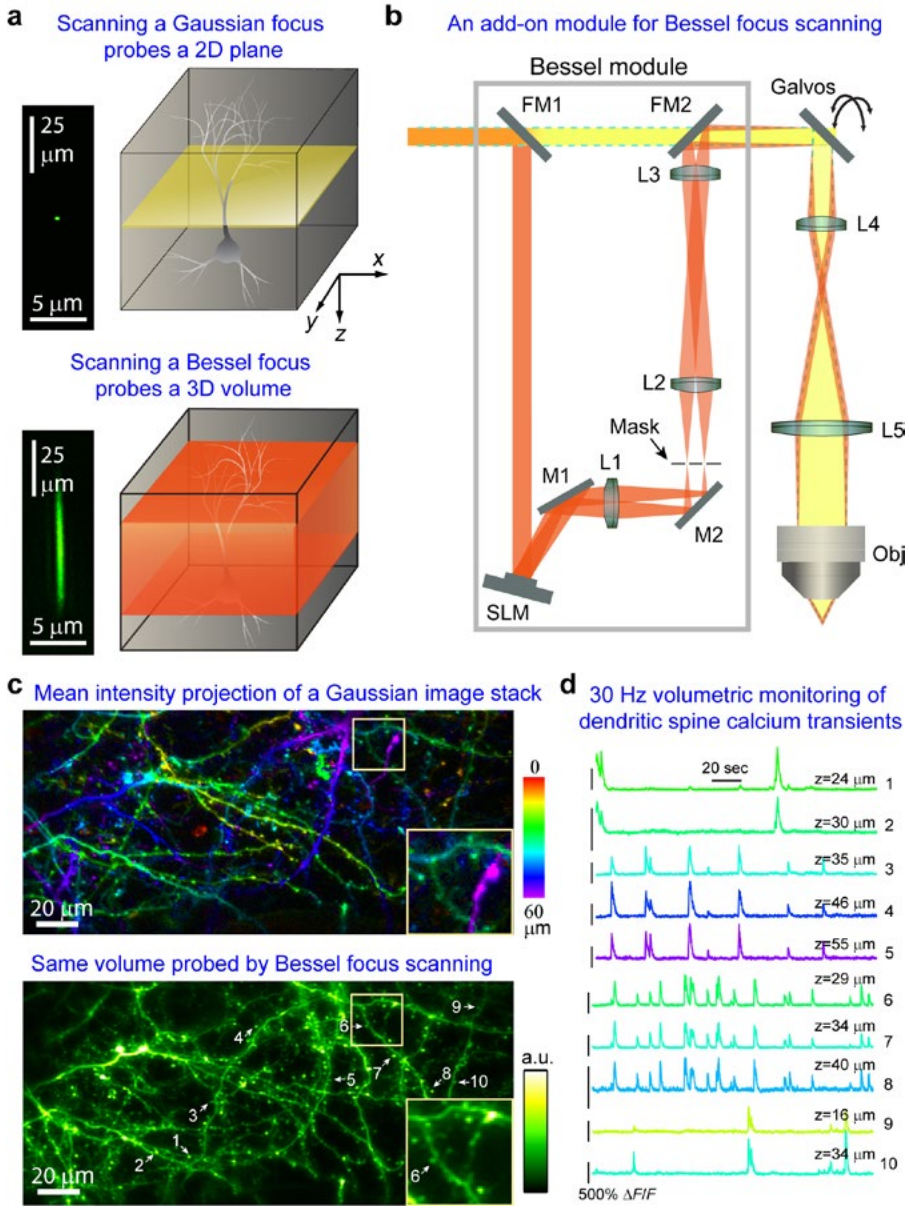


**Figure 5.** Concept, design, and *in vivo* performance of Bessel focus scanning method. ***a***, Top, Scanning a Gaussian focus images a thin section. Bottom, Scanning an axially elongated Bessel focus probes a volume. Left panels, axial images of Gaussian and Bessel foci. ***b***, A Bessel module composed of an SLM, lenses L1-3, and an annular mask. FMs, flip mirrors to switch between Gaussian and Bessel modes. ***c***, Top, Mean intensity projection of a 60-μm-thick image stack (color-coded by depth). Bottom, Same structures imaged at 30 Hz by scanning a Bessel focus. Insets: zoomed-in views of spines. ***d***, Calcium transients measured in volumes of GCaMP6s$^+$ boutons and spines measured at 30 Hz. Scale bars: ***a***, Vertical, 25 μm; horizontal, 5 μm; ***c***, 20 μm. Reprinted with permission from Lu et al. (2017), Fig. 1. Copyright 2017, Springer Nature.

captured all the structures in one frame, reducing the data size by ~60-fold (lower panel, Fig. 5*c*). Using a two-photon fluorescence microscope with a resonant galvo, visually evoked calcium transients in axonal varicosities and dendritic spines within a 270 μm × 270 μm × 60 μm volume were measured at 30 Hz (Fig. 5*d*). Importantly, with Bessel scanning, the gain in volume imaging speed does not come at the cost of a reduction in lateral resolution; here the synapses (arrows in Fig. 5*c*) are clearly resolvable. Using Bessel foci optimized for *in vivo* imaging of fly, zebrafish, mouse, and ferret brains, 30 Hz volumetric calcium imaging with synaptic resolution was demonstrated *in vivo*. The extended axial range of Bessel foci also makes the imaging insensitive to axial brain motion, making it uniquely suitable for *in vivo* brain imaging of behaving animals.

NOTES

## Conclusion

In conclusion, we reviewed recent works on *in vivo* imaging of the brain. All these studies have a common theme: by controlling the wavefront of the light used for image formation, one can achieve high-resolution, high-speed imaging for neurobiological inquiries.

## Acknowledgments

This chapter was adapted with permission from two previously published articles: Rodríguez and Ji (2018) Adaptive optical microscopy for neurobiology. Curr Opin Neurobiol 6:83–91, copyright 2018, Elsevier; and Lu et al. (2017) Video-rate volumetric functional imaging of the brain at synaptic resolution. Nat Neurosci 20:620–628, copyright 2017, Springer Nature.

## References

Booth MJ (2006) Wave front sensor-less adaptive optics: a model-based approach using sphere packings. Opt Express 14:1339–1352.

Booth MJ (2014) Adaptive optical microscopy: the ongoing quest for a perfect image. Light Sci Appl 3:e165.

Booth MJ, Andrade D, Burke D, Patton B, Zarauskas M (2015) Aberrations and adaptive optics in super-resolution microscopy. Microscopy 64:251–261.

Cajal SR (2002) Texture of the nervous system of man and the vertebrates, Vol III (Pasik P, Pasik T, eds). New York: Springer.

Chen TW, Wardill TJ, Sun Y, Pulver SR, Renninger SL, Baohan A, Schreiter ER, Kerr RA, Orger MB, Jayaraman V, Looger LL, Svoboda K, Kim DS (2013) Ultrasensitive fluorescent proteins for imaging neuronal activity. Nature 499:295–300.

Dana H, Mohar B, Sun Y, Narayan S, Gordus A, Hasseman JP, Tsegaye G, Holt GT, Hu A, Walpita D, Patel R, Macklin JJ, Bargmann CI, Ahrens MB, Schreiter ER, Jayaraman V, Looger LL, Svoboda K, Kim DS (2016) Sensitive red protein calcium indicators for imaging neural activity. eLife 5:e12727.

Débarre D, Booth MJ, Wilson T (2007) Image based adaptive optics through optimisation of low spatial frequencies. Opt Express 15:8176–8190.

Galwaduge PT, Kim SH, Grosberg LE, Hillman EM (2015) Simple wavefront correction framework for two-photon microscopy of in-vivo brain. Biomed Opt Express 6:2997–3013.

Göbel W, Helmchen F (2007) *In vivo* calcium imaging of neural network function. Physiology (Bethesda) 22:358–365.

Horton NG, Wang K, Kobat D, Clark CG, Wise FW, Schaffer CB, Xu C (2013) *In vivo* three-photon microscopy of subcortical structures within an intact mouse brain. Nat Photonics 7:205–209.

Ji N, Milkie DE, Betzig E (2010) Adaptive optics via pupil segmentation for high-resolution imaging in biological tissues. Nat Methods 7:141–147.

Ji N, Sato TR, Betzig E (2012) Characterization and adaptive optical correction of aberrations during *in vivo* imaging in the mouse cortex. Proc Natl Acad Sci USA 109:22–27.

Ji N (2017) Adaptive optical fluorescence microscopy. Nat Methods 14:374–380.

Kondo M, Kobayashi K, Ohkura M, Nakai J, Matsuzaki M (2017) Two-photon calcium imaging of the medial prefrontal cortex and hippocampus without cortical invasion. eLife 6:e26839.

Kubby JA (2013) Adaptive optics for biological imaging. Boca Raton: CRC Press.

Liu R, Milkie DE, Kerlin A, MacLennan B, Ji N (2014) Direct phase measurement in zonal wavefront reconstruction using multidither coherent optical adaptive technique. Opt Express 22:1619–1628.

Lu R, Sun W, Liang Y, Kerlin A, Bierfeld J, Seelig JD, Wilson DE, Scholl B, Mohar B, Tanimoto M, Koyama M, Fitzpatrick D, Orger MB, Ji N (2017). Video-rate volumetric functional imaging of the brain at synaptic resolution. Nat Neurosci 20:620–628.

Milkie DE, Betzig E, Ji N (2011) Pupil-segmentation-based adaptive optical microscopy with full-pupil illumination. Opt Lett 36:4206–4208.

Ouzounov DG, Wang T, Wang M, Feng DD, Horton NG, Cruz-Hernández JC, Cheng YT, Reimer J, Tolias AS, Nishimura N, Xu C (2017) *In vivo* three-photon imaging of activity of GCaMP6-labeled neurons deep in intact mouse brain. Nat Methods 14:388–390.

Papadopoulos IN, J.-S. B. Jouhanneau, J. F. A. Poulet, and B. Judkewitz (2017) Scattering compensation by focus scanning holographic aberration probing (F-SHARP). Nat Photonics 11:116–123.

Park JH, Kong L, Zhou Y, Cui M (2017) Large-field-of-view imaging by multi-pupil adaptive optics. Nat Methods 14:581–583.

Rodríguez C, Ji N (2018) Adaptive optical microscopy for neurobiology. Curr Opin Neurobiol 6:83–91.

NOTES

Schwertner M, Booth MJ, Neil MA, Wilson T (2004a) Measurement of specimen-induced aberrations of biological samples using phase stepping interferometry. J Microsc 213:11–19.

Schwertner M, Booth M, Wilson T (2004b) Characterizing specimen induced aberrations for high NA adaptive optical microscopy. Opt Express 12:6540–6552.

Sinefeld D, Paudel HP, Ouzounov DG, Bifano TG, Xu C (2015) Adaptive optics in multiphoton microscopy: comparison of two, three and four photon fluorescence. Opt Express 23:31472–31483.

Southwell WH (1980) Wave-front estimation from wave-front slope measurements. J Opt Soc Am 70:998–1006.

Sun W, Tan Z, Mensh BD, Ji N (2016) Thalamus provides layer 4 of primary visual cortex with orientation- and direction-tuned inputs. Nat Neurosci 19:308–315.

Tao X, Lin HH, Lam T, Rodriguez R, Wang JW, Kubby J (2017) Transcutical imaging with cellular and subcellular resolution. Biomed Opt Express 8:1277–1289.

Theer P, Hasan MT, Denk W (2003) Two-photon imaging to a depth of 1000 μm in living brains by use of a $Ti:Al_2O_3$ regenerative amplifier. Opt Lett 28:1022–1024.

Wang C, Ji N (2012) Pupil-segmentation-based adaptive optical correction of a high-numerical-aperture gradient refractive index lens for two-photon fluorescence endoscopy. Opt Lett 37:2001–2003.

Wang C, Ji N (2013) Characterization and improvement of three-dimensional imaging performance of GRIN-lens-based two-photon fluorescence endomicroscopes with adaptive optics. Opt Express 21:27142–27154.

Wang C, Liu R, Milkie DE, Sun W, Tan Z, Kerlin A, Chen TW, Kim DS, Ji N (2014b) Multiplexed aberration measurement for deep tissue imaging *in vivo*. Nat Methods 11:1037–1040.

Wang K, Milkie DE, Saxena A, Engerer P, Misgeld T, Bronner ME, Mumm J, Betzig E (2014a) Rapid adaptive optical recovery of optimal resolution over large volumes. Nat Methods 11:625–628.

Wang K, Sun W, Richie CT, Harvey BK, Betzig E, Ji N (2015) Direct wavefront sensing for high-resolution *in vivo* imaging in scattering tissue. Nat Commun 6:7276.

Welford WT (1960) Use of annular apertures to increase focal depth. J Opt Soc Am 50:749–753.

Yang W, Yuste R (2017) *In vivo* imaging of neural activity. Nat Methods 14:349–359.

Zeng J, Mahou P, Schanne-Klein MC, Beaurepaire E, Débarre D (2012) 3D resolved mapping of optical aberrations in thick tissues. Biomed Opt Express 3:1898–1913.

# What Is Connectome Coding?

Eric W. Bridgeford, BS,[1] Daniel Sussman, PhD,[6] Vince Lyzinski, PhD,[7] Yichen Qin, PhD,[8] Youngser Park, PhD,[2] Brian Caffo, PhD,[3] Carey E. Priebe, PhD,[4] and Joshua T. Vogelstein, PhD[5]

[1]Department of Biostatistics

[2]Center for Imaging Science
Institute for Computational Medicine

[3]Department of Biostatistics

[4]Department of Applied Mathematics and Statistics
Whiting School of Engineering

[5]Department of Biomedical Engineering
Institute for Computational Medicine
Johns Hopkins University
Baltimore, Maryland

[6]Department of Mathematics and Statistics
Boston University
Boston, Massachusetts

[7]Department of Mathematics and Statistics
University of Massachusetts, Amherst
Amherst, Massachusetts

[8]Department of Statistics
University of Cincinnati
Cincinnati, Ohio

NOTES

## Introduction

In this chapter, we propose a quantitative modeling framework to characterize and explain certain aspects of brain structure. Any quantitative modeling framework either implicitly or explicitly rests on a conceptual model. Although our conceptual model is not entirely novel, making it explicit reveals certain inadequacies of the existing neuroscience modeling frameworks and tools, thereby motivating the development of the strategy proposed below.

In our conceptual model, there are three "levels" of physical objects: a brain, a body, and a world (Fig. 1). Each level exhibits both internal dynamics and interactions across levels. These interactions occur across many orders of magnitude of both space and time. Our main interest is in modeling the brain, and in particular, brain structure, as will be seen below.

Starting from the outer level, the world governs the outcomes of the ongoing evolutionary "games" within various ecological niches. In these games, the brain and body must conspire to behave in ways that outcompete other brains and bodies for shared, limited resources. The body is the source of motor control as well as sensory input to the brain. It is therefore the required interface between the brain and the world. The brain is further divided into structure (e.g., neurons and glia) and activity (e.g., dynamics of ions, neurotransmitters, and second messengers).

From this perspective, it is clear that brain structure plays an integral role in brain activity, motor control, behavior, and eventually, the outcomes of evolutionary pressures (Cajal, 1995). In particular, brain structure governs motor sequences in a variety of ways. For example, a particular brain structure controls the suppressive hierarchy among competing motor programs that drives sequential grooming in *Drosophila* (Seeds, 2014). Similarly, the interscutularis neuromuscular circuit controls the mouse's ear movements (Lu, 2009). In both cases, the brain structure must provide a foundation, as well as a set of constraints and biases, that guides brain activity. Thus, "understanding" the mechanism of those behaviors requires a model of brain structure.

That a model of brain structure is required to explain the brain's output motivates the search for a model that explains brain structure itself. Brain structure is guided by two components. The first comprises developmental programs, which are encoded in the genome (Purves and Lichtman, 1985). Of course, the genome is partially determined by selective pressures imposed on previous generations in which some of the individuals were able to propagate their genes by choosing specific behaviors (and luck) (Tomasetti and Vogelstein, 2015). The second is activity-dependent plasticity, which is encoded in the rules governing, for example, spike-timing-dependent plasticity (Dan and Poo, 2006). Development and activity-

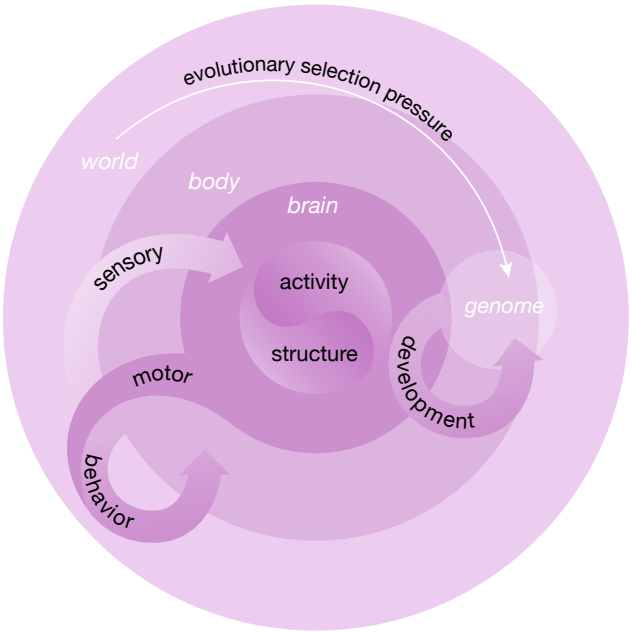


**Figure 1.** The connectome code is a model characterizing how information from brain activity and the genome is represented in the brain by connections between morphological objects (the connectome).

NOTES

dependent plasticity are not fully independent; rather, much of development (and degeneration) is gated or guided by activity, for example, the onset of critical periods (Scott, 1962).

## Connectomics

### What is a connectome?

A connectome is typically defined as a network, the "$\boldsymbol{W}_{ij}$" of the brain of the brain (Hagmann, 2005; Sporns et al., 2005). Recall that in graph theory, a network consists of a set of nodes and edges connecting them. In such a network, there is no physical space, no location, no connection strength, etc. Thus, as defined by graph theory, a network is a bit limiting and overly simplistic for the kinds of analysis and models that people are using to study connectomics. Here, we introduce a more general definition of a connectome, which includes (potentially multiscale) structural attributes, many of which are implicitly included in previous notions of a connectome.

Any brain network consists of nodes (also called vertices or actors) and edges (also called links or arcs). In brain networks, however, nodes are always spatially contiguous morphological objects whose extent and shape are determined by the spatiotemporal resolution of the experimental modality providing connectome data. For example, in nanoscale electron microscopy data, the nodes are typically individual neurons, whereas in macroscale magnetic resonance imaging (MRI) data, nodes may be defined by sulcul and gyral delineations. Thus, these nodes always have attributes, including absolute location in the brain. They often include relative position in a template brain, an associated shape, thickness for cortical areas, and branching morphology, and frequently have an associated hierarchical ontology of neuron types (Hodge et al., 2018) or regions (Mai et al., 2007; Hagmann et al., 2008). Similarly, the edges in nanoscale data can be either chemical or electrical synapses, whereas edges in macroscale data can be defined by correlations over brief epochs of time or large bundles of axons. As a result, these edges have a number of attributes, potentially including strength, size, sign, and more. Therefore, to answer the questions of interest requires a generalized notion of a network or graph, one that includes potentially complex vertex and edge attributes. In summary, we characterize the entirety of the brain structure at a particular scale as the "connectome"' of that region.

### Why connectome coding?

Interest in studying the neural code is well established despite widespread disagreement about whether there is a single neural code, multiple codes, or one code per problem per species, etc. On the other hand, whether a connectome code is valuable is hotly debated. Here we outline a few basic reasons that connectome codes are not just valuable, but actually required for a complete understanding of brain function and dysfunction:

- It is widely conjectured that information in the brain is stored in neural circuits, also called the "memory engram" (Zhang and Linden, 2003). To the extent that this is true, our ability to understand and "read" memories will depend on the depth of our understanding of the statistics of these circuits.
- Another relatively widely held belief is that psychiatric illnesses are disorders of neural circuitry, or connectopathies (Castellanos et al., 2013; Van Dam et al., 2017; Braun et al., 2018; Elliott et al., 2018; Powell et al., 2018; Spronk et al., 2018). Thus, our ability to develop clinically useful prognostic, diagnostic, and treatment protocols will also depend on our understanding of neural circuitry. In both cases, it remains an open question as to the required "precision" of the connectome code. For example, the degree to which a connectome code (at the level of neuron, cell type, or region of interest) will be useful for clinical practice remains an open empirical question.
- Neural activity depends on neural connectivity (Mill et al., 2017). The requisite additional information to create a sufficiently biofidelic simulation of a brain continues to be debated, but all simulations use some connectomic information (Markram et al., 2015).
- Finally, in the human brain, there are approximately $10^{11}$ neurons (Herculano-Houzel, 2009) and $10^{15}$ connections between pairs of neurons, and yet we have only ~$3 \times 10^4$ genes (Ezkurdia et al., 2014). This means that the genome must genetically encode the "blueprint" of the brain, that is, a number of statistical rules governing the probability of synapses between regions throughout development, as well as all the rules for learning new connections due to environmental exposures. Thus, evolution must have learned a connectome code for humans, one that we should be able to learn from data.

The above arguments motivate building statistical models for connectome coding, but why can we not simply use the models already developed for neural coding? There are two key differences between connectome coding and neural coding that make connectome coding substantially more difficult. First, a spike can reasonably be modeled as a function of only

NOTES

a single neuron, whereas an edge is fundamentally a function of two nodes. This complicates matters because even the simplest models become bilinear (linear in both nodes) versus linear (linear in one node). Bilinearity increases the difficulty of estimating parameters, both computationally and statistically. Second, spikes are fundamentally binary operations: a spiking neuron either spikes or does not, to convey information to downstream neurons. However, connections between nodes are not binary. Even individual synapses can vary dramatically in volume and the maximum magnitude of an average evoked potential. Estimated connectomes are also typically weighted, whether they correspond to estimates of the functional or structural relationship between the nodes. Connectomists are therefore faced with a decision: either choose a mechanism for converting weighted networks into binary networks, or develop models for weighted networks. In either case, this is an additional step not required of those modeling spike trains.

## Example connectomes

Next we describe several different estimates of connectomes spanning the phylogenetic tree and spatiotemporal scales. We will use these connectomes as working examples to illustrate the power and flexibility of our proposed connectome coding framework.

### *Caenorhabditis elegans*

*Caenorhabditis elegans* is the only animal for which we have a complete, neuron-to-neuron level connectome. In the *C. elegans* connectome, edges are either chemical synapses (which are directed) or gap junctions (which are bidirectional or "undirected"). Each edge's strength or weight corresponds to the number of synapses between its parent neurons. There are two sexes of *C. elegans*, the male and the hermaphrodite, with different numbers of neurons (the male has more, although most of the neurons are shared between the two sexes, but not all). Thus, each sex has a weighted, partially directed multiconnectome. These connectome estimates are derived by cumbersome manual tracing of axons and dendrites, and identification of synapses, in nanoscale electron micrographs (White et al., 1986) and were updated by Varshney et al. (2011) and Bentley et al. (2016). The neurons are often divided into three classes: sensory (S), internal (I), and motor (M), most of which are bilaterally symmetric, although not all the motor neurons have lateral counterparts (Fig. 2*A*).

### *Drosophila*

Eichler et al. (2017) performed one of the most recent and comprehensive characterizations of a connectome. They published a complete larval *Drosophila* connectome of the mushroom body, also derived from serial electron microscopy, using only chemical synapses, making this connectome weighted and directed. They estimated connectivity from both the left and right mushroom body. Neurons are categorized into Kenyon cells (K), input neurons (I), output neurons (O), and projection neurons (P) (Fig. 2*B*).

### *Mouse connectivity atlas*

Calabrese et al. (2015) generated a high-resolution connectivity atlas using *ex vivo* diffusion MRI (dMRI). This network is undirected, as dMRI lacks directional information, and weights correspond to the number of tracts estimated to go from one region to another. Regions in the mouse connectome can be partitioned into "superstructures," including frontal (F), hindbrain (H), midbrain (M), and white matter (W) (Fig. 2*C*).

### *Human connectomes*

The Consortium for Reliability and Reproducibility (Zuo et al., 2014) collects multiple measurements of anatomical, resting-state, and/or dMRI per individual. They analyze the multiconnectomes, including functional MRI (fMRI)–derived and dMRI-derived estimates, by averaging the entire dataset consisting of 3067 dMRI and 1760 fMRI connectomes. The work of Kiar et al. (2018) provides the largest open-access repository of human connectomes. Additionally, average per-gender dMRI connectomes are estimated from 612 female subjects and 613 male subjects. Of the many possible brain parcellations (Glasser et al., 2016), we elected to use the Desikan parcellation (Desikan et al., 2006), assigning each cortical region into lobes, including frontal (F), occipital (O), parietal (P), and temporal (T), as well as subcortical structures (S) (Fig. 2*D*).

## Proposed connectome coding framework

Adopting notation typical of neural coding, let $s$ denote a realized stimulus and $r$ denote the realized response. We model both the stimulus and the response as random variables, denoted $\boldsymbol{S}$ and $\boldsymbol{R}$, respectively. The neural encoding problem is to estimate the conditional distribution of a neural response given the stimulus, $F_{R|S}$, whereas the neural decoding problem is to estimate the distribution

NOTES

of the stimulus given a response, $F_{S|R}$ . The joint distribution of the response and the stimulus can be written in terms of either conditional distribution, using Bayes' rule:

$$F_{R,S} = F_{R|S} \times F_S = F_{S|R} \times F_R. \quad (1)$$

For connectome coding, we need to define some additional concepts and notation. Denoting a network by $\mathcal{G} = (\boldsymbol{V}, \mathcal{E})$, where $\boldsymbol{V}$ is the set of nodes, and $\mathcal{E}$ is the set of edges, the number of nodes is $n = |\boldsymbol{V}|$. Throughout, we will refer to the "nodes," which might represent neurons or regions of interest, as appropriate. We can represent a network by an $n \times n$

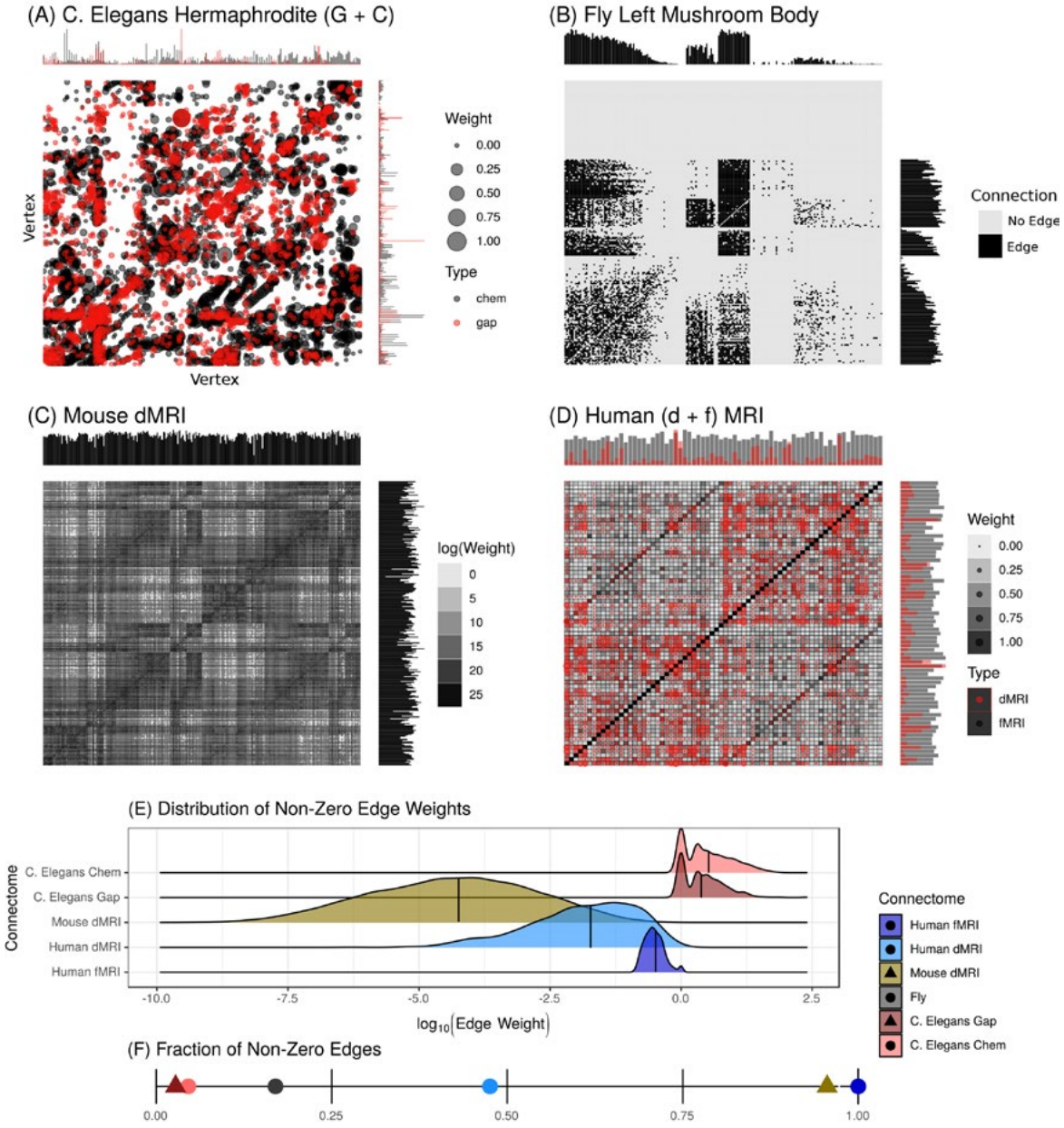


**Figure 2.** ***A–D,*** Connectomes spanning four levels of the phylogenetic tree, each acquired using different experimental modalities and spatial resolutions, ranging from nanoscale (electron microscopy) to macroscale (MRI regions). In each case, the connectomes are depicted as weighted adjacency matrices; for *C. elegans* and the human, the connectomes are multiconnectomes with two different edge types denoted by two different colors. In each case, the vertices are sorted by region. Moreover, along each connectome, we provide the degree sequence, that is, the "degree centrality" for each node and modality (Zuo et al., 2012). G + C, gap and chemical. ***E***, Density estimates of the non-zero edge weights per connectome. The annotated line on each density estimate indicates the average non-zero edge weight. The fly mushroom body (a binary graph) is not shown, as all non-zero edges have weight 1. ***F,*** The fraction of edges per connectome that are non-zero. The connectomes display sizable disparities in both non-zero edge weight and fraction of non-zero edges.

NOTES

adjacency matrix, $A$. If G + C, gap and chemical. the connectome is binary (meaning having no weights on edges), then the existence of an edge between node $u$ and node $v$ is indicated by $A(u, v) = 1$; otherwise, $A(u, v) = 0$. If the connectome is weighted, then $A(u, v)$ can take any real value. If the connectome allows for self-connections (also called self-loops), then it is possible that $A(u, u) = 1$ for any $u$, but otherwise not. If the connectome is undirected, then $A(u, v) = A(v, u)$ for all $(u, v)$ pairs. The total number of possible edges, $n_e$ , depends on whether the network is directed and whether it allows for self-loops. If both, then $n_e = n^2$. If neither is allowed, then $n_e = \binom{n}{2}$. We will see examples of weighted and unweighted, directed and undirected networks, both with and without loops.

To build statistical models of connectomes and connectome code requires introducing the concept of random variables, as in neural coding. Let $\mathbf{A}$ denote a random adjacency matrix (which is akin to the response in neural coding), and let $\boldsymbol{X}$ be the random variable whose values denote some properties of the genome, body, and/or world. Then we can write the joint distribution of the connectome and other stuff as:

$$F_{A,X} = F_{A|X} \times F_X = F_{X|A} \times F_A. \quad (2)$$

For simplicity, this chapter will focus on the connectome encoding problem, that is, determining $F_{A|X}$ , which requires a previous model $F_A$ to build on. In a connectome with $n$ nodes and $n_2$ potential binary edges, there are $2^{n^2}$ possible different connectomes. Note that this means that the number of possible connectomes grows at a super-exponential rate. For example, when $n = 10$, $2^{n^2} = 10^{30}$, and when $n = 30$, $2^{n^2} = 10^{280}$! This is in contrast to the number of seconds since the big bang ($\approx 10^{20}$), the number of molecules in the universe ($\approx 10^{80}$), the number of possible chess games ($\approx 10^{120}$), and the number of possible Go games on a 19 × 19 board ($\approx 10^{170}$). Because connectomes are fundamentally categorical objects, without further assumptions, the "nonparametric" connectome model would be that $\mathbf{A} \sim F(\boldsymbol{\theta})$, where $F$ is a categorical distribution with parameter

$$\boldsymbol{\theta} = (\boldsymbol{\theta}_1, \ldots, \boldsymbol{\theta}_{2^{n^2}}).$$

Clearly, two parameters are far too many to be able to estimate with reasonable sample sizes, even for the smallest connectomes. Thus, connectome coding requires making a number of simplifying assumptions to enable empirically useful estimates. Below we describe several increasingly complex models of connectomes. For each, we introduce the corresponding neural code.

## Edge Models

### Independent edge models

The simplest statistical model characterizing neural spiking activity is a Poisson (point) process. Under a Poisson process, spiking events are independent of one another and have a fixed rate. By analogy, the simplest connectome model is the Erdös–Rényi (**ER**) random graph model. The **ER** model posits that the probability of an edge anywhere in the graph is independent of all other edges and everything else (Erdös and Rényi, 1959). This model is clearly too simple to provide an interesting representation of brain networks. The simplest and slightest generalization of the **ER** model is a weighted **ER** (**WER**) model. We assume here a slightly different **WER** model from those previously proposed (Garlaschelli, 2009); specifically, our **WER** model is model-free: we specify only the average weight per connection. Whereas the **WER** model yields the simplest connectome code for dense, weighted connectomes, many connectome estimates are sparse (including a large number of zeros), and the non-zeros are not all equal to one another. In this case, a "zero-inflated **WER**" (**ZWER**) model is the simplest choice (Tang et al., 2017a). This model is a mixture of an **ER** model and a **WER** model, with a parameter governing the probability that the edge has a non-zero weight. For each of the above described connectomes, the maximum likelihood estimator (MLE) is readily available in closed form for both the probability of an edge and the average weight of edges. Figures 2*E* and 2*F* show these parameters for each of the above described connectomes. The **ZWER** is a "first order" (1°) connectome model.

### Conditionally independent edge models

Independent spike/edge models are not sufficient to characterize the variability of neural activity or connectivity. Thus, the next simplest model is a conditional model, where the probability of a spike or edge is a function of something else. In the neural coding case, for simplicity, assume there are several possible stimuli (e.g., moving bars in one of eight possible directions), and the firing rate of a given visual neuron is a function of the direction. The analogous conditionally independent, random graph model for connectomes is the stochastic block model (**SBM**) (Holland et al., 1983). In an **SBM**, each node has a "type," and the probability of an edge between a pair of nodes is dictated by the type of each node. This is akin to the situation described earlier, where the probability of a spike is conditioned on the stimulus; here, the "stimulus" corresponds to "node type," which could indicate excitatory versus inhibitory,

NOTES

cortical layer, gyral region, hemisphere, etc. In our estimated connectomes, the edges have weights that can vary by orders of magnitude. Thus, if we were to naively estimate the average weight, the large-magnitude weights would dominate. In practice, we therefore consider two common transformations. For the C. *elegans* and human connectomes, we "pass-to-ranks" (Wang et al., 2015; Tang et al., 2017b), which converts the magnitudes to their relative order and is a standard tactic in robust statistics (Huber and Ronchetti, 1981). For the mouse connectome, we log-transform the weights after adding one to reduce the heavy log-linear tail of the edge distribution (Tang et al., 2016). Both of these are special cases of a weighted **SBM** (**WSBM**). The parameters for the **WSBM** are also available in closed form. Figure 3 shows several different examples of estimated **WSBM**s. The assumed block structure follows from the neuron types and hierarchical parcellation schemes described in "Example connectomes," above. The **WSBM** is a 2° connectome model.

## Latent variable models

In the above models, the probability of an "event" (either a spike or an edge) is conditionally dependent on some observed variable. It is also possible to model these events as conditionally dependent on latent variables. In neural coding, it has recently become popular to use latent variable models to characterize an ensemble of neural activities (Cunningham and Yu, 2014). In connectome coding, latent variable models assume a latent variable per node. The simplest variant is the *a posteriori* **SBM**, which is the same as the **SBM** except that the $X$s are not observed; rather, they must be estimated (Wasserman and Anderson, 1987). A generalization of this model is the "latent position model" in which $X$s are no longer categorical, but rather continuous and potentially multivariate (Hoff et al., 2002). A particularly prominent special case of the latent position model is the "random dot product model" (**RDPM**) (Young and Scheinerman, 2007; Scheinerman and Tucker, 2009). We define the weighted **RDPM** much like the weighted **SBM** (Tang et al., 2017a). While technically, one can obtain the MLE for the RDPM, doing so is rather computationally taxing (Bickel et al., 2013). Instead, it turns out that computing an eigendecomposition of the adjacency (or Laplacian) matrix of the connectome yields a consistent estimate of the latent positions under the **RDPM** with modest additional assumptions (up to an irrelevant rotation) (Rohe et al., 2011; Sussman et al., 2011). Figure 4 shows this "adjacency spectral embedding" approach to estimating the latent position on the six example

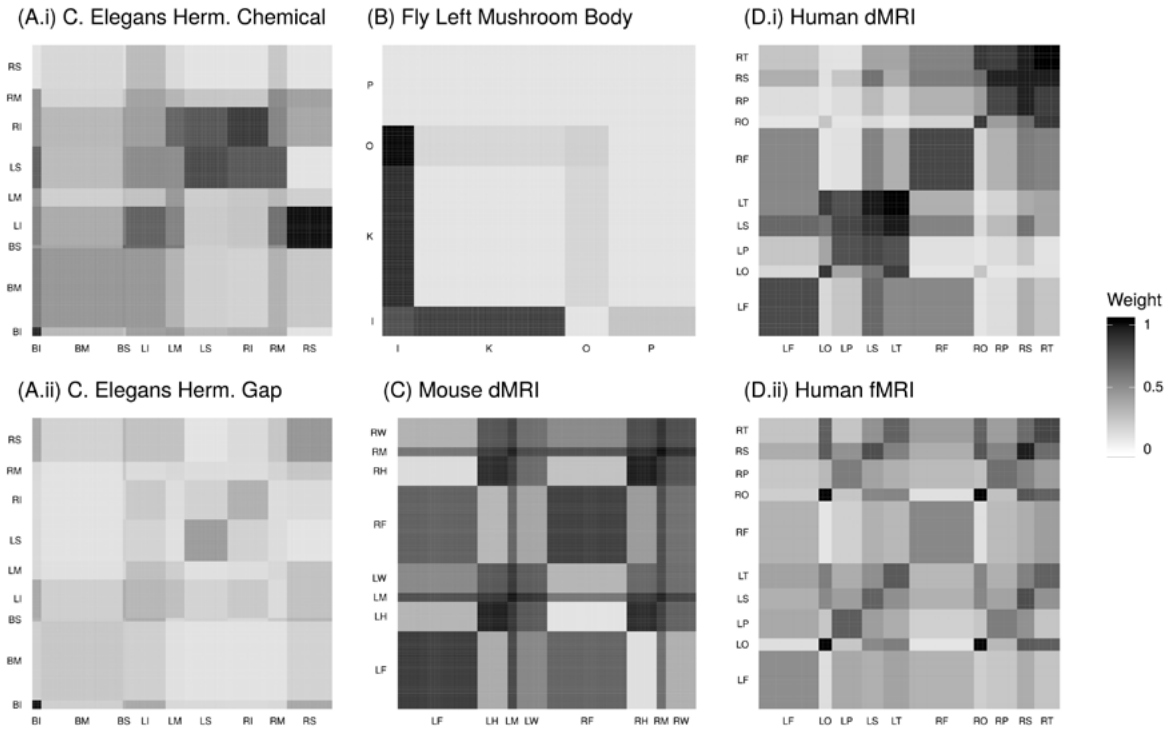


**Figure 3.** **WSBM** estimates of the six connectomes depicted in Figure 2, indicating the average edge weight between communities of vertices.

NOTES

connectomes. For each, the color and/or symbol corresponds to a true latent category. It is evident from the plots that the latent positions correspond to these observed categories. The **WRDPM** is a 3° connectome model.

## Latent structure model

In neural coding, some of the latent variable models impose some structure on the data, such as refractory periods or smooth dynamical systems (Kass et al., 2014). Similarly, connectomes exhibit additional latent structure beyond mere "types." Consider, for example, Figure 4(*D*.i), human dMRI: each node in this connectome has both a hemispheric label as well as a lobe label. A model with multiple categorical labels is related to, but distinct from, the mixed membership **SBM** (Airoldi et al., 2008) and the generalized **RDPM** (Rubin-Delanchy et al., 2017). We therefore introduce the latent structure model (**LSM**) and the weighted **LSM** (**WLSM**), which can characterize many different latent structures. (See Priebe et al., 2017, and Athreya et al., 2018, for mathematical details; the latter describes the **LSM**s that impose parametric and geometric requirements on networks.) Figure 5 shows a concrete example wherein the **LSM** fits a quadratic one-dimensional manifold into a six-dimensional embedded space, to the positions of the Kenyon cells. It turns out that both the left and the right mushroom-body connectome exhibit the same latent structure. A third example of latent structure is hierarchical structure, such as the hierarchical **SBM**. Lyzinski et al. (2017) showed that the *Drosophila* medulla connectome exhibits a hierarchical structure, corresponding to the known anatomical structure of the medulla (Takemura et al., 2013, 2015, 2017). The **WLSM** is a 4° model of connectomes.

## Population models

In neural coding, population models typically refer to populations of neurons rather than populations of individuals (although not so in a human-brain imaging population). In connectome coding, however, population models correspond to at least

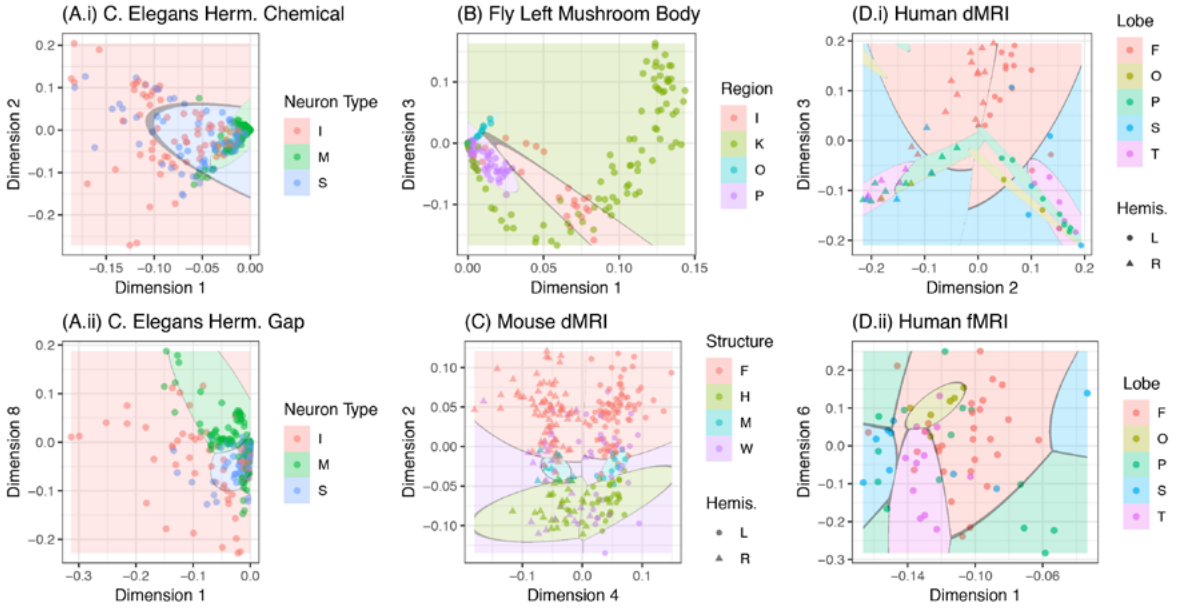


(E) Classifier Performance

| | (A.i) | (A.ii) | (B) | (C) | (D.i) | (D.ii) |
|---|---|---|---|---|---|---|
| *classifier accuracy* | .57 | .55 | .76 | .71 | .71 | .64 |
| *chance accuracy* | .39 | .39 | .48 | .26 | .21 | .41 |

**Figure 4.** Adjacency spectral embeddings of the six example connectomes. ***A–D***, Two-dimensional (2D) scatter plots where each cluster (as defined *a priori*) of nodes is fit with a Gaussian function, and the region of latent space where the likelihood is highest for a given Gaussian function is colored accordingly. ***E***, Fraction of nodes within their most likely region, compared with the fraction under a chance assignment that assigns each node to the most likely class. Note that the 2D embedding and Gaussian fit are significantly more accurate than chance for all connectomes. Neuron types in ***A***: I, internal; M, motor; S, sensory. Neuron types in ***B***: I, input neurons; K, Kenyon cells; O, output neurons; P, projection neurons. Regions in the mouse connectome partitioned into "superstructures" in ***C***: F, frontal; H, hindbrain; M, midbrain; W, white matter. Cortical region lobes in ***D***: F, frontal; O, occipital; P, parietal; T, temporal; S, subcortical structures.

NOTES

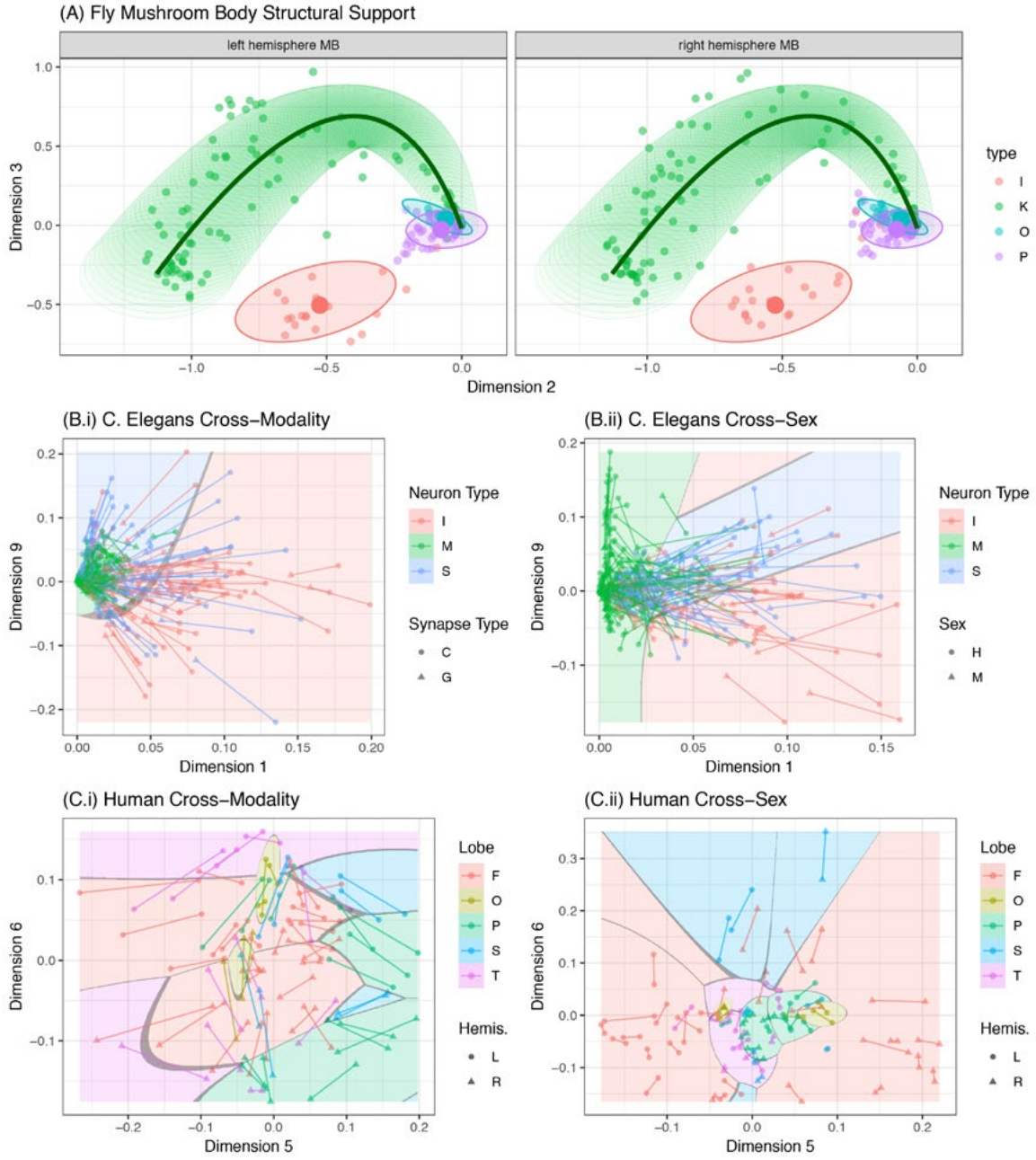


(D) Classifier Performance

| | (B.i) | (B.ii) | (C.i) | (C.ii) |
|---|---|---|---|---|
| *classifier accuracy* | .59 | .58 | .57 | .62 |
| *chance accuracy* | .39 | .39 | .21 | .21 |

**Figure 5.** ***A***, WLSMs; ***B–D***, Weighted MRDPM models. ***A***, A projection onto two dimensions of the six-dimensional estimated curve for the structural support of the Kenyon cell neurons and point masses for the other neuron types (all convolved with Gaussians). MB, mushroom body. Neuron types: I, input neurons; K, Kenyon cells; O, output neurons; P, projection neurons. ***B***, Joint embedding for *C. elegans*; and ***C***, humans. Shape and color indicate the node type, and the lines join vertices matched across sex or modality. Neuron types in ***B***: I, internal; M, motor; S, sensory. Cortical region lobes in ***C***: F, frontal; O, occipital; P, parietal; T, temporal; S, subcortical structures. ***D***, Fraction of nodes within their most likely region, compared with the fraction under a chance assignment that assigns each node to the most likely class.

NOTES

two connectomes. Several population models have recently been proposed, all of which are essentially mixtures of **RDPM**s (**MRDPM**) (Durante and Dunson, 2014; Durante et al., 2017; Levin et al., 2017; Wang et al., 2017; Rosenthal et al., 2018; Zhang et al., 2018) (Levin et al., 2017, describes the omnibus methodology for inference on populations of networks.) Two different strategies have been proposed for estimating the latent positions in these models: tensor factorization and "omnibus" embedding. In omnibus embedding, a joint matrix is constructed by placing the adjacency matrices of each connectome along the diagonal of an omnibus matrix, and augmenting the off-diagonal blocks with combinations of the original connectomes (a technique also used in multiview learning) (Lindenbaum et al., 2015). The result is that the connectomes are embedded together, and the correspondence between vertices in complementary connectomes can help reduce the variance of the estimates. Here again, theory asserts that the estimates should converge under reasonable assumptions. Figure 5 shows four examples that utilize this omnibus procedure. In each case, many corresponding nodes are in close proximity, thereby improving the clustering of various categories between graphs with disparate characteristics. The **MRDPG** is a 5° connectome model, explicitly designed for populations of connectomes.

## Conclusion

This chapter introduced and summarized the basic concepts and preliminary examples of connectome coding. An open-source R package containing all the functions required to estimate any of the models on network data is available at https://neurodata.io/ and https://github.com/neurodata/graphstats (Bridgeford et al., 2018).

Many gaps remain in our knowledge and capabilities with regard to connectome coding. Our intermediate goal is to continue to develop theory, methods, and applications for zero-inflated, weighted **LSM**s for individuals and populations, including statistically and computationally efficient estimation and hypothesis testing in these models (Tang et al., 2017c). Incorporating network, vertex, and edge attributes into these frameworks is yet another future direction. Connectome coding therefore presents a substantial opportunity for discovery in the brain sciences.

## Acknowledgments

The authors from Johns Hopkins University are grateful for support from the Defense Advanced Research Projects Agency's Simplifying Complexity in Scientific Discovery program through Space and Naval Warfare Systems Command contract N66001-15-C-4041.

## References

Airoldi EM, Blei DM, Fienberg SE, Xing EP (2008) Mixed membership stochastic blockmodels. J Mach Learn Res 9:1981–2014.

Athreya A, Tang M, Park Y, Priebe CE (2018) On estimation and inference in latent structure random graphs. arXiv: 1806.01401.

Bentley B, Branicky R, Barnes CL, Chew YL, Yemini E, Bullmore ET, Vértes PE, Schafer WR (2016) The multilayer connectome of *Caenorhabditis elegans*. PLoS Comput Biol 12:e1005283.

Bickel P, Choi D, Chang X, Zhang H (2013) Asymptotic normality of maximum likelihood and its variational approximation for stochastic blockmodels. Ann Stat 41:1922–1943.

Braun U, Schaefer A, Betzel RF, Tost H, Meyer-Lindenberg A, Bassett DS (2018) From maps to multi-dimensional network mechanisms of mental disorders. Neuron 97:14–31.

Bridgeford EW, Park Y, Mehta R, Zhang K, Vogelstein JT (2018) neurodata/graphstats: alpha 1. https://zenodo.org/record/1311965.

Cajal SR (1995) Histology of the nervous system of man and vertebrates, Vol 1. In: History of neuroscience, Vol 6, Ed 1. New York: Oxford University Press.

Calabrese E, Badea A, Cofer G, Qi Y, Johnson GA (2015) A diffusion MRI tractography connectome of the mouse brain and comparison with neuronal tracer data. Cereb Cortex 25:4628–4637.

Castellanos XF, Di Martino A, Craddock RC, Mehta AD, Milham MP (2013) Clinical applications of the functional connectome. Neuroimage 80:527–540.

Cunningham JP, Yu BM (2014) Dimensionality reduction for large-scale neural recordings. Nat Neurosci 17:1500–1509.

Dan Y, Poo MM (2006) Spike timing-dependent plasticity: from synapse to perception. Physiol Rev 86:1033–1048.

NOTES

Desikan RS, Ségonne F, Fischl B, Quinn BT, Dickerson BC, Blacker D, Buckner RL, Dale AM, Maguire RP, Hyman BT, Albert MS, Killiany RJ (2006) An automated labeling system for subdividing the human cerebral cortex on MRI scans into gyral based regions of interest. NeuroImage 31:968–980.

Durante D, Dunson DB (2014) Bayesian inference and testing of group differences in brain networks. arXiv:1411.6506.

Durante D, Dunson DB, Vogelstein JT (2017) Nonparametric Bayes modeling of populations of networks. J Am Stat Assoc 112:1516–1530.

Eichler K, Li F, Litwin-Kumar A, Park Y, Andrade I, Schneider-Mizell CM, Saumweber T, Huser A, Eschbach C, Gerber B, Fetter RD, Truman JW, Priebe CE, Abbott LF, Thum AS, Zlatic M, Cardona A (2017) The complete connectome of a learning and memory centre in an insect brain. Nature 548:175–182.

Elliott ML, Romer A, Knodt AR, Hariri AR (2018) A connectome-wide functional signature of transdiagnostic risk for mental illness. Biol Psychiatry 84:452–459.

Erdös P, Rényi A (1959) On random graphs I. Publicationes Mathematicae Debrecen 6:290–297.

Ezkurdia I, Juan D, Rodriguez JM, Frankish A, Diekhans M, Harrow J, Vazquez J, Valencia A, Tress ML (2014) Multiple evidence strands suggest that there may be as few as 19,000 human protein-coding genes. Hum Mol Genet 23:5866–5878.

Garlaschelli D (2009) The weighted random graph model. New J Phys 11:073005.

Glasser MF, Coalson TS, Robinson EC, Hacker CD, Harwell J, Yacoub E, Ugurbil K, Andersson J, Beckmann CF, Jenkinson M, Smith SM, Van Essen DC (2016) A multi-modal parcellation of human cerebral cortex. Nature 536:171–178.

Hagmann P (2005) From diffusion MRI to brain connectomics. PhD Thesis, École Polytechnique Fédérale de Lausanne, Lausanne, France.

Hagmann P, Cammoun L, Gigandet X, Meuli R, Honey CJ, Wedeen VJ, Sporns O (2008) Mapping the structural core of human cerebral cortex. PLoS Biol 6:e159.

Herculano-Houzel S (2009) The human brain in numbers: a linearly scaled-up primate brain. Front Hum Neurosci 3:31.

Hodge RD, Bakken TE, Miller JA, Smith KA, Barkan ER, Graybuck LT, Close JL, Long B, Penn O, Yao Z, Eggermont J, Hollt T, Levi BP, Shehata SI, Aevermann B, Bertagnolli D, Brouner K, Casper T, Cobbs C, Dalley R, et al. (2018) Conserved cell types with divergent features between human and mouse cortex. bioRxiv doi: 10.1101/384826.

Hoff PD, Raftery AE, Handcock MS (2002) Latent space approaches to social network analysis. J Am Stat Assoc 97:1090–1098.

Holland PW, Laskey KB, Leinhardt S (1983) Stochastic blockmodels: first steps. Social Networks 5:109–137.

Huber PJ, Ronchetti EM (1981) Robust statistics. Wiley Series in Probability and Statistics, Ed 2, Vol 82. Hoboken, NJ: Wiley.

Kass RE, Eden UT, Brown EN, eds. (2014) Analysis of neural data. Springer series in statistics. Berlin Heidelberg: Springer.

Kiar G, Bridgeford E, Roncal WG, Consortium for Reliability and Reproducibility (CoRR), Chandrashekhar V, Mhembere D, Ryman S, Zuo X-N, Marguiles DS, Craddock RC, Priebe CE, Jung R, Calhoun V, Caffo B, Burns R, Milham MP, Vogelstein J (2018) A high-throughput pipeline identifies robust connectomes but troublesome variability. bioRxiv doi: 10.1101/188706.

Levin K, Athreya A, Tang M, Lyzinski V, Priebe CE (2017) A central limit theorem for an omnibus embedding of random dot product graphs. Paper presented at IEEE International Conference on Data Mining, New Orleans, LA, November 18–21.

Lindenbaum O, Yeredor A, Salhov M, Averbuch A (2015) MultiView diffusion maps. arXiv:1508.05550.

Lu J, Tapia JC, White OL, Lichtman JW (2009) The interscutularis muscle connectome. PLoS Biol 7:e1000032.

Lyzinski V, Tang M, Athreya A, Park Y, Priebe CE (2017) Community detection and classification in hierarchical stochastic blockmodels. IEEE Trans Netw Sci Eng 4:13–26.

Mai JK, Paxinos G, Voss T (2007) Atlas of the human brain, Ed 3. San Diego: Academic Press.

NOTES

Markram H, Muller E, Ramaswamy S, Reimann MW, Abdellah M, Sanchez CA, Ailamaki A, Alonso-Nanclares L, Antille N, Arsever S, Kahou GA, Berger TK, Bilgili A, Buncic N, Chalimourda A, Chindemi G, Courcol JD, Delalondre F, Delattre V, Druckmann S, et al. (2015) Reconstruction and simulation of neocortical microcircuitry. Cell 163:456–492.

Mill RD, Ito T, Cole MW (2017) From connectome to cognition: the search for mechanism in human functional brain networks. Neuroimage 160:124–139.

Powell MA, Garcia JO, Yeh F-C, Vettel JM, Verstynen T (2018) Local connectome phenotypes predict social, health, and cognitive factors. Netw Neurosci 2:86–105.

Priebe CE, Park Y, Tang M, Athreya A, Lyzinski V, Vogelstein JT, Qin Y, Cocanougher B, Eichler K, Zlatic M, Cardona A (2017) Semiparametric spectral modeling of the *Drosophila* connectome. arXiv: 1705.03297.

Purves D, Lichtman JW (1985) Principles of neural development, Ed 1. Sunderland, MA: Sinauer.

Rohe K, Chatterjee S, Yu B (2011) Spectral clustering and the high-dimensional stochastic blockmodel. Ann Stat 39:1878–1915

Rosenthal G, Váša F, Griŷa A, Hagmann P, Amico E, Goñi J, Avidan G, Sporns O (2018) Mapping higher-order relations between brain structure and function with embedded vector representations of connectomes. Nat Commun 9:2178.

Rubin-Delanchy P, Priebe CE, Tang M (2017) The generalised random dot product graph. arXiv: 1709.05506.

Scheinerman ER, Tucker K (2009) Modeling graphs using dot product representations. Comput Stat 25:1–16.

Scott JP (1962) Critical periods in behavioral development. Science 138:949–958.

Seeds AM, Ravbar P, Chung P, Hampel S, Midgley FM Jr, Mensh BD, Simpson JH (2014) A suppression hierarchy among competing motor programs drives sequential grooming in *Drosophila*. eLife 3:e02951.

Sporns O, Tononi G, Kötter R (2005) The human connectome: a structural description of the human brain. PLoS Comput Biol 1:e42.

Spronk M, Kulkarni K, Ji JL, Keane B, Anticevic A, Cole MW (2018) A whole-brain and cross-diagnostic perspective on functional brain network dysfunction. bioRxiv doi:10.1101/326728.

Sussman DL, Tang M, Fishkind DE, Priebe CE (2011) A consistent adjacency spectral embedding for stochastic blockmodel graphs. J Am Stat Assoc 107:1119–1128.

Takemura SY, Bharioke A, Lu Z, Nern A, Vitaladevuni S, Rivlin PK, Katz WT, Olbris DJ, Plaza SM, Winston P, Zhao T, Horne JA, Fetter RD, Takemura S, Blazek K, Chang LA, Ogundeyi O, Saunders MA, Shapiro V, Sigmund C, et al. (2013) A visual motion detection circuit suggested by *Drosophila* connectomics. Nature 500:175–181.

Takemura SY, Xu CS, Lu Z, Rivlin PK, Parag T, Olbris DJ, Plaza S, Zhao T, Katz WT, Umayam L, Weaver C, Hess HF, Horne JA, Nunez-Iglesias J, Aniceto R, Chang LA, Lauchie S, Nasca A, Ogundeyi O, Sigmund C, et al. (2015) Synaptic circuits and their variations within different columns in the visual system of *Drosophila*. Proc Natl Acad Sci USA 112:13711–13716.

Takemura SY, Nern A, Chklovskii DB, Scheffer LK, Rubin GM, Meinertzhagen IA (2017) The comprehensive connectome of a neural substrate for 'ON' motion detection in *Drosophila*. eLife 6:e24394.

Tang R, Ketcha M, Badea A, Calabrese ED, Margulies DS, Vogelstein JT, Priebe CE, Sussman DL (2016) Connectome smoothing via low-rank approximations. arXiv: 1609.01672.

Tang R, Tang M, Vogelstein JT, Priebe CE (2017a) Robust estimation from multiple graphs under gross error contamination. arXiv: 1707.03487.

Tang M, Cape J, Priebe CE (2017b) Asymptotically efficient estimators for stochastic blockmodels: the naive MLE, the rank-constrained MLE, and the spectral. arXiv: 1710.10936.

Tang M, Athreya A, Sussman DL, Lyzinski V, Park Y, Priebe CE (2017c) A semiparametric two-sample hypothesis testing problem for random graphs. J Comput Graph Stat 26:344–354.

Tomasetti C, Vogelstein B (2015) Cancer etiology: variation in cancer risk among tissues can be explained by the number of stem cell divisions. Science 347:78–81.

Van Dam NT, O'Connor D, Marcelle ET, Ho EJ, Cameron Craddock C, Tobe RH, Gabbay V, Hudziak JJ, Xavier Castellanos F, Leventhal BL, Milham MP (2017) Data-driven phenotypic categorization for neurobiological analyses: beyond DSM-5 labels. Biol Psychiatry 81:484–494.

NOTES

Varshney LR, Chen BL, Paniagua E, Hall DH, Chklovskii DB (2011) Structural properties of the *Caenorhabditis elegans* neuronal network. PLoS Comput Biol 7:e1001066.

Wang S, Yang Z, Milham M, Craddock C, Zuo X-N, Priebe CE, Vogelstein JT (2015) Optimal experimental design for generating reference connectome datasets. Poster 3544 presented at Organization for Human Brain Mapping 21st Annual Meeting, Honolulu, HI, June 14–18.

Wang S, Vogelstein JT, Priebe CE (2017) Joint embedding of graphs. arXiv: 1703.03862.

Wasserman S, Anderson CH (1987) Stochastic *a posteriori* blockmodels: construction and assessment. Soc Netw 9:1–36.

White JG, Southgate E, Thomson JN, Brenner S (1986) The structure of the nervous system of the nematode *Caenorhabditis elegans*. Philos Trans R Soc Lond B Biol Sci 314:1–340.

Young SJ, Scheinerman ER (2007) Random dot product graph models for social networks. In: Algorithms and models for the web-graph, pp 138–149. Berlin Heidelberg: Springer.

Zhang W, Linden DJ (2003) The other side of the engram: experience-driven changes in neuronal intrinsic excitability. Nat Rev Neurosci 4:885–900.

Zhang Z, Allen GI, Zhu H, Dunson D (2018) Tensor network factorizations: relationships between brain structural connectomes and traits. arXiv:1806.02905.

Zuo XN, Ehmke R, Mennes M, Imperati D, Castellanos FX, Sporns O, Milham MP (2012) Network centrality in the human functional connectome. Cereb Cortex 22:1862–1875.

Zuo XN, Anderson JS, Bellec P, Birn RM, Biswal BB, Blautzik J, Breitner JC, Buckner RL, Calhoun VD, Castellanos FX, Chen A, Chen B, Chen J, Chen X, Colcombe SJ, Courtney W, Craddock RC, Di Martino A, Dong HM, Fu X, et al. (2014) An open science resource for establishing reliability and reproducibility in functional connectomics. Sci Data 1:140049.

# Analysis of Functional Imaging Data at Single-Cellular Resolution

Eftychios A. Pnevmatikakis, PhD,[1] and Liam Paninski, PhD[2]

[1]Center for Computational Biology
Flatiron Institute
New York, New York

[2]Departments of Statistics and Neuroscience
Grossman Center for the Statistics of Mind
Center for Theoretical Neuroscience
Columbia University
New York, New York

NOTES

## Introduction

Calcium imaging has become the dominant method for making recordings from large populations of neurons, owing to several well-known advantages: (1) it offers subcellular spatial resolution with cell-type specificity and can be coupled easily with a variety of genetic tools; (2) it has proven scalability to record simultaneously from O($10^4$) neurons *in vivo*; and (3) it allows for longitudinal tracking of cellular activity across multiple days.

At the same time, calcium imaging presents some important analysis challenges: calcium signals represent a slow, nonlinear encoding of the underlying spike train signals of interest, and therefore it is necessary to denoise, temporally deconvolve, and spatially demix calcium video data into estimates of neural activity. In addition, calcium imaging produces datasets that can be quite large (hundreds of gigabytes per hour in some cases); thus, analysis methods must be scalable and as automated and reproducible as possible.

This chapter presents an overview of state-of-the-art analysis methods for calcium imaging data, with a focus on data recorded at single-neuron resolution. We will also touch briefly on the analysis of voltage imaging data and wide-field calcium imaging data, both of which come with their own related but distinct analysis challenges.

## Steps in a Calcium Imaging Analysis Pipeline

We begin with an overview of the typical steps in a modern calcium imaging analysis pipeline (Fig. 1). After correction of low-level issues (e.g., different gains or noise levels on different pixels in CMOS cameras, or line-to-line phase errors in multiphoton scanning imaging), the dataset in movie format is motion-corrected to remove artifacts arising from brain motion and slow imaging rate (Figs. 1*a*,*b*). Next the movie is denoised and compressed into a smaller format. Subsequently, the movie is demixed to extract a shape and temporal trace corresponding to each neural component (Fig. 1*c*). These temporal traces represent the average fluorescence within each spatial component in each temporal frame and are therefore an indirect measure of neural activity; these traces can be temporally deconvolved to estimate the underlying activity of each corresponding neuron. Finally, an imaging experiment can visit the same field of view (FOV) over the course of multiple sessions or days (Fig. 1*d*). To combine the results from multiple sessions, the components from the different sessions need to be registered. Below we discuss each of these steps in more detail.

### Motion correction

Motion artifacts in calcium imaging datasets can arise from natural brain movement. For a small FOV, this motion can be approximated as rigid, and can usually be corrected using standard template-based registration methods (Thevenaz et al., 1998). (In general, motion within the imaging plane is easier to correct; in contrast, motion out of the imaging plane can cause artifacts in which cells pop in and out of the plane, and therefore appear to turn on and off, respectively. Extending the depth of field can ameliorate this problem to some degree.) However, in multiphoton imaging data, brain motion can be faster than the raster scanning imaging rate, resulting in nonuniform motion artifacts within a data frame; nonrigid registration methods have been developed to handle these effects (Dombeck et al., 2007; Greenberg and Kerr, 2009). For larger FOVs, the rigid motion approximation is often insufficient; to handle this shortcoming, we can split the FOV into smaller spatial patches, compute motion corrections within each patch, and then combine the results over patches (Pnevmatikakis and Giovannucci, 2017). This local "patchwise" processing approach helps parallelize computation and enables scalability to very large datasets, and will be a recurring theme in this chapter.

One significant problem requires further development: tracking activity with single-neuron resolution in small moving animals with flexible nervous systems, e.g., larval zebrafish (Cong et al., 2017), *Drosophila* (Bouchard et al., 2015), or *Hydra* (Dupre and Yuste, 2017). Although good solutions have been developed in *Caenorhabditis elegans* (Christensen et al., 2015; Venkatachalam et al., 2016; Nguyen et al., 2017), demixing of fast cytosolic (nonnuclear-localized) signals in small flexible animals remains an unsolved problem. We expect nonrigid registration approaches similar to those developed by Pnevmatikakis and Giovannucci (2017) to be helpful here.

### Denoising and compression

To facilitate visualization and further processing at this stage, it is useful to denoise the data—i.e., to separate the signal from the noise and discard the noise—and compress the signal into a format that can be stored and processed more efficiently. Denoising is particularly useful for fast or low-intensity imaging methods for which photon count noise may be relatively high compared with the

NOTES

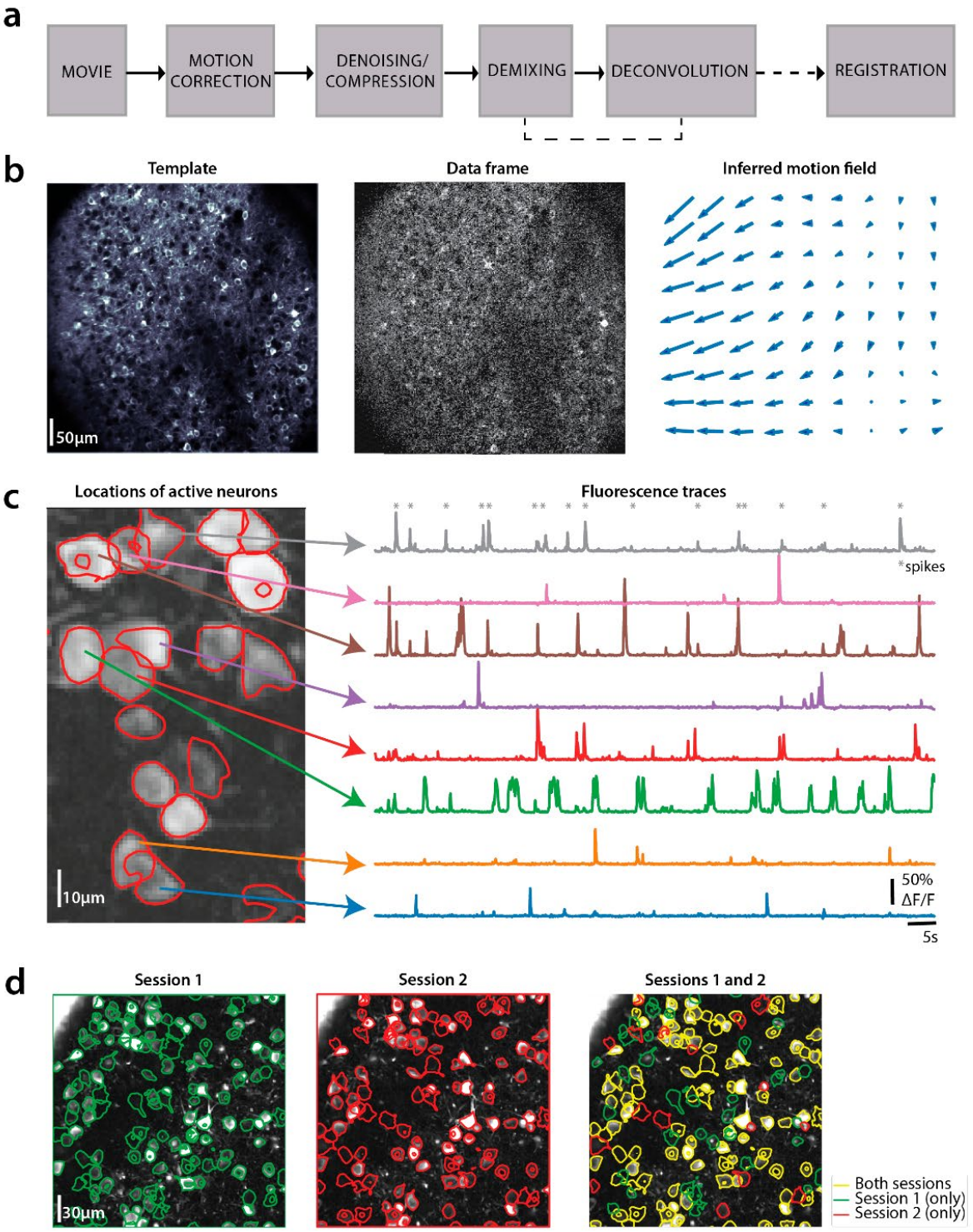


**Figure 1.** Typical analysis pipeline for calcium imaging data. ***a***, The data are first processed for removing motion artifacts. ***b***, This can be done by estimating a motion field from aligning each data frame to a template. ***c***, Subsequently, the locations of the neurons in the imaged FOV and their activity are extracted. Neurons can appear as spatially overlapping owing to limited axial resolution, and their activity needs to be demixed. The activity of each neuron (spikes, gray stars) can be estimated from its corresponding fluorescence trace. ***d***, Left, Middle, Registration of components produced by imaging sessions with the same FOV over the course of different days. Right, Neurons that are active in all or only some of the imaged sessions are identified. The different steps of the pipeline are displayed on mouse *in vivo* cortex data, courtesy of S.A. Koay and D. Tank (Princeton University). Results were obtained using the CaImAn package (Giovannucci et al., 2018). Scale bars: ***b***, 50 µm; ***c***, 10 µm; ***d***, 30 µmµ. Calibration: vertical indicates 50% increase relative to baseline fluorescence; horizontal, 5 s.

NOTES

signal. Principal component analysis (PCA) is often applied here (Mukamel et al., 2009; Pachitariu et al., 2017). Recently, Buchanan et al. (2018) pointed out that the statistical model underlying PCA is not very well matched to functional imaging data, leading to relatively slow computation and suboptimal separation of signal from noise. By incorporating a more appropriate statistical model (exploiting the fact that signals are local in space, and the dominant noise sources are temporally and spatially uncorrelated), Buchanan et al. (2018) developed a patchwise penalized matrix decomposition approach that achieves significantly faster computation and improved denoising and compression (~2–4× increases in signal-to-noise ratio [SNR] and compression rates of 20–300×, with minimal visible loss of signal). Notably, these methods are effective across a wide variety of functional imaging data, including single-photon, multiphoton, calcium, voltage, wide-field, and single-cellular resolution, with no manual parameter adjustment required.

In some datasets, it is necessary to include a detrending step here to remove photobleaching effects (Buchanan et al., 2018). In addition, some approaches (e.g., wide-field calcium imaging) require another step to remove contamination from hemodynamic signals (Ma et al., 2016). Because of space constraints, we will not review either of these issues in depth here.

## Demixing

The next task is to demix activity from the multiple spatially overlapping neurons visible in the FOV into separate components. (This problem is analogous to the "spike-sorting" problem from classical extracellular electrophysiology.) A natural approach is to model the observed movie data as follows:

$$Y(x, t) = \sum_{i=1}^{K} a_i(x) c_i(t) + B(x, t) + \varepsilon_{x,t}. \qquad (1)$$

Here $Y(x, t)$ denotes the observed fluorescence at location $x$ and time $t$, and $a_i$ and $c_i$ denote the spatial footprint and fluorescence trace, respectively, of the $i$-th neural component, with $K$ denoting the number of neurons visible in the FOV.[1] $B(x, t)$ denotes the neuropil/background activity and $\varepsilon_{x,t}$ measurement noise, respectively; the background $B(x, t)$ represents the summed contributions from processes that cannot be reliably separated into single-neuron components.

Equation 1 is a reasonable starting point, but it is not yet a fully specified statistical model in which all the components are identifiable (since we could trivially set $B(x, t)$ to equal $Y(x, t)$ and fully explain the observed data). To make further progress, we need to introduce statistical assumptions or constraints on the model components, and then develop efficient, scalable algorithms for inferring the components from data. Different choices for these constraints have led to different algorithms based on Equation 1. For example, the independent components analysis (ICA) approach in Mukamel et al. (2009) does not constrain the spatial components $a_i$ (and discards $B(x, t)$ from the model) while searching for maximally independent temporal components $c_i$. The constrained nonnegative matrix factorization (CNMF) approach developed in Pnevmatikakis et al. (2016) imposes nonnegativity and sparsity constraints on $a_i$ and $c_i$ and models $B(x, t)$ as a low-rank matrix within small spatial patches; by incorporating a more appropriate statistical model, CNMF achieves better performance than the less structured ICA approach. Pachitariu et al. (2017) use a similar CNMF approach, but with a slightly different objective function and background model. Giovannucci et al. (2017) developed a real-time CNMF implementation that processes incoming data online, one imaging frame at a time, enabling closed-loop experiments. Zhou et al. (2018) introduced a more flexible model for $B(x, t)$ to handle data from one-photon imaging approaches, where background contributions from out-of-focus light are much more severe than in multiphoton data; if these background effects are not handled correctly, strong spurious correlations between neighboring neurons can corrupt downstream analyses. Buchanan et al. (2018) introduced a new, more robust method for initializing the CNMF model and demonstrated significantly improved performance on spatially extended dendritic signals; they also showed that the CNMF approach can be extended to handle

1 It is useful to distinguish this demixing problem from simpler segmentation problems that are the subject of large computer vision and biological image processing literatures. In a segmentation problem, we would want to assign each pixel to at most a single neuron, so for each location $x$, at most one $a_i(x)$ would be allowed to be nonzero. Instead, in Equation 1 we allow multiple neurons $i$ to contribute to a given pixel $x$, since even in the multiphoton imaging setting, a single diffraction-limited excitation spot will often excite fluorophores from multiple neurons. Correctly assigning fluorescence signals to each neuron (i.e., solving the full demixing problem) is particularly critical for any downstream analyses of the correlations between neighboring neurons.

NOTES

voltage imaging data. Finally, Giovannucci et al. (2018) incorporated a convolutional artificial neural network to help initialize new neural components in online CNMF, building on earlier work by Apthorpe et al. (2016) and Klibisz et al. (2017). The approaches developed in Zhou et al. (2018), Giovannucci et al. (2018), and Buchanan et al. (2018) all incorporate patchwise processing to scale to very large movies. Several other papers have developed approaches based on Equation 1, including Maruyama et al. (2014), Andilla and Hamprecht (2014), Haeffele and Vidal (2017), Inan et al. (2017), Takekawa et al. (2017), Nöbauer et al. (2017), and Petersen et al. (2017), but we lack the space to review all of their work here.

***Benchmarking***

One major open issue is the lack of so-called gold-standard datasets that can be used to objectively score algorithm performance. The iterative optimization of open-sourced algorithms on agreed-upon standard datasets has been a critical theme enabling progress in modern machine learning (Donoho, 2017). Some gold-standard datasets have been developed for the segmentation problem of finding nuclei or somas in calcium imaging data, either via manual annotation or the segmentation of datasets in which neurons coexpress a static structural indicator (see, e.g., http://neurofinder.codeneuro.org/ for some example datasets). However, these segmented datasets can be unreliable: expression of structural indicators does not discriminate between active and inactive neurons, and is not guaranteed to be constrained only to neurons where the functional indicator is expressed. Moreover, as shown in Giovannucci et al. (2018), individual manual annotations can be highly variable, with different labelers disagreeing by up to 20% on the same dataset. Finally, these segmented datasets only partially indicate some of the (somatic) pixels within the spatial components $a_i$, and do not provide ground-truth data for the primary objects of interest in the demixing problem (i.e., the full demixed spatial and temporal components $a_i$ and $c_i$). Ground truth for the temporal components would be important for assessing the robustness of demixing methods to neuropil contamination or contamination from small spatially overlapping neurites (Gauthier et al., 2017).

Thus, the curation of fully spatiotemporal gold-standard demixing datasets remains a critical challenge; the IARPA MICrONS (Machine Intelligence from Cortical Neurons) project (www.iarpa.gov/index.php/research-programs/microns) will soon deliver public datasets that combine large-scale electron microscopy with calcium imaging in the same cortical volumes, and will therefore serve as a major step forward in this direction. Meanwhile, realistic generative models (Song et al., 2017a) can also generate useful simulated ground-truth data.

***Toward optimal computational imaging and extensions beyond calcium imaging***

One major trend we see guiding research in this area over the next several years involves the joint optimization of experimental design and analysis methods in order to image larger populations at higher temporal resolution. The suboptimality of, for example, optimizing an imaging apparatus in isolation is widely recognized; instead, the full experimental preparation, imaging technology, and computational analysis approach should be considered as parts of a pipeline to be optimized as a whole. Many researchers (Pnevmatikakis and Paninski, 2013; Yang et al., 2016; Prevedel et al., 2016; Friedrich et al., 2017a; Lu et al., 2017; Song et al., 2017b; Kazemipour et al., 2018) have offered variations on a theme: spatial resolution can be usefully traded off for temporal resolution. That is, we can record from more cells and/or with higher temporal resolution if we are willing to accept a lower ratio of pixels per cell. Moreover, previous information about cell shapes and locations can shift the favorable point of this trade-off even further: once we know the locations and shapes of the cells in the FOV, we can reduce our spatial resolution even more without negatively impacting the quality of the recovered temporal neural activity (Pnevmatikakis and Paninski, 2013; Yang et al., 2016; Friedrich et al., 2017a; Kazemipour et al., 2018). All these approaches can be cast in the same mathematical framework: instead of directly observing $Y$ in Equation 1, we observe $WY$ instead, where $W$ is some linear operator that depends on the details of the imaging technique. A number of generalized demixing approaches have been developed to handle these data types; we expect to see continued algorithmic development in this direction in the near future. Simulators such as those developed in Song et al. (2017a) will again likely play a useful role in the ongoing joint optimization of demixing methods and hardware design, as we push the limits of critical imaging-system parameters such as labeling density, imaging speed, SNR, and FOV size (and the number of neurons observed simultaneously).

Although this chapter focuses on calcium imaging, many similar themes will hold for voltage imaging at single-cell resolution (Buchanan et al., 2018), which is expected to be a major growth area during the next decade (Xu et al., 2017). Of course, voltage imaging methods also provide the opportunity to record at subcellular resolution, at multiple points along the

NOTES

dendrite and axon. Once these imaging methods become more mature, we expect to see rapid growth in statistical methods for extracting information from this noisy spatiotemporal data; earlier works offer algorithmic starting points for modeling voltage data with subcellular resolution (Huys et al., 2006; Huys and Paninski, 2009; Paninski, 2010; Pakman et al., 2014).

## Deconvolution

The demixing methods discussed earlier in this chapter output temporal components $c_i$ for each neuron in the FOV; $c_i(t)$ is proportional to the average fluorescence in neuron $i$ at time $t$ (Eq. 1). Deconvolution methods aim to estimate the activity of each neuron $i$ given the extracted fluorescence trace $c_i$. This problem can be challenging because of several factors: the unknown and often nonlinear nature of the indicator dynamics, the presence of measurement noise, and the relatively low imaging rate of typical calcium recordings. A popular approach assumes linear and time-invariant dynamics, expressing the fluorescence trace c as the sum of the calcium transients due to neural activity plus measurement noise:

$$c(t) = \sum_{j=1}^{N} s_j\, h(t - t_j) + b + \varepsilon_t. \qquad (2)$$

Here $t_j$, $s_j$ denote the time and amplitude of the $j$-th transient, $h$ is a causal function denoting the shape of the transient, and $b$, $\varepsilon_t$ denote the (possibly time-varying) baseline and measurement noise at time $t$. Transients are characterized typically by fast rise followed by a slower decay. This behavior can be modeled using a simple single or double exponential model. Under these assumptions, the deconvolution problem can be cast as a convex optimization problem that can be solved efficiently. See Vogelstein et al. (2010) for early work in this direction, and Pnevmatikakis et al. (2016), Jewell and Witten (2017), and Tubiana et al. (2017) for more recent advances. Fast online formulations are also available (Friedrich et al., 2017b; Jewell et al., 2018), and methods based on more-detailed biophysical models, including nonlinearities, have been developed (Vogelstein et al., 2009; Deneux et al., 2016; Greenberg et al., 2018). Finally, these models can be used to denoise the trace $c_i$ ; this denoising step can be incorporated into the demixing step to improve performance (Pnevmatikakis et al., 2016).

Supervised learning methods have also been applied to the spike inference problem (Theis et al., 2016). Unlike the unsupervised methods reviewed above, supervised methods rely on training data, usually in the form of dual electrophysiological and imaging recordings in small neuron populations, which can be hard to obtain. If a good generative model of the data is available, however, then the model can be used to generate an unlimited amount of training data (Berens et al., 2018). The recent community benchmarking effort (Berens et al., 2018) found that current supervised and unsupervised learning algorithms perform similarly on the labeled datasets available at http://spikefinder.codeneuro.org/. On the other hand, Z. Wei (personal communication) investigated the impact of calcium indicator nonlinearities on downstream analyses of neural population activity, concluding that some caution is warranted when interpreting neural dynamics inferred from calcium imaging data.

The accuracy and temporal resolution of the recovered activity depend on several factors—most critically, the imaging frame rate, SNR, and indicator dynamics (particularly the rise time and degree of nonlinearity of the indicator). Without side information, it is not possible to recover spike times at millisecond resolution, given standard 30 Hz frame rates. However, Bayesian methods that incorporate prior information about spike timing (using information from the activity of other cells, or from external covariates such as stimulus or movement timing) can improve inference accuracy and temporal resolution beyond the original frame rate (Vogelstein et al., 2009; Deneux et al., 2016; Picardo et al., 2016; Aitchison et al., 2017).

Voltage imaging data will present some new challenges. In this context, we do not just care about recovering spike times; instead, we also wish to denoise and recover subthreshold voltage fluctuations. Thus, models that combine both sparse spiking effects with constraints on the smoothness of the subthreshold voltage will likely be critical. In addition, important tradeoffs between imaging frame rate, SNR, and the speed and brightness of the indicator will need to be optimized. For example, slower indicators may be brighter, and if deconvolution methods can improve the resulting temporal resolution, then using a slower indicator might be preferable. As in the demixing problem discussed earlier, we expect that an integrated computational imaging approach (in which we optimize jointly over the indicator, imaging approach, and computational deconvolution method) will lead to improved recovery of voltage signals.

## Postprocessing and visualization

Several postprocessing steps have been implemented to check for missing or clearly nonneuronal components $a_i$ or $c_i$ in the output of the demixing step; for example, in some cases, it is useful to apply *post hoc* image processing methods to remove artifacts

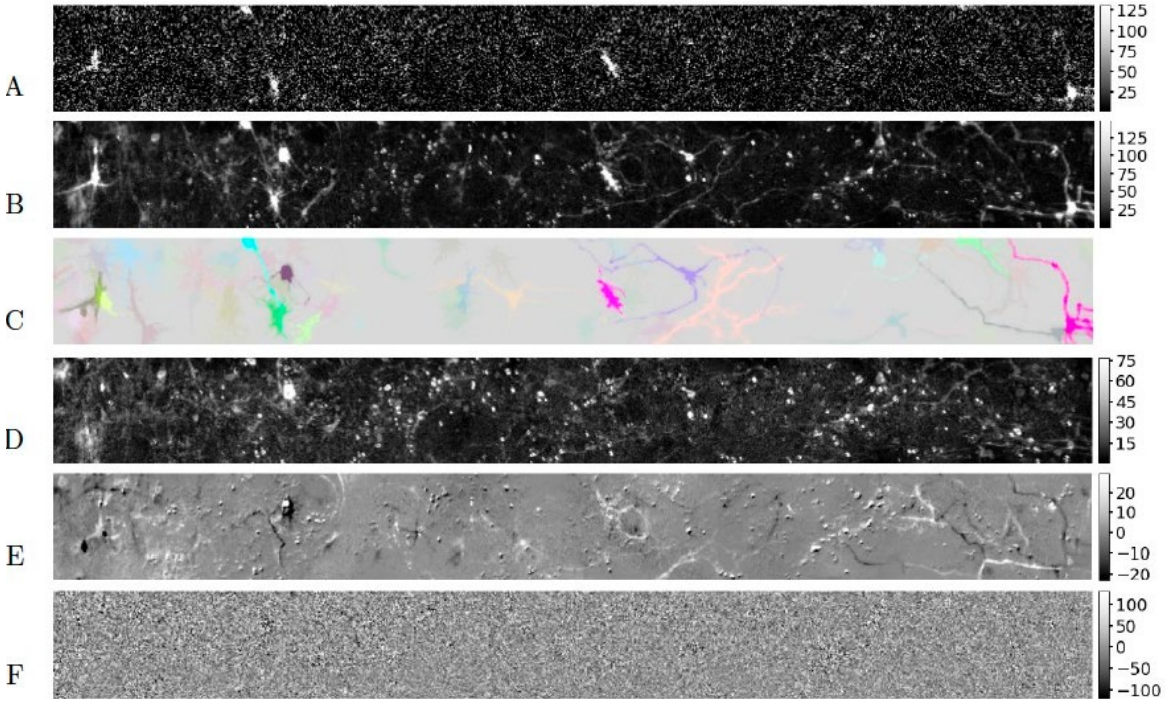


**Figure 2.** An example frame illustrating demixing on voltage imaging data. ***A***, Detrended data *Y*. ***B***, Denoised data *Y*. ***C***, Extracted signals *AC*; each component *i* is assigned a unique color, and the intensity of each pixel at each time is determined by the corresponding value of *AC*. ***D***, Estimated background *B* (constrained to be temporally constant here). ***E***, Residual $Y - AC - B$. Note the small scale of the residual result compared with the original signal. ***F***, Noise removed in the denoising step.

from spatial components. These approaches can also be incorporated within the demixing loop to improve overall demixing performance.

As in any complex statistical analysis, it is important to visualize the outputs of the pipelines described above (Fig. 2). One basic but critical visualization is to simply view the raw data movie Y synchronized with and adjacent to corresponding movies of the components the pipeline has extracted from Y (Figs. 2*A*–*D*), along with the residual result of $Y - AC - B$ (Fig. 2*E*). This visualization makes it easy to quickly identify poor motion correction, potential missing components, poor separation of background versus single-neuronal components, and other common artifacts.

Another useful visualization involves sorting the components $a_i$ and $c_i$ by brightness and then viewing each component individually. Typically the brightest output components will be of high quality, while the dimmest extracted components may be overly noisy or corrupted by artifacts. Quick visual inspection of the sorted components can determine a good value of the number of components to be retained ($K$ in Eq. 1). Simple graphical user interfaces have been developed to aid in this procedure, but further effort in this direction would be useful.

Finally, in general, any software used for manual intervention and/or postprocessing should include an automatic logger to ensure full reproducibility of the analysis.

### Registration across multiple sessions

Calcium imaging enables the monitoring of large neural populations over many different sessions across multiple days. Several packages offer semiautomated methods for registering neurons across multiple sessions (Kaifosh et al., 2014; Pachitariu et al., 2017; Sheintuch et al., 2017; Giovannucci et al., 2018). As in the demixing problem, ground-truth data for validating these methods are difficult to obtain; thus, the results of multisession alignment from challenging datasets (particularly one-photon imaging datasets with limited SNR or very large background signals) should be interpreted with caution (Katlowitz et al., 2018).

## Software Implementations

A critical requirement for the adoption of formal reproducible methods is the existence of reliable, well-documented software that is scalable to the size of modern datasets. Available packages for automated and/or interactive analysis include SIMA (Kaifosh et al., 2014; Python); Suite2p (Pachitariu et al.,

NOTES

2017; MATLAB and Python); ABLE (Reynolds et al., 2017; MATLAB); SCALPEL (Segmentation, Clustering, and Lasso Penalties, by Petersen et al., 2017; R); SamuROI (structured analysis of multiple user-defined regions of interest, by Rueckl et al., 2017; Python); the toolbox of Romano et al. (2017) (MATLAB); CaImAn (Giovannucci et al., 2018; Python and MATLAB); MIN1PIPE (MINiscope 1-photon imaging PIPEline, by Lu et al., 2018; MATLAB); and CNMF-E (constrained nonnegative matrix factorization for microendoscopic data, by Zhou et al., 2018; MATLAB). Most of the packages listed here focus on two-photon data; CNMF-E and MIN1PIPE can handle multiphoton data but are designed specifically for one-photon data. Of all these packages, at least CaImAn, CNMF-E, and Suite2p have attracted a critical mass of users and a community of developers that are continuing to support and improve the software.

## Open Issues and Future Work

The methods described above are the first step in the analysis of datasets that are being acquired daily in hundreds of neuroscience labs. These pipelines represent a foundation on which our understanding of the nervous system is being built; therefore, it is absolutely critical that this foundation be as sturdy as possible. Although the state of the art in this field has progressed rapidly in the past several years, significant work remains to be done.

We have already mentioned several directions for future work, including:

- Better graphical user interfaces for visualization and analysis;
- Methods for motion correction that can demix nonnuclear-localized signals in small flexible moving animals;
- Better gold-standard demixing data;
- Improved generalized demixing methods to handle experiments in which we observe some linear projection $WY$ of the data $Y$ in Equation 1; and
- Development of methods optimized to process voltage imaging and neurotransmitter release imaging data.

A number of additional directions remain open. For example, we expect to see further development of online, real-time-analysis approaches in the context of closed-loop experiments, building on the methods introduced in Giovannucci et al. (2017); the extension of these methods to handle single-photon data with large background signals (as is typical in microendoscopic imaging) is an important next step. Scalable Bayesian methods for quantifying the reliability of each component output by the demixing pipeline would also be very valuable. A number of open analysis challenges remain regarding multimodal data, i.e., functional imaging data collected in conjunction with, for example, electrophysiological data, spatial transcriptomics measurements, electron microscopy (or other very large-scale anatomical imaging approaches), or spatiotemporal patterned optogenetic stimulation.

More broadly, we advocate continued efforts toward full analysis standardization and automation to enable widespread, routine data sharing and reproducibility. Large collaborative experimental efforts such as the International Brain Laboratory (2017) depend on these efforts, and we expect to see a number of large-scale projects with similar requirements in the near future.

## Acknowledgments

This chapter was partially adapted with permission from two articles: Pnevmatikakis E (2018) Analysis pipelines for calcium imaging data (under review); and Paninski and Cunningham (2018) Neural data science: accelerating the experiment-analysis-theory cycle in large-scale neuroscience. Curr Opin Neurobiol 50:232–241. Copyright 2018, Elsevier. We thank S.A. Koay and D. Tank for the mouse *in vivo* dataset, and E. Buchanan, J. Friedrich, A. Giovannucci, I. Kinsella, D. Peterka, J. Vogelstein, D. Zhou, and P.C. Zhou for useful discussions. E.P. was internally funded by the Flatiron Institute. L.P. was funded by the Army Research Office W911NF-12-1-0594 Multidisciplinary University Research Initiative; the Simons Foundation Collaboration on the Global Brain; National Institutes of Health grants R01EB22913, R21EY027592, 1U01NS103489-01, and U19NS104649-01; and the Intelligence Advanced Research Projects Activity via Department of Interior/Interior Business Center contract D16PC00003.

NOTES

## References


Aitchison L, Russell L, Packer AM, Yan J, Castonguay P, Hausser M, and Turaga SC (2017) Model-based Bayesian inference of neural activity and connectivity from all-optical interrogation of a neural circuit. In: 2017 Advances in Neural Information Processing Systems, Vol 30 (Jordan MI, LeCun Y, Solla SA, eds), pp 3486–3495. Cambridge, MA: MIT Press.

Andilla FD, Hamprecht FA (2014) Sparse space-time deconvolution for calcium image analysis. In: 2014 Advances in Neural Information Processing Systems , Vol 27 (Ghahramani Z, Welling M, Cortes C, Lawrence ND, Weinberger KQ, eds), pp 64–72. Curran Associates, Inc.

Apthorpe N, Riordan A, Aguilar R, Homann J, Gu Y, Tank D, Seung HS (2016) Automatic neuron detection in calcium imaging data using convolutional networks. In: 2016 Advances in Neural Information Processing Systems, Vol 29 (Lee DD, Sugiyama M, Luxburg UV, Guyon I, Garnett R, eds), pp 3270–3278. Curran Associates, Inc.

Berens P, Freeman J, Deneux T, Chenkov N, McColgan T, Speiser A, Macke J H, Turaga S. C, Mineault, P, Rupprecht P, Gerhard S, Friedrich RW, Friedrich J, Paninski L, Pachitariu M, Harris KD, Bolte B, Machado TA, Ringach D, Stone J, et al. (2018) Community-based benchmarking improves spike rate inference from two-photon calcium imaging data. PLoS Comput Biol 14:e1006157.

Bouchard MB, Voleti V, Mendes CS, Lacefield C, Grueber WB, Mann RS, Bruno RM, Hillman EM (2015) Swept confocally-aligned planar excitation (SCAPE) microscopy for high-speed volumetric imaging of behaving organisms. Nat Photonics 9:113–119.

Buchanan EK, Kinsella I, Zhou D, Zhu R, Zhou P, Gerhard F, Ferrante J, Ma Y, Kim S, Shaik M, Liang Y, Lu R, Reimer J, Fahey P, Muhammad T, Dempsey G, Hillman E, Ji N, Tolias A, Paninski L (2018) Penalized matrix decomposition for denoising, compression, and improved demixing of functional imaging data. bioRxiv doi: 10.1101/334706.

Christensen RP, Bokinsky A, Santella A, Wu Y, Marquina-Solis J, Guo M, Kovacevic I, Kumar A, Winter PW, Tashakkori N, McCreedy E, Liu H, McAuliffe M, Mohler W, Colón-Ramos DA, Bao Z, Shroff H (2015) Untwisting the *Caenorhabditis elegans* embryo. eLife 4:e10070.

Cong L, Wang Z, Chai Y, Hang W, Shang C, Yang W, Bai L, Du J, Wang K, Wen Q (2017) Rapid whole brain imaging of neural activity in freely behaving larval zebrafish (*Danio rerio*). eLife 6:e28158.

Deneux T, Kaszas A, Szalay G, Katona G, Lakner T, Grinvald A, Rózsa B, Vanzetta I (2016) Accurate spike estimation from noisy calcium signals for ultrafast three-dimensional imaging of large neuronal populations *in vivo*. Nat Commun 7:12190.

Dombeck DA, Khabbaz AN, Collman F, Adelman TL, Tank DW (2007) Imaging large-scale neural activity with cellular resolution in awake, mobile mice. Neuron 56:43–57.

Donoho D (2017) 50 years of data science. J Comput Graph Stat 26:745–766.

Dupre C, Yuste R (2017) Non-overlapping neural networks in *Hydra vulgaris*. Curr Biol 27:1085–1097.

Friedrich J, Yang W, Soudry D, Mu Y, Ahrens MB, Yuste R, Peterka DS, Paninski L (2017a) Multi-scale approaches for high-speed imaging and analysis of large neural populations. PLoS Comput Biol 13:e1005685.

Friedrich J, Zhou P, Paninski L (2017b) Fast online deconvolution of calcium imaging data. PLoS Comput Biol 13:e1005423.

Gauthier J, Charles A, Pillow J, Tank D (2017) Robust estimation of calcium transients by modeling contamination. Abstract I-104 presented at Cosyne Conference, Salt Lake City, UT, February 23–26.

Giovannucci A, Friedrich J, Kaufman J, Churchland A, Chklovskii D, Paninski L, Pnevmatikakis EA (2017) OnACID: Online analysis of calcium imaging data in real time. In: 2017 Advances in Neural Information Processing Systems , Vol 30 (Jordan MI, LeCun Y, Solla SA, eds). Cambridge, MA: MIT Press.

Giovannucci A, Friedrich J, Gunn P, Kalfon J, Koay SA, Taxidis J, Najafi F, Gauthier JL, Zhou P, Tank DW, Chklovskii DB, Pnevmatikakis EA (2018) CaImAn: an open source tool for scalable calcium imaging data analysis. bioRxiv doi: 10.1101/339564.

Greenberg DS, Kerr J (2009) Automated correction of fast motion artifacts for two-photon imaging of awake animals. J Neurosci Methods 176:1–15.

NOTES

Greenberg D, Wallace D, Voit K.-M, Wuertenberger S, Czubayko U, Monsees A, Vogelstein J, Seifert R, Groemping Y, Kerr J (2018) Spike inference for genetically encoded calcium indicators with models of multistep binding kinetics. Abstract III-105 presented at Cosyne Conference, Denver, CO, March 1–4.

Haeffele BD, Vidal R (2017) Structured low-rank matrix factorization: global optimality, algorithms, and applications. arXiv:1708.07850v1.

Huys Q, Ahrens M, Paninski L (2006) Efficient estimation of detailed single-neuron models. J Neurophysiol 96:872–890.

Huys Q, Paninski L (2009) Model-based smoothing of, and parameter estimation from, noisy biophysical recordings. PLoS Comput Biol 5:e1000379.

Inan H, Erdogdu MA, Schnitzer M (2017) Robust estimation of neural signals in calcium imaging. In: 2017 Advances in Neural Information Processing Systems, Vol 30 (Jordan MI, LeCun Y, Solla SA, eds), pp 2905–2914. Cambridge, MA: MIT Press.

International Brain Lab (2017) An international laboratory for systems and computational neuroscience. Neuron 96:1213–1218.

Jewell S, Witten D (2017) Exact spike train inference via $\ell_0$ optimization. arXiv:1703.08644.

Jewell S, Hocking TD, Fearnhead P, Witten D (2018) Fast nonconvex deconvolution of calcium imaging data. arXiv:1802.07380.

Kaifosh P, Zaremba JD, Danielson NB, Losonczy A (2014) SIMA: Python software for analysis of dynamic fluorescence imaging data. Front Neuroinform 8:80.

Katlowitz KA, Picardo MA, Long MA (2018) Stable sequential activity underlying the maintenance of a precisely executed skilled behavior. Neuron 98:1133–1140.

Kazemipour A, Novak O, Flickinger D, Marvin JS, King J, Borden P, Druckmann S, Svoboda K, Looger LL, Podgorski K (2018) Kilohertz frame-rate two-photon tomography. bioRxiv 10.1101/357269.

Klibisz A, Rose D, Eicholtz M, Blundon J, Zakharenko S (2017) Fast, simple calcium imaging segmentation with fully convolutional networks. In: deep learning in medical image analysis and multimodal learning for clinical decision support, pp 285–293. Springer.

Lu J, Li C, Singh-Alvarado J, Zhou ZC, Fröhlich F, Mooney R, Wang F (2018) MIN1PIPE: a miniscope 1-photon-based calcium imaging signal extraction pipeline. Cell Rep 23:3673–3684.

Lu R, Sun W, Liang Y, Kerlin A, Bierfeld J, Seelig JD, Wilson DE, Scholl B, Mohar B, Tanimoto M, et al. (2017) Video-rate volumetric functional imaging of the brain at synaptic resolution. Nat Neurosci 20:620.

Ma Y, Shaik MA, Kim SH, Kozberg MG, Thibodeaux DN, Zhao HT, Yu H, Hillman EM (2016) Wide-field optical mapping of neural activity and brain haemodynamics: considerations and novel approaches. Philos Trans R Soc Lond B Biol Sci 371.

Maruyama R, Maeda K, Moroda H, Kato I, Inoue M, Miyakawa H, Aonishi T (2014) Detecting cells using non-negative matrix factorization on calcium imaging data. Neural Networks 55:11–19.

Mukamel EA, Nimmerjahn A, Schnitzer MJ (2009) Automated analysis of cellular signals from large-scale calcium imaging data. Neuron 63:747–760.

Nguyen JP, Linder AN, Plummer GS, Shaevitz JW, Leifer AM (2017) Automatically tracking neurons in a moving and deforming brain. PLoS Comput Biol 13:e1005517.

Nöbauer T, Skocek O, Pernía-Andrade AJ, Weilguny L, Traub FM, Molodtsov MI, Vaziri A (2017) Video rate volumetric $Ca^{2+}$ imaging across cortex using seeded iterative demixing (SID) microscopy. Nat Methods 14:811–818.

Pachitariu M, Stringer C, Dipoppa M, Schröder S, Rossi LF, Dalgleish H, Carandini M, Harris KD (2017) Suite2p: beyond 10,000 neurons with standard two-photon microscopy. bioRxiv doi: 10.1101/061507.

Pakman A, Huggins J, Smith C, Paninski L (2014) Fast state-space methods for inferring dendritic synaptic connectivity. J Comput Neurosci 36:415–443.

Paninski L (2010) Fast Kalman filtering on quasilinear dendritic trees. J Comput Neurosci 28:211–228.

Paninski L, Cunningham J (2018) Neural data science: accelerating the experiment-analysis-theory cycle in large-scale neuroscience. Curr Opin Neurobiol 50:232–241.

Petersen A, Simon N, Witten D (2017) SCALPEL: extracting neurons from calcium imaging data. arXiv:1703.06946.

Picardo MA, Merel J, Katlowitz KA, Vallentin D, Okobi DE, Benezra SE, Clary RC, Pnevmatikakis EA, Paninski L, Long MA (2016) Population-level representation of a temporal sequence underlying song production in the zebra finch. Neuron 90:866–876.

NOTES

Pnevmatikakis EA, Giovannucci A (2017) NoRMCorre: an online algorithm for piecewise rigid motion correction of calcium imaging data. J Neurosci Methods 291:83–94.

Pnevmatikakis EA, Paninski L (2013) Sparse nonnegative deconvolution for compressive calcium imaging: algorithms and phase transitions. In: 2013 Advances in neural information processing systems, Vol 26 (Burges CJC, Bottou L, Welling M, Ghahramani Z, Weinberger KQ, eds), pp 1250–1258. Curran Associates, Inc.

Pnevmatikakis EA, Soudry D, Gao Y, Machado TA, Merel J, Pfau D, Reardon T, Mu Y, Lacefield C, Yang W, Ahrens M, Bruno R, Jessell TM, Peterka DS, Yuste R, Paninski L (2016) Simultaneous denoising, deconvolution, and demixing of calcium imaging data. Neuron 89:285–299.

Prevedel R, Verhoef AJ, Pernia-Andrade AJ, Weisenburger S, Huang BS, Nöbauer T, Fernández A, Delcour JE, Golshani P, Baltuska A, Vaziri A (2016) Fast volumetric calcium imaging across multiple cortical layers using sculpted light. Nat Methods 13:1021–1028.

Reynolds S, Abrahamsson T, Schuck R, Sjöström PJ, Schultz SR, Dragotti PL (2017) ABLE: An activity-based level set segmentation algorithm for two-photon calcium imaging data. eNeuro 4:ENEURO.0012-17.2017.

Romano SA, Pérez-Schuster V, Jouary A, Boulanger-Weill J, Candeo A, Pietri T, Sumbre G (2017) An integrated calcium imaging processing toolbox for the analysis of neuronal population dynamics. PLoS Comput Biol 13:e1005526.

Rueckl M, Lenzi SC, Moreno-Velasquez L, Parthier D, Schmitz D, Ruediger S, Johenning FW (2017) SamuROI, a python-based software tool for visualization and analysis of dynamic time series imaging at multiple spatial scales. Front Neuroinform 11:44.

Sheintuch L, Rubin A, Brande-Eilat N, Geva N, Sadeh N, Pinchasof O, Ziv Y (2017) Tracking the same neurons across multiple days in $Ca^{2+}$ imaging data. Cell Rep 21:1102–1115.

Song A, Charles A, Gauthier J, Koay SA, Tank D, Pillow J (2017a) Two-photon microscopy simulation for optics optimization and benchmarking. Abstract III-57 presented at Cosyne Conference, Salt Lake City, UT, February 25.

Song A, Charles AS, Koay SA, Gauthier JL, Thiberge SY, Pillow JW, Tank DW (2017b) Volumetric two-photon imaging of neurons using stereoscopy (vTwINS). Nat Methods 14:420–426.

Takekawa T, Asai H, Ohkawa N, Nomoto M, Okubo-Suzuki R, Ghandour K, Sato M, Hayashi Y, Inokuchi K, Fukai T (2017) Automatic sorting system for large calcium imaging data. bioRxiv doi: 10.1101/215145.

Theis L, Berens P, Froudarakis E, Reimer J, Román Rosón M, Baden T, Euler T, Tolias AS, Bethge M (2016) Benchmarking spike rate inference in population calcium imaging. Neuron 90:471–482.

Thévenaz P, Ruttimann UE, Unser M (1998) A pyramid approach to subpixel registration based on intensity. IEEE Trans Image Process 7:27–41.

Tubiana J, Wolf S, Debregeas G (2017) Blind sparse deconvolution for inferring spike trains from fluorescence recordings. bioRxiv doi: 10.1101/156364.

Venkatachalam V, Ji N, Wang X, Clark C, Mitchell JK, Klein M, Tabone CJ, Florman J, Ji H, Greenwood J, Chisholm AD, Srinivasan J, Alkema M, Zhen M, Samuel ADT (2016) Pan-neuronal imaging in roaming *Caenorhabditis elegans*. Proc Natl Acad Sci USA 113:E1082–E1088.

Vogelstein JT, Watson BO, Packer AM, Yuste R, Jedynak B, Paninski L (2009) Spike inference from calcium imaging using sequential Monte Carlo methods. Biophys J 97:636–655.

Vogelstein JT, Packer AM, Machado TA, Sippy T, Babadi B, Yuste R, Paninski L (2010) Fast nonnegative deconvolution for spike train inference from population calcium imaging. J Neurophysiol 104:3691–3704.

Xu Y, Zou P, Cohen AE (2017) Voltage imaging with genetically encoded indicators. Curr Opin Chem Biol 39:1–10.

Yang W, Miller J-E, Carrillo-Reid L, Pnevmatikakis E, Paninski L, Yuste R, Peterka DS (2016) Simultaneous multi-plane imaging of neural circuits. Neuron 89:269–284.

Zhou P, Resendez SL, Rodriguez-Romaguera J, Jimenez JC, Neufeld SQ, Giovannucci A, Friedrich J, Pnevmatikakis EA, Stuber GD, Hen R, Kheirbek MA, Sabatini BL, Kass RE, Paninski L (2018) Efficient and accurate extraction of *in vivo* calcium signals from microendoscopic video data. eLife 7:e28728.

# High-Speed Volumetric Microscopy and Wide-Field Optical Mapping of Whole-Brain Activity

Elizabeth M. C. Hillman, PhD

Departments of Biomedical Engineering and Radiology
Mortimer B. Zuckerman Mind Brain Behavior Institute
Columbia University
New York, New York

NOTES

## Introduction

Despite dramatic improvements in *in vivo* optical reporters and modulators of neural activity over the past decade (Boyden et al., 2005; Chen et al., 2013; Gong et al., 2014; Dana et al., 2016), imaging challenges still limit our ability to capture the activity of thousands of neurons across large brain regions in awake behaving organisms.

Here we will describe two very different approaches to high-speed optical imaging of fluorescent reporters, both of which enable imaging of large numbers of brain cells in real time, in some cases capturing the whole brain or nervous system of behaving organisms. The first approach, swept confocally aligned planar excitation (SCAPE) microscopy, is capable of cellular-level imaging of ~1 × 1 × 0.4 mm fields of view (FOVs) at volumetric imaging speeds exceeding 50 volumes per second (VPS) (Bouchard et al., 2015). SCAPE can be used for *in vivo* microscopy in a diverse range of samples, from *Drosophila melanogaster* (fruit fly) larvae and adults, *Danio rerio* (zebrafish) larvae, and *Caenorhabditis elegans* (worms) to the intact cortex of awake behaving mice. SCAPE can also be used to image larger cleared and expanded tissue specimens at high speeds (Chung and Deisseroth, 2013; Chen et al., 2015). The second approach, wide-field optical mapping (WFOM), uses simple epifluorescence and diffuse reflectance imaging to capture larger-scale neural activity and brain hemodynamics across the dorsal surface of the cortex of awake behaving mice (Ma et al., 2016a,b).

Importantly, both imaging approaches offer sufficient signal-to-noise ratio (SNR) to capture interpretable data in real time. This enables observations of spontaneous behavior without the need to average over trials or tasks, thereby providing new views of the brain in real time in the context of ongoing behavior. The basic principles, capabilities, and limitations of these techniques are described below, along with novel applications we hope will provide new understanding of whole-brain activity.

## SCAPE for High-Speed, Cellular-Level Volumetric Microscopy in Functional Neuroimaging

### Point scanning for fast volumetric microscopy

SCAPE is an approach to *in vivo* microscopy that departs from conventional point-scanning confocal and two-photon microscopy. Point-scanning methods form an image by scanning a point of focused laser light around, and measuring signal from, each point in turn (Fig. 1*a*). However, point scanning is reaching its speed limit for fast volumetric imaging owing to several constraints: (1) the speed limit of physically scanning a focused laser beam in three dimensions (3D) at high speeds, with 24 kHz line-scan-rate resonant scanners being the current upper limit; (2) the proportional decrease in per-pixel integration time, which is reaching fluorescence lifetime, laser repetition, and fast-detector sensitivity limits; and (3) the resulting exposure of tissues to high-power laser illumination, which is reaching photobleaching and thermal damage limits (Hillman et al., 2018). For example, point-scanning a modest volume of 400 × 400 × 100 *x*–*y*–*z* voxels at 5 VPS would require scanners moving at 200 kHz line-scan rates. The pixel detection rate would be 80 MHz, equal to the pulse repetition rate of conventional Ti:Sapphire lasers used for two-photon microscopy, and it would provide a per-pixel integration time of 12 ns for single-photon applications. In contrast, the fluorescence lifetime of green fluorescent protein is between 1 and 4 ns (Pepperkok et al., 1999).

### Advantages of light-sheet illumination for fast volumetric microscopy

Instead of point scanning, SCAPE uses light-sheet illumination—generating a plane of light within the tissue and imaging that plane onto a camera (Bouchard et al., 2015). Illuminating a whole plane at once, and acquiring an image using a camera, permits simultaneous detection of all pixels in parallel (Figs. 1*b*,*c*). This approach circumvents many of the limits described above by greatly increasing per-pixel integration time and reducing physical scanning rates.

A further advantage of light-sheet illumination is that light-sheet photons propagate along the direction of the light sheet, providing multiple opportunities to generate usable fluorescence along their path. This property also reduces the number of photons incident on tissue that is not being imaged at that moment in time (Huisken et al., 2004). In contrast, point-scanning methods seek only to acquire fluorescence from a single location along the photons' path (the high numerical aperture [NA] focal point), while illumination of the tissue above and below the plane of interest represents unwanted exposure (Figs. 1*d*,*e*). Imaging multiple planes to form a volume causes repeated exposure of the rest of the volume. Point scanning's very short per-pixel integration times also require significantly more incident power to generate equivalent fluorescence signal. These effects can

NOTES

combine to produce substantial photobleaching and phototoxicity that limits the use of point scanning for fast, 3D live-cell imaging. In comparison, light-sheet imaging's more efficient use of excitation light, selective illumination of only the plane of interest, and longer integration times significantly reduce phototoxicity. (For a full model comparing parameters between approaches, see Hillman et al., 2018.)

## SCAPE permits single-objective light-sheet imaging at high speeds

Conventional light-sheet microscopy uses two separate orthogonal light paths for illumination and detection (Fig. 1*b*), a configuration that can restrict sample geometries and reduce imaging speeds owing to the need for synchrony between different scan paths (Huisken et al., 2004; Tomer et al., 2012;

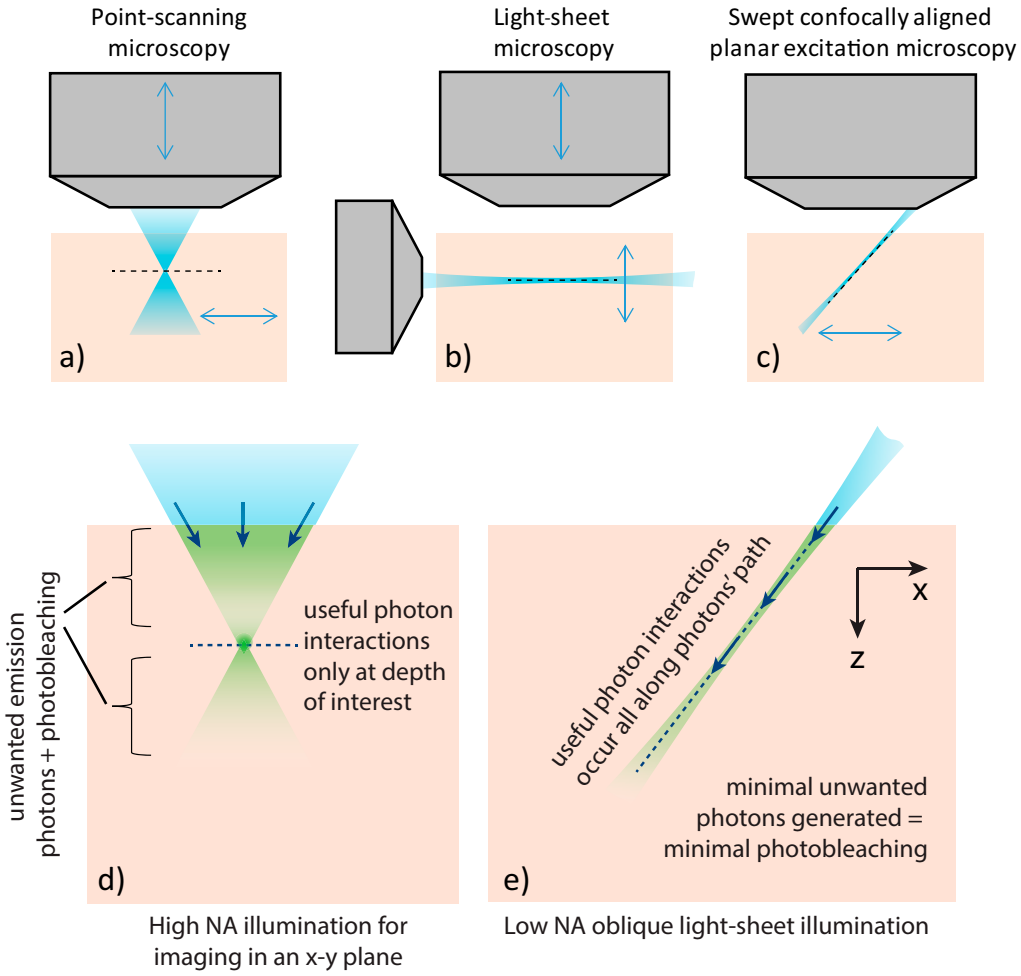


**Figure 1.** Point-scanning versus conventional and oblique light-sheet geometries. ***a***, Point-scanning confocal and two-photon microscopy illuminate tissue with a high-NA beam, forming a tight focus that is scanned in 3D to form a 3D image. ***b***, Conventional light-sheet microscopy illuminates tissue using a plane of light, with a camera focused onto that plane to generate optical sectioning. To form an image, the light sheet and camera focal plane (or the sample itself) must be translated up and down so that the camera remains focused on the light sheet throughout. ***c***, Oblique light-sheet microscopy (e.g., SCAPE) illuminates the tissue from its top surface using an oblique plane of light and collects emitted fluorescence back through the same objective lens. In SCAPE microscopy, volumetric data are acquired by scanning the light sheet from side to side using an approach that maintains the focus of the camera on the light sheet as it scans (Fig. 2*a*). ***d*** and ***e*** illustrate the main differences between point-scanning and light-sheet approaches, which provide significant signal-to-noise versus phototoxicity benefits: (1) High-NA point scanning reexposes tissue above and below the plane of interest for each plane imaged within the volume, whereas light-sheet microscopy restricts illumination to the plane being imaged so that volumetric imaging does not reexpose the whole volume for each plane; (2) Point scanning seeks to only detect photons from fluorescent interactions that occur at the focal point, so interactions above and below the plane provide only nuisance background and additional photodamage. Light sheets are generated by photons traveling in their propagation direction, affording multiple opportunities for excitation photons to interact along their path. As a result, light-sheet microscopy requires fewer photons to enter tissue per fluorescent photon detected. Modified with permission from Hillman et al. (2018), Figs. 1, 2. Copyright 2018, Elsevier.

NOTES

Ahrens et al., 2013). In contrast, SCAPE uses a single-objective lens at the sample, illuminating the sample with an oblique light sheet and detecting fluorescence back through the same objective lens (Fig. 1*c*). This single-objective configuration enables investigators to image diverse moving and intact samples in a more conventional upright or inverted "epifluorescence"-type geometry while delivering the benefits of light-sheet imaging over point scanning.

As shown in Figure 2*a*, to capture the fluorescence generated by the oblique light sheet, SCAPE uses image rotation to focus the oblique plane of the sheet onto a camera (Dunsby, 2008). To generate a 3D image, SCAPE sweeps this oblique sheet laterally across tissue using a single galvanometer (galvo) mirror positioned within the light path. The same mirror descans the returning light, which enables the system to maintain alignment between the stationary focal plane of the camera and the moving plane illuminated by the oblique light sheet in the sample. The only moving part of SCAPE is the galvo mirror, which moves at the volume rate (e.g., only 5–100 lines/s for 5–100 VPS). This single-scanner approach removes speed limitations of conventional two-path light-sheet configurations and requires no physical motion of the objective lens or sample to form a high-speed 3D image. SCAPE can thus image unmounted, freely moving, or sensitive small samples, as well as the brain of an awake behaving mouse at high volumetric imaging speeds. The primary limitations on imaging speed for SCAPE microscopy are the speed of the camera and the fluorescence intensity of the sample in relation to its photobleaching sensitivity.

## Applications of SCAPE microscopy

SCAPE has been applied to imaging a wide range of awake behaving organisms, such as the freely crawling *Drosophila* larva, the whole brain of behaving adult *Drosophila*, zebrafish brain and heart, *C. elegans* worms, as well as the cortex of awake mice. Two examples of high-speed functional brain imaging using SCAPE are shown in Figures 2*b*,*c*. Figure 2*b* shows spontaneous calcium (GCaMP6f) activity in apical dendrites from layer 5 neurons in the awake mouse barrel cortex acquired at 10 VPS to a depth of ~150 μm using 488 nm excitation. Raw fluorescence intensity data extracted from 2 × 2 × 2 voxel regions along individual dendrites over a 60 s time period is also shown. This dataset highlights SCAPE's ability to capture all activity in a 3D FOV >1 mm wide, to resolve fine structures in the dendritic branches, and to display good SNR and minimal photobleaching over 1 min of acquisition. These data also demonstrate significant improvement over imaging the same preparation using our first SCAPE prototype (Bouchard et al., 2015). Figure 2*c* shows SCAPE imaging of nuclear-localized GCaMP6f in neurons in the brain of a live zebrafish larva. SCAPE permits imaging without the need to translate the objective lens or the sample, thus reducing disturbance. The fact that SCAPE's oblique light sheet does not need to pass through the fish's eye is also a major advantage, while the simple mounting of the fish permits simple presentation of stimuli (e.g., visual patterns) as well as surveillance of the animal, including recording swim efforts or simultaneous electrode recordings. In this sample, data were acquired at 6 VPS for >1 h without evidence of phototoxicity (e.g., marked decreases in neural activity).

These examples demonstrate that SCAPE delivers the significant benefits of light-sheet imaging: reduced photodamage and improved SNR. These benefits combine with the ability to acquire volumetric images of unmounted, intact, behaving or freely moving samples at sufficiently high speeds to visualize cellular-level functional activity over large FOVs.

## Limitations of SCAPE microscopy

As with all microscopes, SCAPE's imaging depth is ultimately limited by light scattering and absorption in living tissues. In cleared tissues, SCAPE's depth of field can be >500 μm using a 20×, 1.0 NA objective, and it can image as deep into the tissue as the objective's working distance will allow. In more scattering samples, such as the mouse brain, this range can decrease to 250 μm using 488 nm excitation. Extended depths can be achieved by using longer-wavelength and two-photon excitation, although at increasing depths, the scattering of fluorescent light generated by the sheet will ultimately limit resolution and sensitivity at greater depths.

Compared with high-NA confocal and conventional light-sheet imaging using high-NA detection, SCAPE's resolution is currently limited by its inability to capture all the light from the full pupil of the primary objective lens. The other limit on its resolution is sample density, which is a function of the speed of available cameras. Today, standard scientific complementary metal-oxide-semiconductor CMOS (sCMOS) cameras can image ≤400 MHz pixel rates, but frame rates are dictated by the number of rows being read from the camera. On a standard sCMOS camera, 80 rows (depths) and the full chip width of >2000 columns (*y*-dimension) can be read at ~2400 Hz, enabling 240 planes in the *x*-direction to be read at 10 VPS. However, as faster cameras and more efficient fluorophores are developed, higher sampling rates are permitting volumetric imaging speeds of >100 VPS with sampling densities of <0.6 μm.

NOTES

## Zooming Out: WFOM of the Awake Mouse Brain

### Sacrificing cellular resolution for wider-field brain imaging

Although SCAPE can provide cellular-level imaging of functional dynamics over significant volumes of the rodent cortex (Fig. 2*b*), current implementations are unable to capture activity across bilateral mammalian cortex. However, the advent of robust genetically encoded calcium indicators (Akerboom et al., 2012; Chen et al., 2013; Dana et al., 2016) provides the opportunity for much simpler high-speed capture of pancortical cellular activity—if the user is willing to sacrifice resolving the activity of every individual neuron.

Classical neuroscience research has long focused on the activity of individual cells as the key to understanding circuits, but other neuroimaging modalities, such as functional magnetic resonance imaging (fMRI), electroencephalography (EEG),

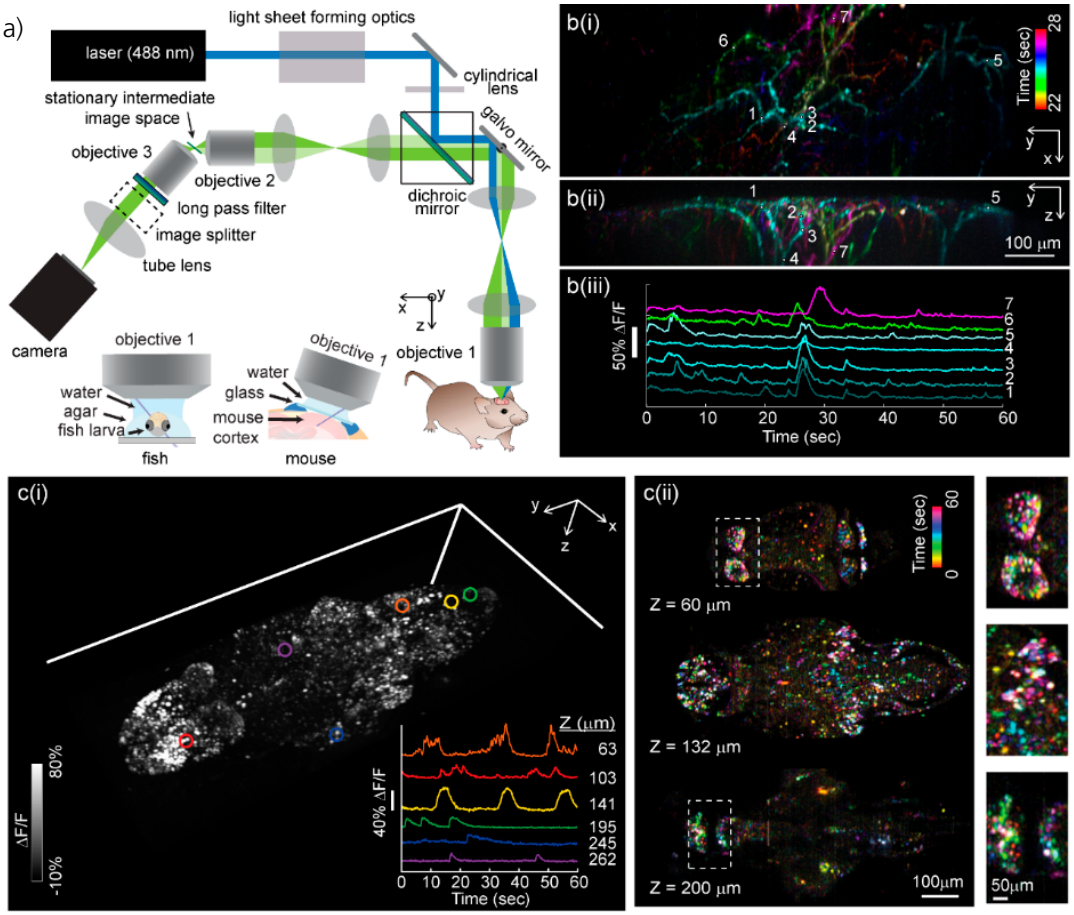


**Figure 2.** SCAPE microscopy for high-speed 3D neuroimaging. ***a***, Optical layout of a typical SCAPE system permitting oblique sheet scanning through a stationary, single-objective lens. Insets, Sample geometries for brain imaging in zebrafish larvae (left) and awake behaving mouse brain (right). ***b***, SCAPE data acquired at 10 VPS (140 × 750 × 149 *x*–*y*–*z* voxels = 372 × 1032 × 174 μm FOV) in an awake behaving mouse capturing spontaneous activity in apical dendrites of layer 5 neurons in whisker barrel cortex via GCaMP6f (AAV9.Syn.GCaMP6f). Methods used are similar to those of Bouchard et al. (2015) but with improved resolution, penetration depth, and SNR compared with our first demonstration. ***b***(*i*–*ii*), Maximum-intensity views from the top (*x*–*y*) and side (*y*–*z*) are shown for activity occurring between 22 s and 28 s (colors denote time). ***b***(*iii*), Raw fluorescence time courses from the regions of interest indicated are shown as raw data, showing excellent SNR, minimal photobleaching over 60 s, and the ability to probe firing dynamics along individual dendrites during a single spontaneous event. ***c***, Imaging of spontaneous activity in the whole brain of larval zebrafish: data were acquired at 6 VPS over a 820 × 380 × 260 μm FOV. (*i*) Volume rendering of a time-maximum-intensity projection taken over all 360 time points of the 1 min run. Inset, Time series extracted from six neurons at six depth planes within the fish as indicated. (*ii*) A time-encoded color projection of three depth planes showing spontaneous activity over a range of brain regions. Insets, ~2× close-ups of indicated regions. Seven days past fertilization HuC:H2B–GCaMP6f fish obtained from Janelia Farm. Scale bars: ***b***(*ii*), 100 μm; ***c***(*ii*), 100 μm; inset, 50 μm. Reprinted with permission from Hillman et al. (2018), Fig. 4. Copyright 2018, Elsevier.

NOTES

magnetoencephalography (MEG), and electrocorticography (ECoG), have taught us much about the brain from larger-scale representations of brainwide activity. The benefit of imaging genetically encoded fluorescent sensors is that the expression of indicators can be highly cell-specific, providing sensitivity to a particular cell type or chemical signal without necessarily requiring high spatial resolution. Beyond calcium-sensitive fluorophores, newer probes are also providing sensitivity to a wider array of neurotransmitters, neuromodulators, metabolites, and mediators of cellular signaling, including voltage (Shibuki et al., 2003; St-Pierre et al., 2014; Gong et al., 2015; Kozberg et al., 2016; Machler et al., 2016; Patriarchi et al., 2018). At the same time, new spectral variants are beginning to permit spectral encoding to report the activity of multiple cell types or chemical signatures in parallel (Dana et al., 2016). Capturing this highly specific activity in real time, across the bilateral cortex of awake behaving mammals, is increasingly providing a new view of brainwide, ensemble-scale activity that may not even be apparent when measuring a small number of individual cells (Vanni and Murphy, 2014; Ma et al., 2016a; Allen et al., 2017).

There is a wide range of approaches to this kind of imaging, of which WFOM is one (Fig. 3*a*) (Bouchard et al., 2009; Ma et al., 2016b). However, all methods require the following essential elements:

(1) A method for optically accessing the cortex. This could include thinning the skull; clearing the skull with index-matching compounds; removing part of the skull and replacing it with a glass window; or retracting the scalp and imaging through intact skull (although this obscures visualization of the cortical surface) (Figs. 3*b*,*c*).

(2) A light source capable of exciting the fluorophore at its excitation wavelength, along with a camera and an emission filter to block excitation light. High-power, stable light emitting diodes (LEDs) (Fig. 3*a*) provide higher spectral density than filtered white-light sources (Dunn et al., 2003; Bouchard et al., 2009). Modern sCMOS cameras are well suited to imaging fluorescence at high frame rates.

(3) An approach to compensating for the effects of hemoglobin absorption on the detected fluorescence signal.

## Hemodynamic correction in WFOM

The problem of hemodynamic contamination in wide-field fluorescence imaging is a key issue that cannot be ignored and has been addressed in a range of ways by different groups (Xu et al., 2015; Murphy et al., 2016; Ma et al., 2016c; Allen et al., 2017; Rossi et al., 2017). Changes in neural activity in the brain are generally accompanied by local increases in blood flow, which transiently increase both the local concentration and oxygenation state of hemoglobin in the tissue (Hillman, 2014). Hemoglobin is a strong light absorber that also has oxygenation-dependent shifts in its absorption spectrum. As Figure 3*d* illustrates, wide-field measurements of fluorescence require that excitation light ($I_1(\lambda_{ex})$, e.g., blue light for GCaMP) entering the tissue reaches cells expressing fluorescent markers. These fluorophores convert this incident light to longer-wavelength light ($I_1(\lambda_{em})$) (e.g., green light), which must then travel out of the tissue and be detected by a camera. In general, the path lengths ($X(\lambda_{ex})$ and $X(\lambda_{em})$) traveled by both excitation and emission light are much farther for wide-field measurements than for methods such as confocal microscopy, which effectively constrain the distance traveled by detected photons. To understand these effects, we can use the Beer–Lambert law, which describes how light is attenuated by an absorber (Fig. 3*d*):

$$I_2(\lambda) = I_1(\lambda)\, e^{-\mu_a(\lambda)X(\lambda)}, \quad (1)$$

where $\mu_a(\lambda)$ is the wavelength-dependent absorption coefficient of the tissue and is dominated by oxy-hemoglobin (HbO) and deoxy-hemoglobin (HbR) absorption at visible wavelengths (units of $mm^{-1}$), as given by:

$$\mu_a(\lambda) = c_{HbO}\varepsilon_{HbO}(\lambda) + c_{HbR}\varepsilon_{HbR}(\lambda). \quad (2)$$

In Equation 2, $c$ and $\varepsilon$ are the concentrations and molar extinction coefficients, respectively, of HbO and HbR. Thus, detected wide-field fluorescence signals ($I_2(\lambda_{em})$) will represent the true fluorescence $F$, contaminated by the effects of time-varying changes in hemoglobin concentration and oxygenation; the latter will differentially affect the intensity of blue excitation light reaching the fluorophores and the green light emitted by the fluorophores and reaching the camera. We can derive the following equations from Figure 3*d* (now including variations over time $t$):

$$I_2(t,\lambda_{ex}) = I_1(t,\lambda_{ex})\, e^{-\mu_a(t,\lambda_{ex})X(\lambda_{ex})} \quad (3)$$

$$I_1(t,\lambda_{em}) = I_2(t,\lambda_{ex})F(t) \quad (4)$$

$$I_2(t,\lambda_{em}) = I_1(t,\lambda_{em})\, e^{-\mu_a(t,\lambda_{em})X(\lambda_{em})} \quad (5)$$

NOTES

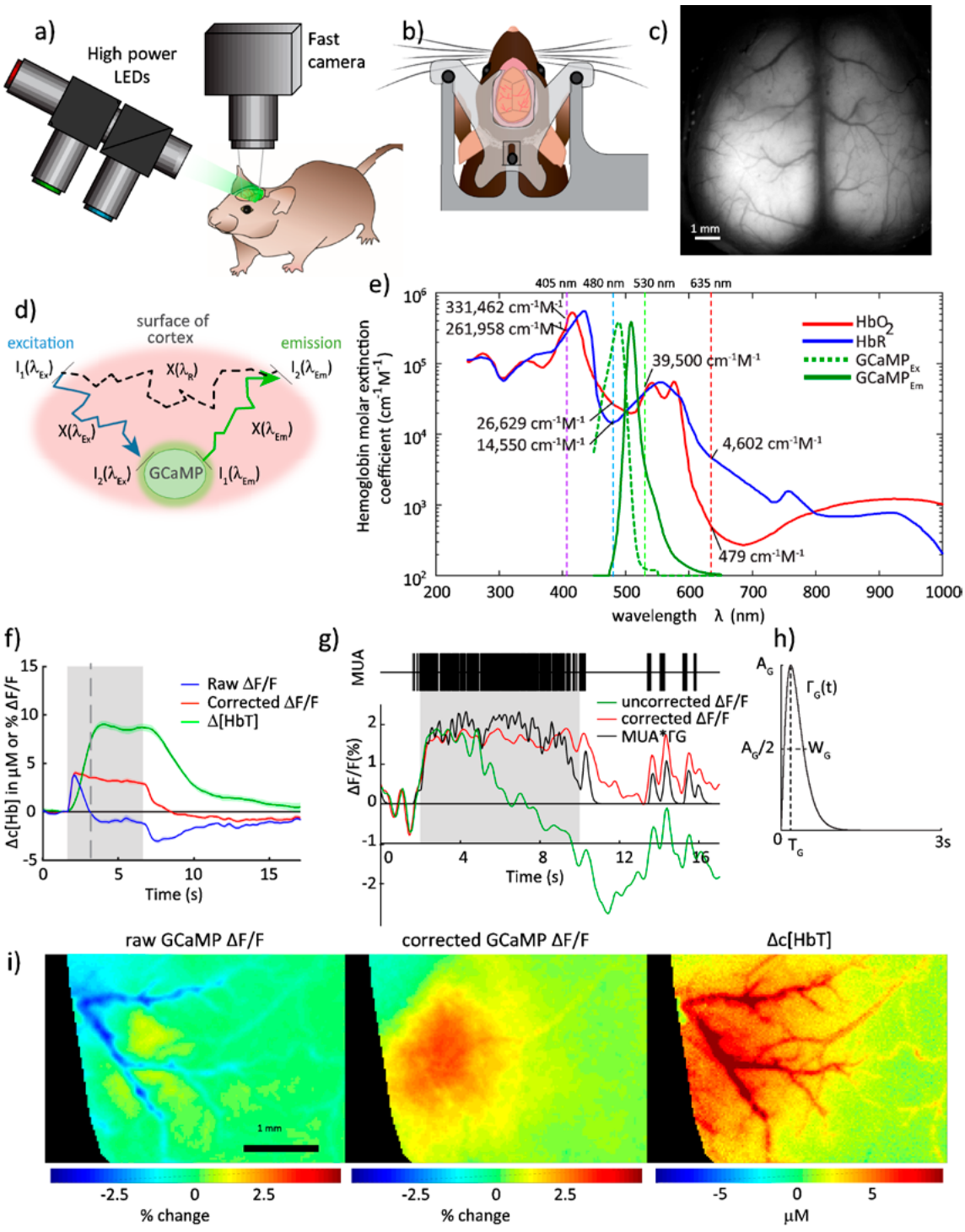


**Figure 3**. WFOM of pancortical activity in awake behaving mice. ***a***, Our preferred configuration in which three LEDs are positioned to illuminate the cortex while a fast camera is used to image it. The LEDs are strobed in synchrony with sequential camera frames to provide three interleaved images of fluorescence and diffuse reflectance. ***b***, The WFOM head plate and thinned-skull preparation provide optical access to almost the entire dorsal surface of the cortex (***c***) while allowing quick head fixation and release. Scale bar, 1 mm. ***d***, Paths taken by light in a wide-field geometry to and from a fluorophore. ***e***, Wavelength-dependent absorption spectra of HbO and HbR (log-scale) and the excitation and emission spectra of GCaMP (linear scale). ***f***, Detected GCaMP fluorescence signal before and after hemodynamic correction along with total hemoglobin (HbT) from reflectance measurements, all taken from the whisker barrel (***i***) of an awake mouse during a 5 s tactile whisker stimulus. Before correction, the increasing absorption of HbT during functional hyperemia causes a marked decrease in detected fluorescence. ***g***, A control measurement in which multiunit electrophysiology was acquired in the same location as GCaMP3 fluorescence. Convolving spikes with a putative calcium indicator gamma-function response (***h***) yields a signal that more closely matches measured fluorescence after hemodynamic correction. ***i***, Proper hemodynamic correction further removes vascular patterns from measured fluorescence.

NOTES

Substituting into Equation 3, we get the following:

$$I_2(t,\lambda_{em}) = F(t) I_1(t,\lambda_{ex}) e^{-(\mu_a(t,\lambda_{ex})\chi(\lambda_{ex})+\mu_a(t,\lambda_{em})\chi(\lambda_{em}))} \quad (6)$$

$$F(t) = \frac{I_2(t,\lambda_{em})}{I_1(t,\lambda_{ex})} e^{(\mu_a(t,\lambda_{ex})\chi(\lambda_{ex})+\mu_a(t,\lambda_{em})\chi(\lambda_{em}))} \quad (7)$$

Importantly, this physical explanation of the origins of fluorescence contamination indicates that signal correction should be multiplicative rather than additive, and thus will not diminish for fluorophores or light sources with higher brightness. It is also important to note that hemodynamic changes will likely be casually coupled to neural dynamics and will thus not be separable via averaging multiple trials.

In WFOM, our approach to hemodynamic correction is to make additional reflectance measurements that estimate the spatiotemporally varying absorption contaminating fluorescence images. Measuring hemoglobin dynamics via diffuse reflectance is a well-established technique (Dunn et al., 2003; Martin et al., 2006; Bouchard et al., 2009). In WFOM, in addition, interlaced images are acquired with the same camera (at ~75 Hz) while the cortex is illuminated by two additional wavelengths of light. For GCaMP, reflectance at green (~530 nm) and red (~630 nm) wavelengths are taken, enabling all light to pass through a fluorescence 500 nm emission filter to the camera without moving parts (Fig. 3*e*). For correction, these measurements can be used to estimate the time-varying concentrations of HbO and HbR derived from the red and green reflectance measurements (derived using Eq. 2), which can then be used to predict the spatiotemporal attenuation of blue light that would correspond to these absorption changes. Similarly, calculating the attenuation of green emission light can be done using the relevant emission spectrum of the fluorophore rather than the same wavelength band of green light used for the diffuse reflectance measurement. By combining these measurements with estimates of path lengths $X_{ex}$, $X_{em}$, $X_{Rgreen}$, and $X_{Rred}$, an estimate of $e^{(\mu_a(t,\lambda_{ex})\chi_{ex}(\lambda)+\mu_a(t,\lambda_{em})\chi(\lambda_{em}))}$ can be derived and simply divided from measured fluorescence at each pixel to yield corrected data (Ma et al., 2016c).

Although no WFOM correction can be 100% exact, this approach follows the expected physical properties of attenuation of excitation and emission light and does not use subtraction or rely on regression to remove contamination. This approach also provides insights into the relationship between neural activity and blood flow (neurovascular coupling), which is relevant to understanding fMRI data which records signals corresponding to changes in the concentrations of HbR as a surrogate for neural activity (Ma et al., 2016a).

### Applications of WFOM

Despite the need for careful hemodynamic correction, the simplicity of collecting high-speed, wide-field data on awake behaving mice enables researchers to perform a wide range of complex experiments that would otherwise be beyond the reach of even fMRI experiments. For example, WFOM enables high-speed, simultaneous imaging of both neural activity and brain hemodynamics over the entire dorsal cortical surface of the mouse cortex. During imaging, the mouse's behavior can be observed and tasks can be performed, stimuli presented, or perturbations such as optogenetics and drugs administered. The technique is also well suited to the longitudinal characterization of disease progression, treatment response, and recovery (e.g., in Alzheimer's disease, brain cancer, and stroke). Here, WFOM provides simultaneous assessment of effects on behavior, bilateral neural representations of behavior, and associated alterations in hemodynamic representations of neural activity.

## Summary

In summary, a range of new methodologies for optical imaging are leveraging the power of new optical indicators of cellular function to capture real-time multimodal activity across more and more brain regions in parallel. These techniques are providing new views of the awake behaving brain—from flies to mice—and promise important new insights into how whole-brain, real-time activity drives, shapes, and represents behavior.

NOTES

## References


Ahrens MB, Orger MB, Robson DN, Li JM, Keller PJ (2013) Whole-brain functional imaging at cellular resolution using light-sheet microscopy. Nat Methods 10:413–420.

Akerboom J, Chen TW, Wardill TJ, Tian L, Marvin JS, Mutlu S, Calderón NC, Esposti F, Borghuis BG, Sun XR, Gordus A, Orger MB, Portugues R, Engert F, Macklin JJ, Filosa A, Aggarwal A, Kerr RA, Takagi R, Kracun S, et al. (2012) Optimization of a GCaMP calcium indicator for neural activity imaging. J Neurosci 32:13819–13840.

Allen WE, Kauvar IV, Chen MZ, Richman EB, Yang SJ, Chan K, Gradinaru V, Deverman BE, Luo L, Deisseroth K (2017) Global representations of goal-directed behavior in distinct cell types of mouse neocortex. Neuron 94:891–907.e6.

Bouchard MB, Chen BR, Burgess SA, Hillman EM (2009) Ultra-fast multispectral optical imaging of cortical oxygenation, blood flow, and intracellular calcium dynamics. Opt Express 17:15670–15678.

Bouchard MB, Voleti V, Mendes CS, Lacefield C, Grueber WB, Mann RS, Bruno RM, Hillman EM (2015) Swept confocally-aligned planar excitation (SCAPE) microscopy for high speed volumetric imaging of behaving organisms. Nat Photonics 9:113–119.

Boyden ES, Zhang F, Bamberg E, Nagel G, Deisseroth K (2005) Millisecond-timescale, genetically targeted optical control of neural activity. Nat Neurosci 8:1263–1268.

Chen F, Tillberg PW, Boyden ES (2015) Optical imaging. Expansion microscopy. Science 347:543–548.

Chen TW, Wardill TJ, Sun Y, Pulver SR, Renninger SL, Baohan A, Schreiter ER, Kerr RA, Orger MB, Jayaraman V, Looger LL, Svoboda K, Kim DS (2013) Ultrasensitive fluorescent proteins for imaging neuronal activity. Nature 499:295–300.

Chung K, Deisseroth K (2013) CLARITY for mapping the nervous system. Nat Methods 10:508–513.

Dana H, Mohar B, Sun Y, Narayan S, Gordus A, Hasseman JP, Tsegaye G, Holt GT, Hu A, Walpita D, Patel R, Macklin JJ, Bargmann CI, Ahrens MB, Schreiter ER, Jayaraman V, Looger LL, Svoboda K, Kim DS (2016) Sensitive red protein calcium indicators for imaging neural activity. eLife 5:e12727.

Dunn AK, Devor A, Bolay H, Andermann ML, Moskowitz MA, Dale AM, Boas DA (2003) Simultaneous imaging of total cerebral hemoglobin concentration, oxygenation, and blood flow during functional activation. Opt Lett 28:28–30.

Dunsby C (2008) Optically sectioned imaging by oblique plane microscopy. Opt Express 16:20306–20316.

Gong Y, Wagner MJ, Zhong Li J, Schnitzer MJ (2014) Imaging neural spiking in brain tissue using FRET-opsin protein voltage sensors. Nat Commun 5:3674.

Gong Y, Huang C, Li JZ, Grewe BF, Zhang Y, Eismann S, Schnitzer MJ (2015) High-speed recording of neural spikes in awake mice and flies with a fluorescent voltage sensor. Science 350:1361–1366.

Hillman EM (2014) Coupling mechanism and significance of the BOLD signal: a status report. Annu Rev Neurosci 37:161–181.

Hillman EMC, Voleti V, Patel K, Li W, Yu H, Perez-Campos C, Benezra SE, Bruno RM, Galwaduge PT (2018) High-speed 3D imaging of cellular activity in the brain using axially-extended beams and light sheets. Curr Opin Neurobiol 50:190–200.

Huisken J, Swoger J, Del Bene F, Wittbrodt J, Stelzer EH (2004) Optical sectioning deep inside live embryos by selective plane illumination microscopy. Science 305:1007–1009.

Kozberg MG, Ma Y, Shaik MA, Kim SH, Hillman EM (2016) Rapid postnatal expansion of neural networks occurs in an environment of altered neurovascular and neurometabolic coupling. J Neurosci 36:6704–6717.

Ma Y, Shaik MA, Kozberg MG, Kim SH, Portes JP, Timerman D, Hillman EM (2016a) Resting-state hemodynamics are spatiotemporally coupled to synchronized and symmetric neural activity in excitatory neurons. Proc Natl Acad Sci USA 113:E8463–E8471.

Ma Y, Shaik MA, Kim SH, Kozberg MG, Thibodeaux DN, Zhao HT, Yu H, Hillman EM (2016b) Wide-field optical mapping of neural activity and brain haemodynamics: considerations and novel approaches. Philos Trans R Soc Lond B Biol Sci 371:20150360.

Ma Y, Kim S, Shaik M, Zhao T, Hillman E (2016c) Widefield optical mapping of neural activity and cortical hemodynamics imaging during locomotion. Soc Neurosci Abstr 63.14.

NOTES

Machler P, Wyss MT, Elsayed M, Stobart J, Gutierrez R, von Faber-Castell A, Kaelin V, Zuend M, San Martin A, Romero-Gomez I, Baeza-Lehnert F, Lengacher S, Schneider BL, Aebischer P, Magistretti PJ, Barros LF, Weber B (2016) *In vivo* evidence for a lactate gradient from astrocytes to neurons. Cell Metab 23:94–102.

Martin C, Martindale J, Berwick J, Mayhew J (2006) Investigating neural-hemodynamic coupling and the hemodynamic response function in the awake rat. Neuroimage 32:33–48.

Murphy TH, Boyd JD, Bolaños F, Vanni MP, Silasi G, Haupt D, LeDue JM (2016) High-throughput automated home-cage mesoscopic functional imaging of mouse cortex. Nat Commun 7:11611.

Patriarchi T, Cho JR, Merten K, Howe MW, Marley A, Xiong WH, Folk RW, Broussard GJ, Liang R, Jang MJ, Zhong H, Dombeck D, von Zastrow M, Nimmerjahn A, Gradinaru V, Williams JT, Tian L (2018) Ultrafast neuronal imaging of dopamine dynamics with designed genetically encoded sensors. Science 360:eaat4422.

Pepperkok R, Squire A, Geley S, Bastiaens PI (1999) Simultaneous detection of multiple green fluorescent proteins in live cells by fluorescence lifetime imaging microscopy. Curr Biol 9:269–274.

Rossi LF, Wykes RC, Kullmann DM, Carandini M (2017) Focal cortical seizures start as standing waves and propagate respecting homotopic connectivity. Nat Commun 8:217.

Shibuki K, Hishida R, Murakami H, Kudoh M, Kawaguchi T, Watanabe M, Watanabe S, Kouuchi T, Tanaka R (2003) Dynamic imaging of somatosensory cortical activity in the rat visualized by flavoprotein autofluorescence. J Physiol 549:919–927.

St-Pierre F, Marshall JD, Yang Y, Gong Y, Schnitzer MJ, Lin MZ (2014) High-fidelity optical reporting of neuronal electrical activity with an ultrafast fluorescent voltage sensor. Nat Neurosci 17:884–889.

Tomer R, Khairy K, Amat F, Keller PJ (2012) Quantitative high-speed imaging of entire developing embryos with simultaneous multiview light-sheet microscopy. Nat Methods 9:755–763.

Vanni MP, Murphy TH (2014) Mesoscale transcranial spontaneous activity mapping in GCaMP3 transgenic mice reveals extensive reciprocal connections between areas of somatomotor cortex. J Neurosci 34:15931–15946.

Xu HP, Burbridge TJ, Chen MG, Ge X, Zhang Y, Zhou ZJ, Crair MC (2015) Spatial pattern of spontaneous retinal waves instructs retinotopic map refinement more than activity frequency. Dev Neurobiol 75:621–640.